# The use of green $H_2$ and sustainable carburization to $Fe_3C$ for the direct reduction of iron ore pellets

MSc. Thesis - Sustainable Energy Technology

Hugo van Leeuwen

Delft University of Technology

TU Delft

# The use of green $H_2$ and sustainable carburization to $Fe_3C$ for the direct reduction of iron ore pellets

by

Hugo van Leeuwen

to obtain the degree of Master of Science
at Delft University of Technology,
to be defended publicly on Friday April 12, 2024 at 12:00 PM.

| | | |
|---|---|---|
| Student number: | 4534662 | |
| Department: | Process & Energy | |
| Project duration: | August 1, 2023 – April 12, 2024 | |
| Thesis committee: | Dr. O. Moultos, | TU Delft, supervisor |
| | Dr. P. Dey, | TU Delft |
| | Dr. L. J. P. Van den Broeke, | TATA Steel, supervisor |
| | Prof. dr. ir. T. J. H. Vlugt, | TU Delft |

Cover: Article: *'Verduurzaming industrie wordt maatwerk'*, Agro&Chemie, 05/05/2022.

TU Delft TATA STEEL

" ’t Het nog nooit,
nog nooit zo donker west,
Of ’t wer altied
wel weer licht "

**Ede Staal** *(1984)*

" ’t Has never,
never been so dark,
Or it has always
gotten light again "

**Ede Staal** *(1984)*

# Acknowledgements

I extend my sincere gratitude to all those who have contributed to the completion of this thesis. First, I would like to express my deepest appreciation to my daily supervisor and the chair of my thesis committee, dr. O. Moultos, whose support, patience, and encouragement have been invaluable. I am grateful that I could always reach out to him and that he always had the time and space to discuss the new developments of my thesis, no matter how minor or major the issue. His guidance and dedication have been crucial in navigating the challenges encountered during this research.

I am also indebted to dr. L.J.P. Van den Broeke for providing me with the opportunity to conduct my thesis in collaboration with TATA Steel IJmuiden. It has been an incredible experience to finish my years at university at a company of such stature and on such an interesting and valuable topic. Furthermore, I am grateful for his guidance and insightful feedback during the past nine months.

Special gratitude is reserved for prof. dr. ir. T.J.H. Vlugt of the department of Process & Energy at Delft University of Technology. I would like to thank him for his academic support and expertise throughout my thesis. I always found our meetings to be constructive and I greatly appreciated his approachability.

I would like to extend my heartfelt thanks to dr. P. Dey for her assistance, encouragement, and valuable suggestions during the course of this research. Her valuable feedback during our meetings encouraged me to keep me on my toes and onto the right track.

Furthermore, I would like to extend my appreciation to dr. ir. M. Ramdin of the Engineering Thermodynamics research group at Delft University of Technology. He provided me with valuable support on the economics part of this thesis. From the same research group, I would also like to thank PhD candidate M. Polat, who assisted me on the thermodynamic sections.

Of the people at the Research & Development department of TATA Steel IJmuiden, my special thanks go out to Maria Naharro Vilas for advising me on the carburization process and on the gas phase reactions and to Johannes Hage, who provided me with the operational data used throughout this thesis.

Lastly, I am deeply grateful to my family, friends, fellow thesis students and old roommates in Delft for their support, understanding, and encouragement throughout this academic endeavor.

# Summary

Steel manufacturing is a carbon intensive process, that is responsible for approximately 7% of the total global $CO_2$ emissions. Therefore, TATA Steel IJmuiden aims to lower its carbon emissions. One way to bring down emissions, is to replace the existing blast furnace (BF) CO reduction process with the $H_2$-based direct reduction of iron ore (DRI). The challenge for TATA Steel IJmuiden lies in maintaining a carbon weight percentage of 2 wt.% to 4 wt.% in their high grade steel product, when no carbon source is present in the reducing or cooling gas stream.

Many research has already been conducted on $H_2$ iron ore reduction and it is known that reduction with $H_2$ has a two to three times higher reaction rate than reduction with CO. Furthermore, reduction of iron ore with $H_2$ has an optimal temperature at T = 1173 K, while higher metallization degrees are attained for $H_2$ reduction compared to reduction with CO. The two most widely applied $H_2$-DRI processes around the world are the low pressure MIDREX, abbreviated as MLP, and medium pressure HYL-Energiron, abbreviated as EMP. Since TATA Steel IJmuiden wants to study the switch from BF to $H_2$-DRI steelmaking, it is relevant to gain insight into which gas phase reactions are dominant for both processes, into the direct reduction process itself and into the behaviour of the carburization reactions. Although research has already been conducted on the modelling of the MLP and EMP processes, there is a lack in reaction rate comparison studies and on studies of the dominant carburization mechanisms. Furthermore, a thorough techno-economic feasibility study on green $H_2$-based steel production scenarios in the Netherlands may prove to be a valuable addition to existing work on $H_2$-DRI processes in Scandinavia.

To model the gas phase reactions, iron ore reduction and carburization reactions, Gibbs minimization and kinetic reaction models were applied on obtained MLP and EMP stream data. In the gas phase reactions, it was seen that for the MLP process *in situ* reforming of natural gas can be a viable option before switching to a 100% $H_2$ process. This may prove to be worthwhile in the early stages of $H_2$-DRI steel production, when green $H_2$ is still scarce and expensive. For EMP, internal reforming seems less of a possibility due to the high reaction rate for the reverse water gas-shift. So for EMP, external reforming of natural gas is required for a DRI process on syngas. When comparing both MLP and EMP, reaction rates are generally higher for EMP than for MLP and hence smaller reactor volumes are required for the EMP process to acquire the same amount of output. Direct reduction with $H_2$ has a higher reaction rate than reduction with CO, while for the carburization reactions methane cracking was found to be the dominant reaction. Boudouard reaction only plays a minor part in the carburization process and can even be neglected for the EMP process. It is possible to estimate the carbon weight percentage of the DRI end product, although the model of Chipman [28] is only valid up to 850 K. In general, an increase of pressure leads to an increase in the reaction rate of methane cracking and therefore a higher carbon weight percentage in the DRI end product, while an increase in porosity lowers the reaction rate.

Techno-economic scenarios for 100% $H_2$-based DRI in which green $H_2$ is to be imported are only feasible when $H_2$-prices fall below €1.80/kg. This is not a realistic $H_2$-price that will be attained in the next five to ten years. Meanwhile, a scenario with an on-site electrolyzer powered by grey grid electricity only proves to be worthwhile for electricity prices lower than €20/$MWh_e$. Meanwhile, the grid emission factor (GEF) should fall below 0.2 to 0.1 kg $CO_2$/$kWh_e$ to obtain an overall decrease in carbon emissions compared to BF. The Netherlands had an average GEF of 0.421 kg $CO_2$/$kWh_e$ in the year 2023. Belgium seems to be a better location for the implementation of this techno-economic scenario: over 2023 electricity in Belgium had an average GEF of 0.108 kg $CO_2$/$kWh_e$. The most promising techno-economic scenario, which includes an on-site electrolyzer and the construction of a wind farm just off the coast from the TATA Steel IJmuiden site, assumes an electricity price of €40/$MWh_e$. This scenario is optimistic, but looks promising when efficiencies of wind turbines and electrolyzers increase, while the construction costs decrease.

# Contents

# 1 Introduction

Without the iron and steelmaking industry, the world we know today would be a vastly different place. From a bike to a train, or from a soda can to a sky scraper: iron and steel are everywhere. Despite the important role steel plays in society, the production of steel is quite a carbon intensive process. In 2023, 70% of the global steel production was achieved via the coal-based blast furnace process, which approximately emits 1.9 tonnes of $CO_2$ per tonne steel produced [54, 98]. After the blast furnace process, the natural gas-based direct reduction process is most widely applied around the world [98]. Although less carbon intensive than the blast furnace process, natural gas direct reduction still has a carbon intensity of 1.5 tonnes of $CO_2$ per tonne direct reduced iron produced [126]. For both steel manufacturing processes that is indirect and direct emissions combined. Over the year 2023, the total world crude steel production was almost 1900 Mt [125]. Hence it is estimated that the steel manufacturing sector is responsible for nearly 7% of the total global $CO_2$ emissions [42, 55, 57]. In spite of the high carbon intensity of its production, the global demand for steel has grown 1.8% over the year 2023 and is predicted to continue to grow in the years to come [127]. This can be related to a rise in demand in upcoming economies and in the necessity of steel for the energy transition [42, 127]. Steel is required for the construction of wind turbines, electrical vehicles and battery casings, among others. It is evident though that the carbon intensity of the steel and iron manufacturing industry must decrease, otherwise climate goals and agreements can not be upheld.

When looking closer to home, this also applies to the iron and steelmaking industry in the Netherlands. The steel industry is located in IJmuiden in the province of Noord-Holland and is owned by TATA Steel. In 2022, steel production at the TATA Steel site in IJmuiden had a carbon intensity of 19% under the global average [36, 115]. Therefore, TATA Steel IJmuiden was acknowledged as the third cleanest steel manufacturer in the world [36, 115]. Despite these promising statistics, TATA Steel IJmuiden still emitted 9.7 Mt of $CO_2$ over the year 2022 [77]. Hence a reduction in $CO_2$ emissions at the site of TATA Steel in IJmuiden can have a positive impact on the carbon footprint of the Netherlands nonetheless. To put in an effort to decrease their carbon pollution, TATA Steel already presented a comprehensive plan of action: the so-called *Roadmap Plus* [115]. Launched in 2020, the *Roadmap Plus* program brings forth multiple objectives and measures to prepare TATA Steel IJmuiden for the future. According to the program, the ambitious goal is to achieve a $CO_2$ reduction of up to 40% by 2030. To realize the demanding targets, research is being conducted on the direct reduction of iron ore (DRI) with green hydrogen [17, 37]. It is reported that a substitution of natural gas with $H_2$ can reduce the direct $CO_2$ emissions from 0.45 to 0.04 tonnes of $CO_2$ per tonne DRI produced [98]. That is a decrease of direct $CO_2$ emissions of 91%.

The direct reduction of iron ore by natural gas or hydrogen is not a completely new concept and in light of this topic a lot of research has already been conducted [13, 32, 56, 98]. In the USA and Germany for example, DRI plants on natural gas have already been in use for several decades [50]. As of yet however, none of these sites is operating on 100% $H_2$ [50, 126]. Therefore, more research on the topic of $H_2$-based DRI production is necessary. For the production of one tonne liquid steel it is estimated that 60 kg of $H_2$ is required for the direct reduction alone [98]. In 2023, TATA Steel IJmuiden had a crude steel output of 4.7 Mt [59]. Assuming a constant steel production over the year, this indicates that TATA Steel

IJmuiden requires over 770.000 kg of green $H_2$ per day. In the current economy it is not yet possible to acquire such amounts, let-alone to be able to produce a cost-competitive commodity with present $H_2$ market prices of over €8/kg [85]. Another problem that arises when reducing iron ore with $H_2$, is that of the quality of the steel end product. Due to a weight percentage of 2 wt.% to 4 wt.% of cementite or $Fe_3C$ in the high quality steel of TATA Steel IJmuiden, it can be used in the automotive industry, for the production of batteries or for the production of robust appliances [75, 81]. When using 100% hydrogen for iron ore reduction however, no carbon source is present to form the $Fe_3C$-bonds and to give the steel its high grade quality. Achieving carbon neutrality in the iron and steelmaking industry is therefore a major challenge for the years to come. This thesis aims to contribute to the topic of $H_2$-based DRI production and intends to address both the direct and indirect $CO_2$ emissions of the process.

With all the aforementioned challenges and obstacles in mind, the following research question is proposed for this thesis study:

How does the direct reduction of iron ore with hydrogen compare to existing direct reduction processes under different operating conditions, while including the carburization process and producing a cost-competitive end-product?

Subsequently, this research question leads to the following set of sub-questions:

1. What are the main differences between existing direct reduction processes and direct reduction based solely on hydrogen?
2. What are the effects of pressure, temperature, $H_2$ concentration in the reducing gas and pellet porosity on the reaction rates and equilibria of the chemical reactions for the direct reduction process?
3. Which carburization mechanism is dominant and what is the effect of temperature, pressure and pellet porosity on the carburization reactions?
4. Under which conditions does iron and steel manufacturing with hydrogen become economically feasible?

To address the research question and sub-questions at hand, this thesis research will focus on the following goals in chronological order:

1. Research of the chemical processes and thermodynamic equilibrium compositions for the gas phase in a shaft furnace for the direct reduction of iron ore
2. Investigation of the reaction kinetics of the direct reduction of iron ore
3. A look into the reaction kinetics of the carburization process
4. Techno-economic assessment of $H_2$ requirements, production, import and storage options by proposing different techno-economic scenarios

For the purpose of this study, the main insights of earlier work will be presented and discussed in Chapter 2. In Chapter 3, the methodology of the thesis is further explicated. Then in Chapter 4, both the results and the discussion for the thermodynamic equilibrium modelling, the kinetic reaction modelling and techno-economic scenario modelling are presented. Thereafter, in Chapter 5 the conclusions of this thesis research are formulated. Finally, Chapter 6 will propose the recommendations on the direct reduction process, sustainable carburization and on further research into the topic of $H_2$-based DRI production.

# 2

# Steel Manufacturing

Before the thermodynamic equilibrium modelling and kinetic reaction modelling can be performed, at first a study is conducted on existing iron and steel manufacturing processes. This concerns both the blast furnace (BF) process and the direct reduction of iron ore (DRI) process. The concepts of DRI and BF steelmaking will be discussed in Section 2.1, while Section 2.2 will touch upon the chemical reactions for the DRI process. Subsequently, in Section 2.3 the state-of-the-art DRI processes will be discussed. Section 2.4 will compare $H_2$ with CO as reducing agent for the DRI process, while in Section 2.5 the concept of the carburization process is explained. At last, in Section 2.6 the basis for this thesis is briefly discussed.

## 2.1. Direct Reduction of Iron Ore

The main concept of the reduction of iron ore is the same for both BF and DRI processes. The former makes use of a blast furnace (BF) in its process, while the latter operates with a shaft furnace (SF). Both furnaces are schematically shown in Figure 2.1. For both steel manufacturing routes, raw iron ore burden is reduced to metallic iron via a reducing agent. For this thesis research it is considered that iron ore burden consists of 100% $Fe_2O_3$, which is also known as hematite [72]. To get from the raw iron ore to the steel end product, all the oxygen inside of the hematite has to be removed to get to metallic iron [50]. During the reduction of $Fe_2O_3$, it is recognized that multiple iron ore intermediates are formed before the metallic end product is obtained [13, 50]. In Table 2.1, hematite and its intermediates are presented. During hematite reduction, the first intermediate state the iron ore reaches is that of magnetite, or $Fe_3O_4$. Subsequently, magnetite reduces to wustite or $Fe_xO$, that can have varying values for the $x$ depending on the reaction conditions and process parameters. For this research and according to Béchara et al. [13] and Hamadeh, Mirgaux, and Patisson [50], $x$ can be assumed to be 0.95. Finally, wustite reduces to metallic iron that leaves the reactor. An important sequential reaction to this last stage of reduction is the formation of cementite, or $Fe_3C$. Usually, the metallic iron product that that is needed in this stage of the process at TATA Steel IJmuiden contains 2 wt.% to 4 wt.% of carbon before it leaves the reactor [115]. This specific carbon content has two purposes. At first, it leads to a lower usage of energy in the

**Table 2.1:** The names of the different iron oxides and the chemical compositions [12, 13, 32, 45]. In accordance with previous studies, the value for $x$ is assumed to be 0.95 [12, 50, 63, 64].

| Chemical species | Chemical composition |
|---|---|
| *Hematite* | $Fe_2O_3$ |
| *Magnetite* | $Fe_3O_4$ |
| *Wustite* | $Fe_xO$ |
| *Iron* | Fe |
| *Cementite* | $Fe_3C$ |

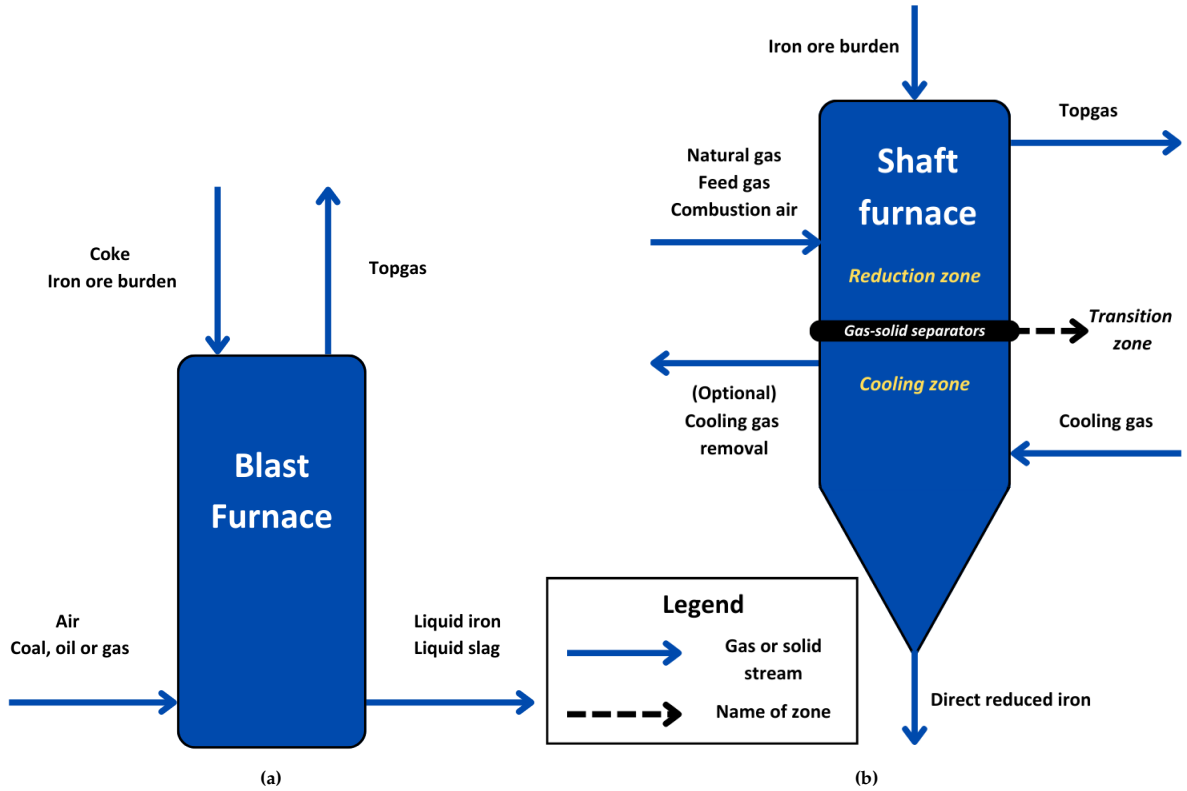


**Figure 2.1: a)** Schematic overview of a blast furnace. Iron ore burden and coke are fed-in at the top, reducing agents at the bottom. After the iron ore reduction, the hot liquid iron product leaves the furnace at the bottom. **b)** Schematic overview of a shaft furnace. Iron ore is fed-in from the top, where it is reduced by a reducing gas in the *reduction zone*. Reduced Fe then flows through the *transition zone* into the *cooling zone*, where the solid is cooled down and carburized through a cooling gas [45, 91, 130].

**Table 2.2:** Operating temperatures and pressures of a blast furnace and a shaft furnace for the direct reduction of iron ore [34, 45, 67, 91, 130].

| | **Blast Furnace** | **Shaft Furnace** |
|---|---|---|
| Possible reducing agents | Coal, coke, CO | $H_2$, CO, $CH_4$ |
| $P$ / [atm] | 2.5 | 1 - 8 |
| $T_{\text{furnace}}$ / [K] | 2250 | 1150 |
| $T_{\text{reducing gas}}$ / [K] | 1250 - 1550 | 1000 - 1300 |
| $T_{\text{top gas}}$ / [K] | 350 - 450 | 550 - 850 |
| $T_{\text{cooling gas in}}$ / [K] | - | 300 - 325 |
| $T_{\text{cooling gas out}}$ / [K] | - | 750 - 775 |
| $T_{\text{iron ore in}}$ / [K] | 298 | 298 |
| $T_{\text{iron product out}}$ / [K] | 1750 | 325 - 875 |

electric arc furnace (EAF) further down in the process [63, 64, 98]. After the metallic iron leaves the SF, it is subsequently melted and processed to steel in an EAF. Secondly, the carbon content gives the steel its high grade quality, a unique selling point of the TATA Steel site in IJmuiden [2, 75, 115].

While the reduction of $Fe_2O_3$ to metallic Fe occurs both in BF and SF steel manufacturing, the two production routes differ in main concepts and operating conditions. By far the most commonly used form of steel production is that of the BF, which currently represents approximately 70% of the world total [45, 55, 89, 109]. At the moment, only 7% of global steel production is obtained via DRI [55, 40, 89]. The other 23% is produced via the recycling of scrap metal in an EAF [89]. In Figure 2.1, a schematic overview of the BF and the SF is given. As can be seen in Figure 2.1a, a BF can be interpreted

as a chemical reactor that has two inflows (one solid, one gas) and two outflows (one solid, one gas). Although the BF route of steel manufacturing is the most widely used steel production process around the world, it is also the most polluting form. When incorporating the complete process from cradle to cradle, it is estimated that the total $CO_2$ emissions for a BF amount to 1.9 tonnes of $CO_2$ per tonne steel produced [32, 53, 67, 128]. Meanwhile, for the natural gas-based DRI process the total $CO_2$ emissions are estimated at 1.5 tonnes of $CO_2$ per tonne direct reduced iron produced [98, 126]. Therefore, even when operating on natural gas, the DRI steel production route is less carbon intensive than the BF-route. Whereas the BF steel manufacturing route focuses on the melting of the iron ore burden and produces a molten iron end product, the SF DRI process aims to directly reduce the iron ore burden in the solid phase, without melting it [47]. Hence its name, the direct reduction of iron ore. Therefore operating temperatures inside an SF can be 1100 K lower than temperatures in a BF as is shown in Table 2.2.

Just like the BF, the SF can be seen as a counter-current flow reactor, with solids moving from the top to the bottom and gases flowing from the bottom to the top. Roughly halfway through the SF the reducing gas is introduced, usually consisting of a mixture of $H_2$, CO and $CH_4$ and a low volume of their reaction products, $H_2O$ and $CO_2$ [19, 50]. After the reduction of the iron ore has taken place in the top part of the reactor, all gases leave the SF via the topgas stream. This part of the reactor is known as the *reduction zone* [12, 32, 50, 103, 105]. When examining Figure 2.1b, it can be seen that an SF usually has an extra inflow and an extra outflow in its process scheme compared to the BF shown in Figure 2.1a. These are intended for a cooling gas, that is introduced to the reactor after the hematite is reduced to metallic Fe [12, 50, 56, 66]. This part of the reactor is known as the *cooling zone* [50, 48, 105]. The main constituent of this cooling gas generally is $CH_4$, or natural gas, which functions as a carburizing agent as well as a coolant [105]. This ensures the production of cold DRI, that leaves the reactor usually at 325 K [34]. That is 1500 K lower than the molten iron product that is produced in a BF and therefore the DRI end product is significantly more facile to process further. More temperatures for the inlet and outlet streams of the BF and SF are given in Table 2.2. From Table 2.2 it is evident that pressures inside a BF are moderate, while pressures in an SF can be increased as high as 8 atm. The outlet stream of the cooling gas for SF is optional, as in some cases this stream is included and in some excluded [91, 130]. If not included in the SF process, the cooling gas leaves the reactor together with the other gases via the topgas outlet stream. When the exit stream of the cooling gas is included, there are usually valves installed in the SF to separate the *cooling zone* gases from the *reduction zone* gases [12]. This is illustrated in Figure 2.1b by the black bar in the middle of the furnace. This area is known in literature as the *transition zone* [12, 48, 50, 105].

## 2.2. Chemical Reactions for the Direct Reduction of Iron Ore

The chemical reactions for DRI are presented in Table 2.3, in combination with their reaction enthalpies under standard conditions. In a BF, the main iron ore reduction processes are those concerning CO or *R2* and *R4*. In an SF supplied with syngas, both $H_2$ and CO reduction take place and *R1* up to and including *R4* need to be taken into account. In Table 2.3, the reduction of magnetite ($Fe_3O_4$) into wustite ($Fe_{0.95}O$) is not considered. According to previous studies, this reaction occurs almost instantaneously on account of its quick reduction kinetics and has a conversion of close to 100% [23, 50, 62, 109]. For sake of simplicity, this reaction is therefore omitted and for the remainder of this research it is assumed that hematite reduces directly into wustite in the stoichiometric ratio that is observed in Table 2.3. During the reduction reactions, both $H_2O$ and $CO_2$ are formed. These two gases can subsequently react further as is shown in *R6* to *R8* in Table 2.3. From the gas phase reactions, the water-gas shift (WGS) and steam reforming of methane (SRM) are the most important, while dry reforming (DR) only plays a minor role [50]. As can be observed in methane cracking (MC) and the Boudouard reaction (BR), the presence of $CH_4$ and CO in the gas phase can lead to the accumulation of solid carbon or C(s). When not reacting further to form cementite or $Fe_3C$ as shown in *R5*, this solid carbon can block the pores of the iron ore pellets and lower the reactive surface area. This leads to an undesirable decrease in the reduction rate [131]. Furthermore, this solid carbon has the abilility to react with $H_2O$ as is shown for coal gasification (GC) or *R11*, although this reaction requires high operating temperatures.

**Table 2.3:** The chemical processes for the direct reduction of iron ore, considering both the reduction of the iron oxides and the gas phase reactions [13, 23]. Since the reduction of $Fe_3O_4$ happens so rapidly and has such a high conversion rate, for simplicity reasons only the reduction of hematite and wustite are taken into account [23, 62].

| Chemical Reaction | Reac. no. | Formula | | | $\Delta H_R^\circ$ / [kJ/mol] |
|---|---|---|---|---|---|
| $H_2$ Hematite reduction | R1 | $Fe_2O_3 + H_2$ | $\longrightarrow$ | $\frac{40}{19}\,Fe_{0.95}O + H_2O$ | 46.6 |
| CO Hematite reduction | R2 | $Fe_2O_3 + CO$ | $\longrightarrow$ | $\frac{40}{19}\,Fe_{0.95}O + CO_2$ | 5.49 |
| $H_2$ Wustite reduction | R3 | $Fe_{0.95}O + H_2$ | $\longleftrightarrow$ | $0.95\,Fe + H_2O$ | 25.5 |
| CO Wustite reduction | R4 | $Fe_{0.95}O + CO$ | $\longleftrightarrow$ | $0.95\,Fe + CO_2$ | -15.7 |
| Cementite formation | R5 | $3\,Fe + C\,(s)$ | $\longrightarrow$ | $Fe_3C$ | 27.0 |
| Steam Reforming of Methane (*SRM*) | R6 | $CH_4 + H_2O$ | $\longleftrightarrow$ | $CO + 3\,H_2$ | 206.9 |
| Water-Gas Shift (*WGS*) | R7 | $CO + H_2O$ | $\longleftrightarrow$ | $CO_2 + H_2$ | -41.16 |
| Dry Reforming *(DR)* | R8 | $CH_4 + CO_2$ | $\longleftrightarrow$ | $2\,H_2 + 2\,CO$ | 260.5 |
| Methane Cracking *(MC)* | R9 | $CH_4$ | $\longleftrightarrow$ | $C\,(s) + 2\,H_2$ | 75.5 |
| Boudouard Reaction *(BR)* | R10 | $2\,CO$ | $\longleftrightarrow$ | $C\,(s) + CO_2$ | -172.5 |
| Coal Gasification *(CG)* | R11 | $C\,(s) + H_2O$ | $\longrightarrow$ | $CO + H_2$ | 131.4 |

## 2.3. State-of-the-art Direct Reduction of Iron Ore Processes

For the DRI operation, multiple types of processes were developed. Some technologies rely on a rotary kiln, others on a rotary hearth furnace, but none of these concepts could compare with the levels of output and efficiencies of the DRI processes that depend on the SF [47, 56, 67, 102]. From the SF processes that were developed, the Midland-Ross Direct Reduction (MIDREX) process and the HYL-Energiron process are the most promising gas-based technologies. The concept for both of these DRI processes is shown schematically in Figure 2.2 [19]. Since there is no single standard operating condition for both MIDREX and Energiron processes, referring to both concepts can sometimes be confusing. Therefore, throughout the rest of this thesis work MIDREX will be referred to as MIDREX Low Pressure (MLE) and Energiron will be referred to as Energiron Medium Pressure (EMP).

MLP accounts for close to 60% of the total DRI processes across the globe [9, 47]. Since it was the first direct reduction process that could be applied on an industrial scale, it soon gained momentum and therefore now dominates the DRI market [11]. EMP follows as number two, with an approximate market-share of 12% [11, 47]. Despite these numbers, the EMP process shows promising signs for a fully $H_2$-based steel manufacturing route [11]. Of the other DRI processes around the world, the rotary kiln has a market share of 24.4%, while miscellaneous operations account for the last 3.2%. For this thesis, rotary kiln and other DRI production processes are not considered. As is shown in Figure 2.2, both MLP and EMP concepts make use of an SF that consists of a *reduction*, *transition* and *cooling zone*. For both operations the same additions to the overall process can be made. It can be decided to lead the reducing gas through an external reformer before it enters the SF to engage in reduction reactions. Inside this reformer, natural gas and combustion air are brought together to form a syngas mixture with a large share of $H_2$ [105]. Usually, recycled gases from the SF are also led to the reformer, to improve the efficiency of the overall process. It can also be decided to omit this external reformer. In that case it is assumed that the feed-in of natural gas reforms *in situ*, in the SF [88, 130]. For the EMP process this is known as Energiron ZR, in which ZR stands for Zero Reforming [104].

The main difference between the MLP and EMP plant lies in the operating conditions. MLP usually operates at pressures of 1 to 2 bar, close to atmospheric pressure [86, 103, 105]. On the other hand, EMP processes usually operate at higher pressures of 6 to 8 bar [88, 130]. This increase in pressure of EMP compared to the MLP process offers a few advantages. Due to the higher pressure inside of the SF, it is possible to acquire the same amount of output with a lower reducing gas velocity and smaller reactor diameter than compared to the low pressure MLP process. Therefore it is evident that production costs for the EMP process are usually lower than that of the MLP process for the same output. Hence, EMP is more facile to scale-up, while the total power consumption of the process is also lower than for the

MLP process. On the other hand, due to the high pressure operation the EMP process is more costly in operational expenditure [104]. In the end, it is also important to notice that the EMP process can deliver direct reduced iron with a higher $Fe_3C$ content than the MLP process can. EMP can produce metallic iron with an $Fe_3C$ weight percentage up to 4 wt.%, while MLP can produce steel with a weight percentage of only 2 wt.% $Fe_3C$ [34, 104]. It is approximated that in MLP 50 $m^3$ of natural gas is needed per tonne DRI produced for a final $Fe_3C$ content of 1.4% [100].

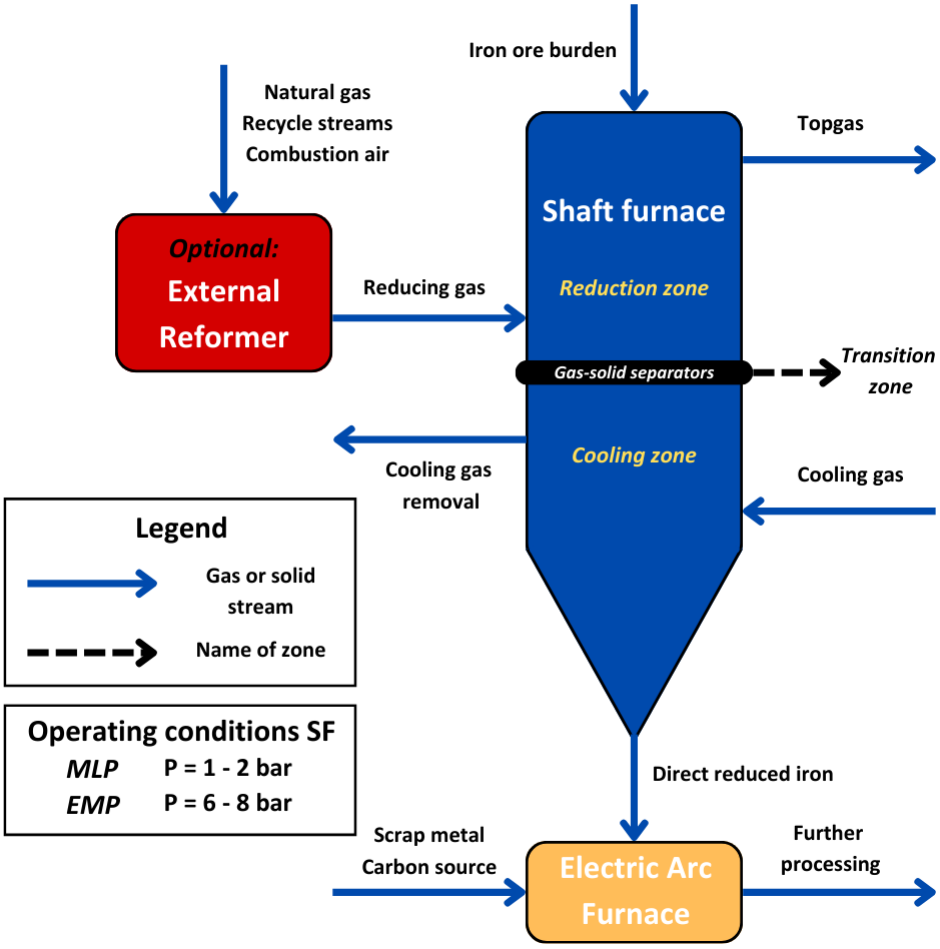


**Figure 2.2:** A schematic overview of a shaft furnace for both MLP and EMP processes. In the shaft furnace, iron ore is fed-in from the top and reduced, cooled and carburized before exiting the furnace as direct reduced iron at the bottom. The reducing gas fed into the furnace can be reformed at first through an optional reformer. The direct reduced iron is processed in an electric arc furnace, where an extra carbon source and scrap metal are added.

For some MLP and EMP plants in operation, stream and furnace data were collected. These are presented in Appendix A. The plants considered here are an MLP plant in Mobile, USA, an MLP plant in Contrecoeur, Canada, an MLP plant near Oregon, USA and an EMP plant mentioned in literature [13, 50, 105, 130]. The MLP process of Appendix A.1 operates with 56% $H_2$ and 36% CO in a $H_2/CO$ ratio of 1.55, while also lower $H_2$ concentrations and $H_2/CO$ ratios have been reported as shown in Appendix A.2 and Appendix A.3 [27, 104]. At the moment, it is already possible to co-feed extra $H_2$ into the MLP process to lower $CO_2$ emissions [6]. However, after a 30% $H_2$ addition changes have to be made to the SF [6]. In Germany and Spain there are ongoing projects that aim to go to a fully $H_2$-based MLP process [104]. Most of the EMP plants currently in operation already use close to 70% of $H_2$ [104], which is confirmed in Table A.8 for the Zugliano EMP plant [130]. It must be noted that in this specific case, the reducing gas that is fed-in into the SF was externally reformed. This explains the relatively high $H_2$ and low $CH_4$ content as seen in Table A.8. For the EMP process, it is already claimed that a sole usage of $H_2$ can be achieved in the existing process without further alteration to the furnace [15].

To attain the necessary levels of carburization of the steel end product, natural gas or pure carbon is injected into the EAF used later on in the process [104].

## 2.4. Iron Ore Reduction with $H_2$ and CO

As mentioned in Section 2.3, as of yet there are no steel manufacturing sites that rely solely on $H_2$ as reducing agent. However, research has been conducted on the topic as well as on iron ore reduction with syngas mixtures. Therefore it is possible to make a comparison between $H_2$-based reduction and CO-based reduction for the direct reduction of iron ore.

For a syngas mixture at temperatures below 850°C, the iron ore reduction reactions with CO have a higher reaction rate than the reduction reactions with $H_2$ [53, 112]. It is acknowledged that this is on account of the stability the CO molecule exhibits under these conditions [73]. All reduction reactions are given in Table 2.3, from *R1* up to and including *R4*. At temperatures above 850°C however, a shift is acknowledged and it is seen that reduction with $H_2$ becomes the dominant reduction mechanism [53, 68, 87, 112]. This shift in reduction rates is likely due to the higher permeability $H_2$ exhibits at these temperatures compared to CO, enabling faster reduction kinetics [15, 25, 53, 73]. The reaction rate for $H_2$ reduction was found to be in the order of two to three times larger than the rate for CO reduction under these operating conditions [18]. Therefore, to acquire the same amount of steel output at these temperatures, a process with $H_2$ requires a smaller reactor volume [15]. For the reduction processes the temperature should not exceed 900°C however, since it has been found that the rates of reaction then decrease considerably due to undesirable pellet sintering [26, 32, 104]. A recent study by Liu et al. [67] has shown that the optimal reduction temperature of a fully $H_2$-based DRI process is 1173 K, or 900°C. Reduction with $H_2$ also has the benefit that it leads to a higher degree of end product metallization than CO reduction does [53, 112, 131]. Another negative effect of reduction with CO is carbon deposition due to BR, shown as *R10* in Table 2.3. This blocks the pores inside of the iron ore pellets and lowers the surface area of the reaction front, which leads to a decrease in the overall reduction rate [131]. It was found that this carbon deposition mainly takes place inside of the SF at temperatures lower than 900°C [18]. Furthermore, full iron ore conversion with CO is almost never achieved [44, 131]. Overall, $H_2$ iron ore reduction is endothermic and CO iron ore reduction exothermic [53, 112, 131]. This means that 100% $H_2$ reduction requires extra energy input in order to get to and maintain the desired reaction temperatures inside the SF. This can be solved by burning $H_2$ gas at the gas heaters in the furnace [98]. It is estimated by Rechberger et al. [98] that approximately 6 kg of $H_2$ per tonne steel is required for sufficient heating of the SF. To maintain a reduction temperature of 1173 K, the use of other renewable energy sources also remains a possibility.

For the whole MLP process to operate on $H_2$ alone, it is estimated that 800 $m^3$ of $H_2$ is required per tonne direct reduced iron produced in standard temperature and pressure [98, 100]. That is 550 $m^3$ for reducing and 250 $m^3$ for heating. Using a general conversion factor of 1/11 to go from kg $H_2$ to $m^3$ $H_2$, under standard temperature and pressure this equals 72.7 kg $H_2$ [117]. Promising reports of experiments by ArcelorMittal in Germany state that for the production of 0.55 Mt of DRI per annum, 635 $m^3$ of $H_2$ per tonne DRI was needed [98]. That is 57.7 kg $H_2$. According to a study by Bhaskar et al. [15], to produce a tonne of direct reduced iron 60 kg of $H_2$ is required. Since the results of Rechberger et al. [98] were obtained experimentally and under optimal conditions and are in line with the findings of [15], for the outset of this thesis a value of 60 kg of $H_2$ per tonne direct reduced steel is applied. When heating with $H_2$ is included, 66 kg per tonne direct reduced steel is assumed.

To summarize, the main advantages of reduction of iron oxides with $H_2$ as compared to CO at the optimum operating condition of 900°C are:

- No $CO_2$ and CO production and/or emissions
- A two to three times higher reduction rate than with CO
- Higher metallization degree of the direct reduced iron end product
- No carbon formation that blocks the pores of the pellets and decreases reduction reaction rates
- A lower reactor volume for the same level of output compared to syngas-based direct reduction

Aside from the benefits of the use of $H_2$ as sole reducing agent, there are also three major drawbacks that need to be considered. These disadvantages are:

- Extra energy is required in the SF due to the highly endothermic nature of $H_2$ iron ore reduction
- Without a carbon source present, no $Fe_3C$ will be formed
- At the moment, green $H_2$ is more expensive than $CH_4$ or syngas

To supply the energy to the DRI process, a surplus of $H_2$ could be added to the gas heaters of the SF or electric heaters powered by a sustainable energy source could be utilized. However, for processes of this scale as of yet there is no precedent. To carburize a certain percentage of the DRI product in a sustainable manner, a sustainable carbon source could be added to the EAF further down in the process. Yet again no current example is available for sustainable carburization at this scale. As current market prices predict, green $H_2$ is more expensive than $CH_4$ or syngas [15, 108]. To eventually produce cost-competitive steel, $H_2$ prices of lower than at least €2 per kg are required [65]. A recently installed 100 MW electrolyzer in Europe now produces its green $H_2$ for more than €8 per kg, which is not even close to the feasible price [65].

## 2.5. Carburization of Iron Ore

The carbon content of the DRI end product has implications for operations further down in the process. As mentioned in Section 2.1, a carbon content of 2 wt.% to 4 wt.% decreases energy consumption for the EAF operation while it also facilitates a high quality steel end product [2, 63, 64, 75, 98, 115]. Hence, *R5* or cementite formation as listed in Table 2.3 is of the utmost importance for steel manufacturing. Therefore, the different parallel reactions that can occur with solid carbon inside the SF should be studied. The reaction mechanism of carburization can be regarded as a two-step process. At first, free carbon atoms are obtained through either MC or BR that diffuse rapidly to the surface of the iron oxide pellets due to a large potential difference between the surface and the atmospheric carbon [2, 124]. This immediately follows from Fick's first law of diffusion. The second step encompasses the diffusion of the adsorbed carbon atoms into the porous iron oxide material, which takes longer and can be determined through Fick's second law of diffusion [2]. It is also given in literature that an increase in temperature and carburizing time leads to a higher penetration depth of the carbon, hence to a stronger DRI end product [1, 110].

Despite the necessity of carbon in the DRI end product, the carbon formed in the SF can also block the pores and decrease the reduction reaction rates. Just as DRI with CO, it is acknowledged that MC (*R9*) and BR (*R10*) only play a role of significance with temperatures up to approximately 850 K [63, 98, 99]. These two reactions are highly exothermic and favoured at lower temperatures than the endothermic CG or *R11*, which usually is the preferred carbon deposition reaction at temperatures higher than 727 K [11]. In the typical DRI process temperatures in the *cooling zone* where the carburization occurs do not reach these heights. *R11* is therefore considered as the main driving force behind the iron ore carburization for the BF process, since the CO-based carburization reactions are not active when T > 860 K [75, 99]. In the MLP and EMP processes given in Appendix A, the cooling gas inflow mainly consists of $CH_4$. It is regarded that for moderate temperatures of 300 K to 700 K, MC or *R9* is the main carburization reaction [50, 99].

## 2.6. Basis of Study

This study will compare the MLP in Appendix A.1 and the EMP plant as mentioned by Zugliano et al. [130] in Appendix A.4. The MLP plant has a $H_2$/CO-ratio of 1.55 while the EMP plant has a $H_2$/CO-ratio of 4.09. For the MLP process, the other data available in Appendix A.2 and Appendix A.3 can be used as extra reference material. Many studies have already looked into the optimization of the reaction parameters for these two processes, while not so many compare 100% $H_2$ use with regular MLP and EMP processes. An extension of earlier research with the option for a fully $H_2$ operating DRI plant can prove to be worthwhile. Generally, economic feasibility studies have been conducted for the use of green $H_2$ in the steel manufacturing world, with some even considering local production

and storage. This has already been done by Bhaskar et al. [15] for a steel plant in Norway, for example. A study into the possible techno-economic scenarios at the TATA Steel site in IJmuiden can prove to be an interesting addition to previous work. Especially when a scenario is researched in which TATA Steel IJmuiden constructs a wind farm in the North Sea for the production of renewable energy to supply an on-site electrolyzer. In the area of carburization, the studies are also thin on the matter of sustainable steelmaking. Adedipe et al. [2] discuss the use of sustainable carbon sources, but only shows small-scale experimental results. Still, a look into the carburization options provided by Adedipe et al. [2] can deliver new insights. A study on the dominant carburization mechanisms in the MLP and EMP processes would be a valuable topic to investigate further on behalf of TATA Steel IJmuiden.

With the plant data available, the thermodynamics, reduction kinetics and carburization processes are studied to formulate an answer to the research questions proposed in Chapter 1. To address the research question and to answer the sub-questions that originate from it, several methods and models were developed throughout the academic world. In Chapter 3, the methods and models that can be applied to study the DRI process are further explicated.

# 3

# Methodology

Each method and each model that was developed to study the DRI process is constrained under its assumptions and limitations. Therefore it is important to identify and compare the different methods that are available to study the different parts of this thesis. A distinction can be made between three fields of interest this thesis lays its focus on: thermodynamic equilibrium modelling, kinetic reaction modelling and techno-economic scenario modelling. For each of these three subjects, different methods and approaches will be discussed in this chapter. At first, the focus of Section 3.1 is to identify the thermodynamic models that exist to study the equilibrium for the bulk gas phase reactions. Then, Section 3.2 will discuss the different approaches for the kinetic reaction modelling for three different aspects of the DRI process: the gas phase, the reduction of the iron ore pellets and the carburization reactions. Finally, in Section 3.3 the different methods for a techno-economic scenario study are explored.

## 3.1. Thermodynamic Equilibrium Modelling

To get a better understanding of the direct reduction of iron oxide pellets, at first it is necessary to gain a better insight into the behaviour of the gases inside of the shaft furnace. Before these gases reach the solid iron oxide pellets and engage in reducing and carburizing reactions, the gases can already undergo homogeneous reactions [3, 50, 56, 105]. This usually leads to a change in the composition of the gas mixture. Subsequently, this can have a direct effect on the reducing or carburizing potential of the system [50, 86, 96]. Therefore it is important to have some understanding of the behaviour of the gas phase reactions, especially under varying operating conditions.

For small gas phase systems in which just one equilibrium reaction is considered, the equilibrium composition of the gas phase can be determined by calculating the equilibrium constant $K_{eq}$ [71, 74]. This is done via the partial pressures of the gases and stoichiometric coefficients of the reaction and the method is known as the Equilibrium Constant Approach. This approach is most practically used in a system with just one equilibrium reaction and calculations for this model become increasingly more complex with an increase of the total reactions in the system. To address homogeneous gas phase systems with multiple reactions, more robust numerical methods have been developed. The method that is most commonly applied for this purpose, is the method of the Gibbs free energy minimization [74, 92, 94, 95].

### 3.1.1. Gibbs Free Energy Minimization

Thermodynamic equilibrium is the state of a system in which no observable changes take place [74]. By definition, this is the point where the Gibbs free energy of the system reaches a minimum value for a certain temperature and pressure [60, 93, 94]. The total Gibbs free energy of a system is calculated via the following relationship [92, 93, 94, 95]:

$$G_{\text{Total}} = \sum_{j=1,2,\dots} [n_j \, \mu_j{}^{\circ}] + RT \sum_{j=1,2,\dots} [n_j \, ln \left( \frac{P^{\circ}}{y_j \, \phi_j \, P_{\text{Total}}} \right)] \tag{3.1}$$

The total Gibbs free energy of a system in [kJ/mol] is a function of the number of moles of component $j$ as $n_j$, the standard chemical potential $\mu_j{}^{\circ}$ in [kJ/mol], the universal gas constant $R$ in [(L·bar)/(K·mol)], temperature $T$ in [K], the dimensionless mole fraction in the gas phase $y_j$, the dimensionless fugacity coefficient $\phi_j$, reference pressure $P^{\circ} = 1$ [bar] and total pressure $P_{\text{Total}}$ in [bar]. When performing a minimization on Equation (3.1) via Matlab, it is possible to attain the equilibrium composition of the system in moles or mole fractions. Equation (3.1) is constrained by the molar balances that can be derived out of the starting compositions of the gases in the system. All further parameters and correlations that are required to minimize Equation (3.1) are given in Appendix B. Here, also the relevant thermodynamic data that is required to solve the equations for the gas phase for the direct reduction of iron ore is listed. Throughout this thesis, the thermodynamic data of the National Institute of Standards and Technology and Joint Army-Navy-Air Force (NIST-JANAF) tables are used. This thermodynamic dataset is freely accessible and is also applied in similar studies [94, 95].

Although the Gibbs minimization method is a robust way to model and simulate equilibrium compositions in the gas phase, the method also has its limitations. The state of chemical equilibrium that is reached via this method is generally only attained after a long period of time. For DRI the gases usually have a mean residence time in the shaft furnace of 12 to 20 seconds [47, 73, 102]. That is not nearly a sufficient amount of time to reach thermodynamic equilibrium. Gibbs minimization also presumes a closed-system in steady-state, whereas the typical DRI process is continuous and transient. It must also be noted that it is difficult to incorporate multi-phase reactions, which poses a problem when trying to incorporate the carburization reactions that contain solid carbon into the model. In spite of these limitations, the method still provides valuable information about the gas phase composition and to which reactions will turn out to be dominant. Another plus side of the Gibbs minimization is that the code it requires is not complex and computational times are small. The Matlab code applied throughout this thesis is given in Appendix E.

In summary the advantages and disadvantages of the Gibbs free energy minimization method are:

- Easily adjustable for different parameters and reaction conditions
- Relatively easy to model, relatively short computational times
- Thermodynamic equilibrium is only reached after a long amount of time and therefore not reached for the direct reduction of iron ore
- Considers a closed system in steady-state, not a continuous and transient process
- Difficult to incorporate non-equilibrium, multi-phase reactions

### 3.1.2. Peng-Robinson Equation of State

The fugacity coefficient ($\phi_j$) of a gas $j$ is a measure of its ideality [70, 74, 94]. When the fugacity is assumed to be unity, the gas behaves perfectly ideal [74]. The more the fugacity coefficient deviates from one, the less ideal the behaviour of its associated gas. To get a better understanding of the behaviour of the gases of the reference cases used for this thesis, it is necessary to calculate their respective fugacities. This can be done via the Peng-Robinson Equation of State [92, 94, 95]. An Equation of State is a mathematical relationship that is used to predict and understand the behaviour of gases [70]. It tries to associate microscopic structure to macroscopic properties and it can be used to calculate densities, enthalpies, entropies, fugacities and more. The Peng-Robinson Equation of State is known through the following relationship.

$$P = \frac{RT}{v_m - b_m} - \frac{a_m}{v_m\,(v_m + b_m) + b_m\,(v_m - b_m)} \tag{3.2}$$

In Equation (3.2), $v_m$ is the molar volume of the gaseous mixture per mole of mixture, while $a_m$ and $b_m$ are specific pure component parameters. The formulas to obtain these specific component parameters and all associated formulas and parameters that are needed to calculate the fugacity coefficient, are given in Appendix B.2. In Appendix B.2, also the fugacity coefficients of the gas streams of Appendix A.1 and Appendix A.4 are tabulated. Although the Peng-Robinson Equation of State is a versatile and generally accurate model for fugacity calculations, the model does get increasingly complex for gaseous mixtures. Additional mixing rules are then required that add more uncertainty to the results obtained from the model [94].

## 3.2. Kinetic Reaction Modelling

To describe DRI, the kinetics of the governing chemical reactions can be expressed mathematically. Many researchers have tried to develop a numerical model that expresses the reduction of hematite pellets as a function of all sorts of parameters [5, 35, 50, 86, 96, 111]. Usually, every study or research considers its own assumptions and limitations in order to investigate different parts and different parameters of the reduction process. The difference that has the most influence on the reaction rates of the DRI process, is the choice of a kinetic reduction model. When considering DRI, two methods are most widely applied in literature: the Unreacted Shrinking Core Model (USCM) and the Grain Model (GM). These two models will be discussed and compared in Section 3.2.1. In Section 3.2.2 the model for gaseous diffusion through a porous solid is discussed, and finally Section 3.2.3 explicates the kinetic reaction rate modelling.

### 3.2.1. Unreacted Shrinking Core Model vs. Grain Model

In USCM it is assumed that the reduction of the iron ore pellets occurs in sequential reaction steps and that there is only one reaction front, that moves inward as the reaction progresses [46, 97, 113, 119]. This model can only be applied accurately when the initial pellet is non-porous and when pore-diffusion is controlled [79, 96, 97]. A schematic overview of the concept of USCM is shown in Figure 3.1. For simplicity it is assumed that an iron oxide pellet consists of 100% hematite or $Fe_2O_3$ before the reduction begins. When the reduction reactions commence, the $Fe_2O_3$ reduces into magnetite or $Fe_3O_4$. In Figure 3.1, $Fe_2O_3$ can be seen as M1 and $Fe_3O_4$ as M2. While reducing, the distance to the centre for M1 called $r_1$ decreases. Since the reaction front is located at the outer layer of the M1 shell, the reaction front moves inward. The $Fe_3O_4$ is formed at the outside of the unreacted $Fe_2O_3$ of the pellet. As the reaction goes on, the reducing gases need to diffuse through an increasing layer of M2 to reach the reaction front. When all of the M1 is reduced, the $Fe_3O_4$ or M2 forms the new reaction front and the subsequent reduction reactions take place to form wustite ($Fe_{0.95}O$). These steps repeat until the metallic Fe end product is formed.

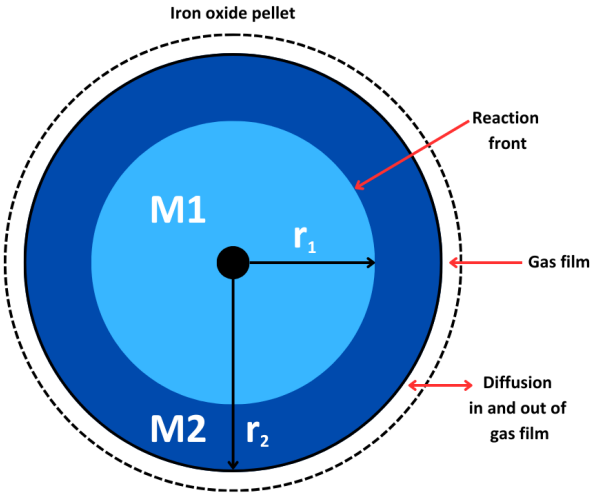


**Figure 3.1:** A schematic overview of USCM [46]. M1 and M2 are the product layers of the reactants and reaction products, respectively. In the same manner, $r_1$ and $r_2$ are the distance of both product layers to the centre of the pellet. The dotted line marks the transport layer between the bulk gas flow and the reducing gas film around the pellet. Before the gases can engage in solid reduction, they first have to diffuse into the gas film and towards the reaction front of M1.

The USCM model is sensitive to mass transfer limitations, since the reducing gases have to diffuse through a product layer before reaching the pellet reaction front [78, 96, 114, 113]. The pellet size also has a major impact on the overall reduction rate of the process, since it affects the mass transfer rate between the bulk gas flow and the gas at the reaction front [96, 97]. General assumptions that are made for USCM throughout literature, are that of plug flow behaviour for gases and solids, a uniform pellet temperature, pseudo-steady state conditions, no temperature differences between solids and gases and the existence of a single reaction front, at the outer layer of M1 [78, 96, 97, 119]. Although some studies have developed USCM models with multiple reactive fronts, these models become increasingly more complex than the general UCSM model [78]. Therefore, these complex USCM models are considered to be beyond the scope of this thesis research.

Since the pellets used for the direct reduction of iron ore are initially porous, USCM is not the most accurate in describing the reduction kinetics. Another type of model that does take into account the porosity of the pellets is GM [12, 13, 46, 50, 82, 87, 96, 109, 111, 118, 119]. The GM considers all reduction reactions to occur sequentially and parallel throughout the pellet. The idea behind GM is shown in Figure 3.2. Basically, an iron oxide pellet consists of millions of smaller particles, called grains. All these grains can react independently, hence no unreacted core or no single reaction front is present. On account of the uniformity of the reducing gases throughout the pellets, mass transfer limitations play a smaller role for GM than for USCM [46, 82, 96, 97, 109, 118]. Due to the absence of a single reaction front, grain and pellet size does not have a direct influence on mass transfer limitations while it does have an effect on the overall reaction time of the reduction. Since the GM provides more accurate results than application of the USCM, the kinetic model in this thesis research is based on the GM.

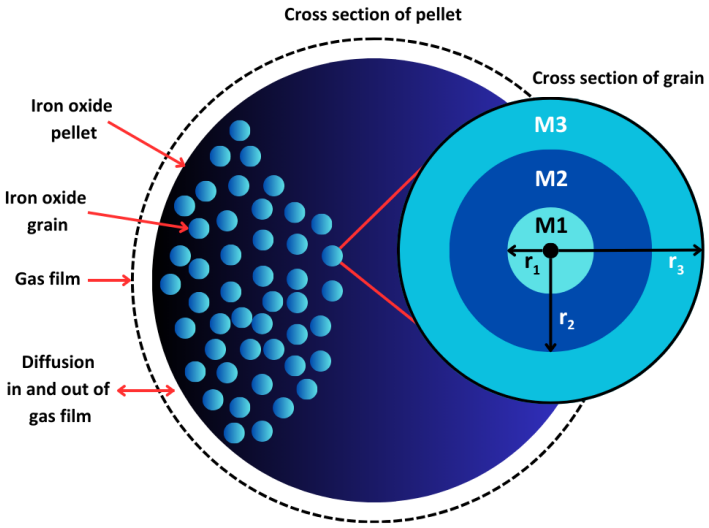


**Figure 3.2:** A schematic overview of GM [96]. A single iron oxide pellet consists of millions of smaller grains that can react independently and simultaneously. M1, M2 and M3 represent the different product layers of the iron oxides, while $r_1$, $r_2$ and $r_3$ represent the distances to the centre of the grain for their respective product layer. Gases need to diffuse into the gas film before engaging in reduction reactions, but gas distribution inside of the pellets is assumed to be uniform.

In summary, the Grain Model for the reduction of iron oxide pellets:

- Considers both sequential and parallel reactions
- Assumes that a single pellet consists of many independently but simultaneously reducing grains
- Applies for porous pellets, with deep reducing gas penetration depths
- Is less sensitive to mass transfer limitations than USCM
- Is less dependent on the initially chosen pellet and grain radii than USCM

### 3.2.2. Diffusivity of Gases in Porous Solids

Gas diffusion through a porous solid can be described by two types of diffusion: molecular diffusion and Knudsen diffusion. In Table 3.1, the range at which the diffusion types are dominant is presented. When the pores of the porous solid are smaller than 0.1 μm, molecular diffusion is dominant [117]. If the pores of the porous solid are larger than 10 μm, Knudsen diffusion dominates [117]. Whenever the pores of the solid are in between 0.1 and 10 μm, a mixed regime is considered in which both types of diffusion need to be taken into account [117]. Experimental work indicates that the average pore size of

hematite pellets usually lies somewhere between 7 to 11 μm [10, 76]. This lies in or is close to the mixed diffusion regime. In other work it is suggested that the pores of low grade iron ore are even smaller, in the region of 2 to 4 μm [122]. For simplicity, in this thesis it is further assumed that all pores of hematite and of the iron oxide intermediates are smaller than 10 μm and lie in the mixed diffusion regime.

**Table 3.1:** Knudsen and molecular diffusion regimes for porous solids [117]. With a pore size of the solid in between 0.1 and 10 μm, both Knudsen and molecular diffusion are considered. This is denoted by the mixed regime.

| **Diffusion regime** | *Pore size* / [μm] |
|---|---|
| Molecular diffusion | < 0.1 |
| Mixed regime | 0.1 - 10 |
| Knudsen diffusion | > 10 |

The Knudsen diffusion is only valid when the pore diameter is smaller than the mean free path length of the molecule. For calculations on the validity of the Knudsen diffusion, Appendix C should be consulted. There it is shown that Knudsen diffusion indeed holds up for the gas molecules for the reduction and carburization reactions: $H_2, CO, CH_4, H_2O$ and $CO_2$. For an arbitrary gas A, the molecular diffusion and Knudsen diffusion can be calculated via Equation (3.3) and Equation (3.4) respectively [96, 117]:

$$D_{\mathrm{A,m}} = \frac{1 - y_{\mathrm{A}}}{\sum_{j=B,C,\ldots}^{n} \frac{y_j}{D_{\mathrm{A}j}}} \tag{3.3}$$

$$D_{\mathrm{A,Kn}} = \frac{4}{3} K_{0,\mathrm{A}} \sqrt{\frac{8\,RT}{\pi\, M_{\mathrm{w,A}}}} \tag{3.4}$$

The molecular diffusion of gas A through a gas $j = B,C,...$ in a mixture of $n$ gases in [$m^2$/s] is shown in Equation (3.3) and is a function of the dimensionless mole fraction of both gases, $y_{\mathrm{A}}$ and $y_j$, and the binary diffusion coefficient $D_{\mathrm{A}j}$ of gas A through stationary gas $j$ in [$m^2$/s]. The formula for molecular diffusion is valid when we consider gas A to be the only dynamic or diffusing gas, while the other gases ($B$, $C$, ...) are assumed to be stationary. Another condition for this equation to be valid is that the pressure must not exceed 10 atm [117]. The Knudsen diffusion given in Equation (3.4) in [$m^2$/s] is a function of the Knudsen diffusion coefficient $K_0$ in [m] and an approximation of the mean velocity of the gas in [m/s]. The approximation of the mean velocity of the gas is given as the square root of gas constant $R$ in [kJ/(mol·K)], temperature $T$ in [K] and the molecular weight of gas A as $M_{\mathrm{w,A}}$ in [g/mol].

When combined, molecular diffusion and Knudsen diffusion can be considered as a series resistance. At first, the gas must diffuse to the surface of the pellet from inside of the bulk gas phase, which can be described by molecular diffusion. Then, the gas needs to enter the inter-granular pores of the pellet, which can be described via Knudsen diffusion. Therefore, the total pore diffusion when considering both types of diffusion can be calculated via the relationship for a resistance in series [117]:

$$\frac{1}{D_{j,\mathrm{pore}}} = \frac{1}{D_{j,\mathrm{m}}} + \frac{1}{D_{j,\mathrm{Kn}}} \tag{3.5}$$

In Equation (3.5), all the types of diffusion (pore, molecular and Knudsen) are given in [$m^2$/s]. From the pore diffusion of a gas, it is possible to calculate the effective diffusivity by multiplying with the porosity of the pellet squared [96, 117].

$$D_{j,\mathrm{eff}} = {\epsilon_{\mathrm{p}}}^2 \cdot D_{j,\mathrm{pore}} \tag{3.6}$$

The porosity of the pellet $\epsilon_{\mathrm{p}}$ is dimensionless, while the diffusivities are given in [$m^2$/s]. Based on Equation (3.6), it is possible to calculate the effective diffusivities of different compositions of gases through porous solids with varying porosities. When the iron oxide solid reduces from $Fe_2O_3$ to $Fe_3O_4$, $Fe_{0.95}O$ or Fe the radius, density and porosity of the pellet change. These parameters are related to one another, and hence the porosity of a pellet can be estimated via the relationship proposed by Niksiar and Rahimi [80]:

$$\epsilon_{\mathrm{p}} = 1 - \left( \left( \frac{R_{\mathrm{g}}}{R_{\mathrm{g0}}} \right)^3 (1 - \epsilon_{\mathrm{p0}}) \right) \tag{3.7}$$

In Equation (3.7), the dimensionless pellet porosity $\epsilon_{\mathrm{p}}$ can be calculated through the dimensionless initial pellet porosity $\epsilon_{\mathrm{p0}}$, grain radius $R_{\mathrm{g}}$ in [m] and initial grain radius $R_{\mathrm{g0}}$ in [m].

### 3.2.3. Kinetic Reaction Rate Modelling

After the diffusion of the gases into the solid iron oxide pellets, the reduction reactions can occur. As is explained in Section 2.2, only the reduction of hematite ($Fe_2O_3$) and wustite ($Fe_{0.95}O$) is considered for the modelling of the direct reduction process. For the reduction reactions of iron ore, the kinetic model of Rahimi and Niksiar [96] is applied. In this model, the reaction rates are a function of the concentration difference between $H_2$ and $H_2O$ or CO and $CO_2$, respectively. The model proposed by Rahimi and Niksiar [96] is based on the GM and is valid under the following assumptions:

- The gases and solids exhibit plug flow behaviour
- Reduction reaction rates are modelled in 2D
- The size of the pellets fed into the shaft furnace is constant
- The chemical reactions take place at the surface of the grains
- The temperature within a single grain is uniform
- The temperature of the solids and gases inside of a single pellet are uniform

The reaction formulas of hematite ($Fe_2O_3$) and wustite ($Fe_{0.95}O$) reduction with $H_2$ and CO are given in Table 2.3. The reduction of $Fe_2O_3$ with $H_2$ is labelled *R1* and $Fe_2O_3$ reduction with CO is labelled *R2*. In the same manner, $Fe_{0.95}O$ reduction with $H_2$ is labelled *R3* and $Fe_{0.95}O$ reduction with CO is labelled *R4*. The reaction rate formulas for the direct reduction of $Fe_2O_3$ and $Fe_{0.95}O$ proposed by Rahimi and Niksiar [96] are:

$$v_1 = k_1 \left( C_{\mathrm{H_2}} - \frac{C_{\mathrm{H_2O}}}{K_{\mathrm{eq},1}} \right) \tag{3.8}$$

$$v_2 = k_2 \left( C_{\mathrm{CO}} - \frac{C_{\mathrm{CO_2}}}{K_{\mathrm{eq},2}} \right) \tag{3.9}$$

$$v_3 = k_3 \left( C_{\mathrm{H_2}} - \frac{C_{\mathrm{H_2O}}}{K_{\mathrm{eq},3}} \right) \tag{3.10}$$

$$v_4 = k_4 \left( C_{\mathrm{CO}} - \frac{C_{\mathrm{CO_2}}}{K_{\mathrm{eq},4}} \right) \tag{3.11}$$

The reaction rate $v_i$ for reaction $i$ is given in [mol/(m$^2$·s)] and is a function of mass transfer coefficient $k_i$ in [m/s], concentration of component $j$ as $C_j$ in [mol/m$^3$] and dimensionless equilibrium constant $K_{\mathrm{eq},i}$ for reaction $i$. It must be noted that the reduction reaction rates derived from Rahimi and Niksiar [96] are two dimensional. Nevertheless, the model still provides an overview of the kinetic differences between hematite and wustite reduction with $H_2$ and CO.

For both the bulk gas-phase and the carburization reactions, the kinetic model developed by Hamadeh, Mirgaux, and Patisson [50] is applied. This model estimates the rate of the reactions as a function of partial pressures and pellet porosity. Furthermore, this model is well explicated in literature, while the results obtained compare well to existing direct reduction process data [50]. The kinetic model of Hamadeh, Mirgaux, and Patisson [50] is based on the GM and has the following assumptions:

- The model assumes steady-state behaviour
- A two dimensional geometry inside the shaft furnace
- The model is axisymmetrical

- The pellet diameter of the $Fe_2O_3$ pellets fed-in from the top is constant
- The temperature inside of the pellets is uniform

Although in Table 2.3 three gas phase reactions are identified, it is evident from literature that two of these reactions are dominant [50]. SRM (*R6*) and WGS (*R7*) are the two reactions with the largest influence on the gas phase composition, while the influence of DR (*R8*) for the direct reduction of iron ore is limited. For simplicity DR is therefore mostly excluded in the kinetic reaction modelling in literature [50]. For SRM and WGS, the reaction rates derived from Hamadeh, Mirgaux, and Patisson [50] are:

$$v_6 = k_6 \, (1 - \epsilon_{\text{bed}}) \, (1 - \epsilon_{\text{p}}) \left( P_{\text{CH}_4} \, P_{\text{H}_2\text{O}} - \frac{P_{\text{CO}} \, {P_{\text{H}_2}}^3}{K_{\text{eq},6}} \right) \tag{3.12}$$

$$v_7 = k_7 \, (1 - \epsilon_{\text{bed}}) \, (1 - \epsilon_{\text{p}}) \left( P_{\text{CO}} \, P_{\text{H}_2\text{O}} - \frac{P_{\text{CO}_2} \, P_{\text{H}_2}}{K_{\text{eq},7}} \right) \tag{3.13}$$

$$v_7 = k'_7 \, \rho_{\text{c}} \, (1 - \epsilon_{\text{bed}}) \, (1 - \epsilon_{\text{p}}) \left( P_{\text{CO}} \, P_{\text{H}_2\text{O}} - \frac{P_{\text{CO}_2} \, P_{\text{H}_2}}{K_{\text{eq},7}} \right) \tag{3.14}$$

The reaction rate $v_i$ for reaction $i$ is obtained in [mol/(cm$^3$·s)] and is a function of rate constant $k_i$ in [mol/(cm$^3$·s)] for $k_6$ and $k_7$ and in [mol/(kg$_{\text{cat}}$·s)] for $k'_7$, $\epsilon_{\text{bed}}$ is the dimensionless porosity of the bed, $\epsilon_{\text{p}}$ is the dimensionless porosity of the pellet, $P_j$ is the partial pressure of component $j$ in [bar] and $K_{\text{eq},i}$ is the dimensionless equilibrium constant of reaction $i$. It must be noted that for the WGS, two reaction rate equations are given. This is due to the catalytic working of iron and the different iron oxides on the WGS reaction. At the surface of Fe and $Fe_{0.95}O$, Equation (3.13) applies. At the surface of $Fe_3O_4$ and $Fe_2O_3$, Equation (3.14) applies. The values for $k_i$ and $K_{\text{eq},i}$ for different pressures and temperatures were calculated and are tabulated in Appendix C. The bed porosity was assumed to be constant at $\epsilon_{\text{bed}} = 0.44$, in accordance with literature [50, 96]. The pellet porosity, $\epsilon_{\text{pellet}}$, varies during the iron oxide reduction. The relationship used to determine the porosity of a pellet was derived by [80] and is given in Section 3.2.2.

After the reduction of the hematite pellets to wustite and metallic iron in the upper part of the furnace, the reduced iron ore pellets are cooled in the bottom part of the shaft furnace by means of a cooling gas. This is also the part of the reactor where the carburization reactions take place. In Table 2.3, cementite ($Fe_3C$) formation is shown as *R5*. The reactions contributing to the formation of solid carbon are MC and BR, given in Table 2.3 as *R9* and *R10* respectively. CG (*R11*) is a reaction that consumes the solid carbon and converts it into $H_2$ and CO. CG mainly becomes important at temperatures above 1000°C and when large quantities of solid carbon are present, like in the coal-based BF steel production route [50]. On account of the moderate temperatures for DRI, CG is omitted from the kinetic modelling in this study.

Out of the kinetic model of Hamadeh, Mirgaux, and Patisson [50], the reaction rate equations for the carburization reactions were derived. These are a function of the carbon activity. Proposed by Chipman [28] in 1972, the carbon activity is an ideality factor that is related to the atomic ratio of carbon over iron. Via the relationship of Chipman [28] and the work of Ribeiro et al. [99], it is possible to make an estimation of the weight percentage of carbon that the direct reduced iron will have after carburization. The Chipman relationship is known as:

$$log(a_{\text{C},i}) = \frac{2300}{T} - 0,920 + \frac{3860}{T} \, C + log\left( \frac{C}{1 - C} \right) \tag{3.15}$$

In Equation (3.15), the logarithmic value of the dimensionless carbon activity is a function of $T$ in [K] and the dimensionless ratio of carbon over iron, $C = n_{\text{C}}/n_{\text{Fe}}$. Following the work of Chipman [28], Ribeiro et al. [99] established the relationship between the carbon activities and the chemical equilibrium of MC (*R9*) and BR (*R10*), given below:

$$a_{\text{C},9} = K_{\text{eq},9} \, \frac{P_{\text{CH}_4}}{{P_{\text{H}_2}}^2} \tag{3.16}$$

$$a_{\text{C},10} = K_{\text{eq},10} \, \frac{{P_{\text{CO}}}^2}{P_{\text{CO}_2}} \tag{3.17}$$

The dimensionless carbon activity $a_{C,i}$ for reaction $i$ can be calculated with the dimensionless equilibrium constant $K_{eq,i}$ and the partial pressures $P_j$ of constituent $j$ in [bar]. Subsequently, Hamadeh, Mirgaux, and Patisson [50] developed their kinetic reaction model of both carburization reactions as a function of the partial pressures and the carbon activity.

$$v_9 = \frac{k_9}{{P_{H_2}}^{1/2}} (1 - \epsilon_{bed}) (1 - \epsilon_p) \left( P_{CH_4} - \frac{{P_{H_2}}^2 a_{C,9}}{K_{eq,9}} \right) \tag{3.18}$$

$$v_{10} = \left( k_{10} {P_{H_2}}^{1/2} + k'_{10} \right) (1 - \epsilon_{bed}) (1 - \epsilon_p) \left( {P_{CO}}^2 - \frac{P_{CO_2} a_{C,10}}{K_{eq,10}} \right) \tag{3.19}$$

In Equation (3.18) and Equation (3.19) the reaction rate is in units of [mol/(m$^3$·s)] and is a function of rate constant $k_i$ (or $k'_i$) for reaction $i$ in [mol/(m$^3$·s)], partial pressures $P_j$ for component $j$ in [bar], the dimensionless porosity of the bed $\epsilon_{bed}$, the dimensionless porosity of the pellet $\epsilon_p$ and the dimensionless carbon activity of reaction $i$ as $a_{C,i}$ .

## 3.3. Techno-Economic Scenario Modelling

A techno-economic assessment is necessary to study whether the switch to green $H_2$ is an economically sound decision for TATA Steel IJmuiden. Many methods exist to compare different feedstocks for chemical processes, like the Levelized Cost of Hydrogen or the Levelized Cost of Energy. For an industrial process on the scale of $H_2$-based DRI production, not only the feedstock needs to be taken into account however. Different reducing gas feed-in compositions may require adjustments to existing processes, or maybe demand the construction of whole new systems and reactors. For example, direct reduction based on natural gas may include a $CO_2$ capture unit, while a process based solely on $H_2$ may incorporate an on-site electrolyzer. A model that incorporates the capital and operational expenditures, maintenance, labour and emission costs for different scenarios, is the framework of the Levelized Cost of Production (LCOP) proposed by Bhaskar et al. [15]. The LCOP can be calculated via:

$$LCOP = \frac{C_{capex}\, AF + C_{opex} + C_{maint} + C_{labour} + C_{emission}}{Annual\ steel\ production} \tag{3.20}$$

The LCOP is a function of the the capital expenditure $C_{capex}$, the annuity factor $AF$, operational expenditure $C_{opex}$, maintenance costs $C_{maint}$, labour costs $C_{labour}$ and emission costs $C_{emission}$. The other formulas, parameters and datasets used to solve this Equation (3.20) are given in Appendix D. After calculating the LCOP, different DRI scenarios can be compared in terms of the Carbon Mitigation Costs (CMC). The CMC basically estimates the costs of preventing $CO_2$ emissions, comparded to other steel production methods. The results for the CMC can be compared to current European emission prices to determine whether the alterations to the process are worth the investment in the end. The CMC can be calculated via:

$$CMC = \frac{LCOP_2 - LCOP_1}{Emissions_1 - Emissions_2} \tag{3.21}$$

In Equation (3.21), the CMC is a comparison between two steel production scenarios. For example, scenario 1 can be BF-based steel manufacturing, while scenario 2 can be $H_2$-based steel production. For the purpose of this thesis research, three different scenarios for the production of direct reduced iron with 100% $H_2$ are researched. These three scenarios are:

- **Scenario A:** 100% $H_2$-based DRI production, green $H_2$ import
- **Scenario B:** 100% $H_2$-based DRI production with compressed $H_2$ storage, grey $H_2$ production from an on-site electrolyzer by supplying grey grid electricity
- **Scenario C:** 100% $H_2$-based DRI production with compressed $H_2$ storage, green $H_2$ production from an on-site electrolyzer by supplying green electricity from wind farm

# 4

# Results & Discussion

In this chapter, the results of this thesis research will be presented and discussed. The DRI process itself is once again divided into three parts: the gas phase reactions, the iron ore reduction and the carburization reactions. In Section 4.1 the results for the thermodynamic equilibrium modelling of the gas phase reactions are presented, while Section 4.2 gives the results for the kinetic reaction modelling. This includes the gas phase reactions, reduction reactions and carburization reactions. At last, Section 4.3 provides the results for the techno-economic scenario modelling.

## 4.1. Thermodynamic Modelling of the Gas Phase

The thermodynamic modelling is split into three parts. At first, the results for the Gibbs free energy and enthalpy calculations are given in Section 4.1.1. Then, Section 4.1.2 presents the results for the Gibbs minimization of the reducing gas streams for both MLP and EMP processes. Finally, a parametric study was performed on the $H_2$/CO-ratio in the reducing gas stream, of which the results are given in Section 4.1.3.

### 4.1.1. Gibbs Free Energy and Enthalpy

The Gibbs free energies and standard enthalpy of reactions were calculated for the gas phase reactions as a function of temperature. In Figure 4.1a the Gibbs free energies are shown, while in Figure 4.1b the enthalpy of reactions are given. For all calculations, the pressure was set to 1 bar. It can be observed that the standard enthalpy of reaction is not highly sensitive to a change in temperature, while the standard Gibbs free energies do show a strong temperature-dependent relationship. When the Gibbs free energy is negative, a chemical reaction occurs spontaneous. On the other hand, a positive value for the Gibbs free energy implicates that a reaction is non-spontaneous. It can be observed in Figure 4.1a that the Gibbs free energies of all reactions reverse in the range of 900 K to 1000 K. This has implications on the direction of the gas phase reactions for both the bulk gas flow and carburization parts of the SF. In Figure 4.1b it can be noticed that in the gas phase, DR and SRM are highly endothermic, while WGS is exothermic. For carburization, it may be observed that CG and MC are endothermic, while BR is highly exothermic.

For the reduction reactions of $Fe_2O_3$ and $Fe_{0.95}O$ with $H_2$ and CO, the enthalpies of reaction are given in Figure 4.2. For the reduction reactions the pressure was set to P = 1 bar. Figure 4.2 shows that $Fe_{0.95}O$ reduction with $H_2$ is endothermic, while reduction of $Fe_2O_3$ with $H_2$ is exothermic. For a reduction temperature between 1100 K and 1200 K, the overall reduction of iron ore with $H_2$ is endothermic. Reduction of both hematite and wustite with CO is exothermic, hence overall reduction with only CO is highly exothermic.

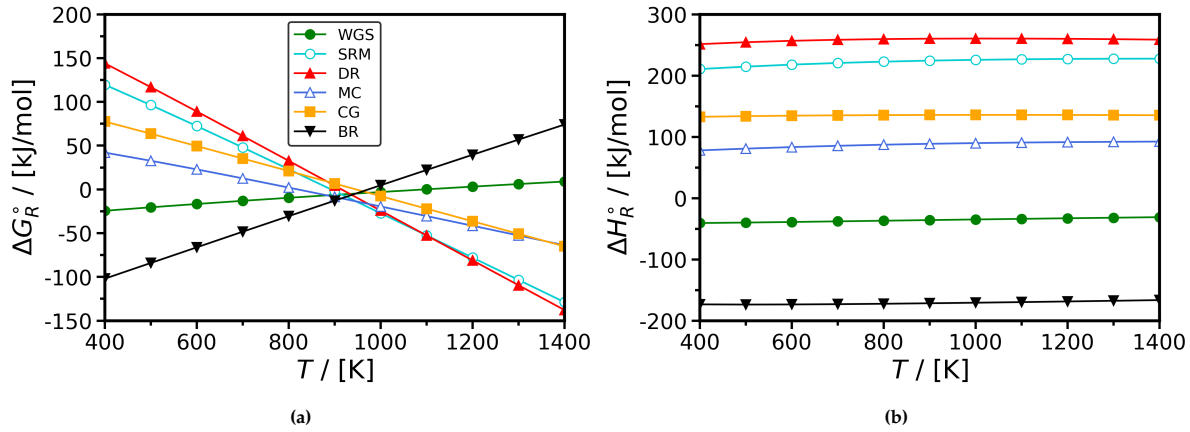


(a) (b)

**Figure 4.1: a)** The standard Gibbs free energies of reaction for all gas phase reactions mentioned in Table 2.3. **b)** The standard enthalpies of reaction for all gas phase reactions mentioned in Table 2.3. The legend of figure **a)** also applies to figure **b)**.

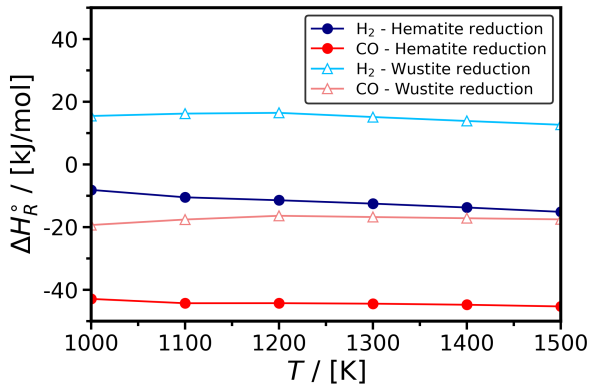


**Figure 4.2:** Standard enthalpy of reactions for $Fe_2O_3$ and $Fe_{0.95}O$ reduction with $H_2$ and CO. P = 1 bar.

### 4.1.2. Reducing Gas Streams

The reducing gas stream compositions for the MLP and EMP processes are given in Table 4.1. Over both of these gas phase compositions, a Gibbs minimization was performed. In both cases the temperature was varied in the direct reduction regime of 1000 K to 1250 K. For the MLP reducing gas composition, the results of the Gibbs minimization are shown in Figure 4.3a. It can be seen that for a pressure of 1.8 bar, no significant changes occur in the chemical equilibrium composition in the temperature range for direct reduction. In Figure 4.3b the results of the Gibbs minimization for the EMP reducing gas are shown. Although a slight variation of the equilibrium composition is observed between 1000 K and 1100 K, the chemical equilibrium composition for EMP is as good as constant after 1100 K. When the temperature range is extended to include temperatures from 600 K upwards, for both MLP and EMP the chemical equilibrium composition changes and $y_{H_2}$ and $y_{CO}$ decrease with a decrease in temperature. Since the reducing gases enter at temperatures of over 1100 K and the reduction finds place at approximately 1173 K, these lower temperatures are not taken into account for the Gibbs minimization.

**Table 4.1:** The pressure and molar fractions in the gas phase for the reducing gas streams for the MLP process of Appendix A.1 and the EMP process of Appendix A.4.

| | $P$/[bar] | $y_{CO}$/[-] | $y_{CO_2}$/[-] | $y_{H_2}$/[-] | $y_{H_2O}$/[-] | $y_{N_2}$/[-] | $y_{CH_4}$/[-] |
|---|---|---|---|---|---|---|---|
| **MLP** [91] | 1.84 | 0.35 | 0.02 | 0.54 | 0.05 | 0.01 | 0.03 |
| **EMP** [130] | 7.24 | 0.16 | 0.05 | 0.66 | 0.04 | 0.01 | 0.08 |

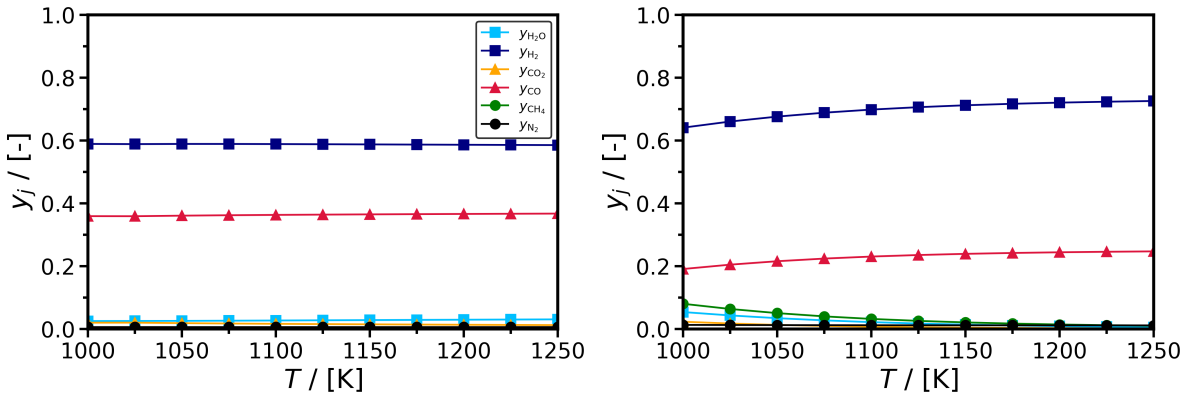


**(a)** **(b)**

**Figure 4.3: a)** Reducing gas composition at thermodynamic equilibrium of MLP as a function of temperature. P = 1.84 bar. **b)** Reducing gas composition at thermodynamic equilibrium of EMP as a function of temperature. P = 7.24 bar.

In addition to the Gibbs minimization as a function of temperature, also a Gibbs minimization as a function of pressure was performed on the MLP and EMP reducing gas streams. For the pressure dependent Gibbs minimization it was assumed that the reducing gases exist of $H_2$, CO and $N_2$ only. This will make the results comparable to the results of Section 4.1.3. The starting compositions for the MLP and EMP reducing gas streams for the pressure calculations are shown in Table 4.2, while the results of the Gibbs minimization with varying pressure are given in Figure 4.4. The pressure was varied within the direct reduction operating regime, from 1 bar to 8 bar. It is evident from both Figure 4.4a and Figure 4.4b that the pressure has no influence on the chemical equilibrium composition for both MLP and EMP reducing gas streams up to 8 bar.

**Table 4.2:** The temperature and molar fractions in the gas phase for the reducing gas streams for MLP and EMP.

| | $T$/[K] | $y_{CO}$/[-] | $y_{H_2}$/[-] | $y_{N_2}$/[-] |
|---|---|---|---|---|
| **MLP** [91] | 1113 | 0.35 | 0.54 | 0.11 |
| **EMP** [130] | 1235 | 0.16 | 0.66 | 0.18 |

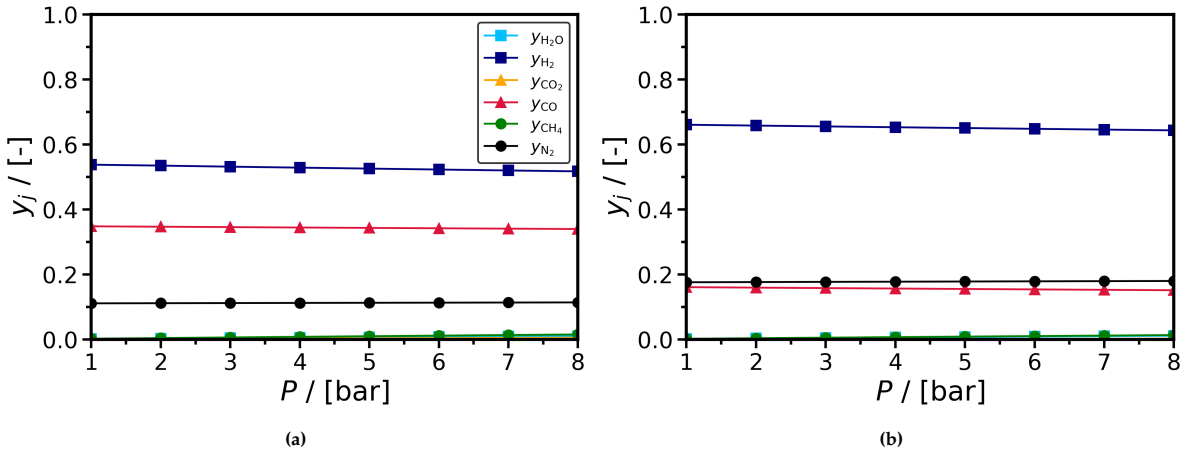


**(a)** **(b)**

**Figure 4.4: a)** Gas compositions at thermodynamic equilibrium for the MLP reducing stream of Table 4.2. **b)** Gas composition at thermodynamic equilibrium for the reducing EMP stream of Table 4.2.

### 4.1.3. $H_2$/CO-ratio

The MLP and EMP process have a $H_2$/CO-ratio of 1.55 and 4.09, respectively. A parametric study over this ratio was performed to determine the influence of both temperature and pressure on the mole fractions of $H_2$ and CO at chemical equilibrium. The input data for the Gibbs minimization on reducing gas streams with different $H_2$/CO-ratios are listed in Table 4.3. All gas phases are initially composed of $H_2$, CO and $N_2$ only. The $H_2$/CO-ratio is linearly increased from 1 to 9, while the mole fraction of $N_2$ is kept constant at 0.05 for all ratios. The results of the minimization on the mole fraction of CO are shown in Figure 4.5. For the mole fraction of $H_2$ in the gas phase, Figure 4.6 shows the results. In Figure 4.7 the results of the Gibbs minimization of the MLP and EMP processes are combined. For all results, the darker the colour, the higher the $H_2$/CO-ratio. Furthermore, for the temperature dependent calculations, P = 1 bar. For the graphs with pressure dependent calculations, T = 1173 K.

**Table 4.3:** The different $H_2$/CO-ratio reducing gas streams and their respective compositions.

| **$H_2$/CO-ratio** /[-] | $y_{H_2}$ /[-] | $y_{CO}$ /[-] | $y_{N_2}$ /[-] |
|---|---|---|---|
| 1 | 0.475 | 0.475 | 0.05 |
| 3 | 0.713 | 0.238 | 0.05 |
| 5 | 0.792 | 0.158 | 0.05 |
| 7 | 0.831 | 0.119 | 0.05 |
| 9 | 0.855 | 0.095 | 0.05 |

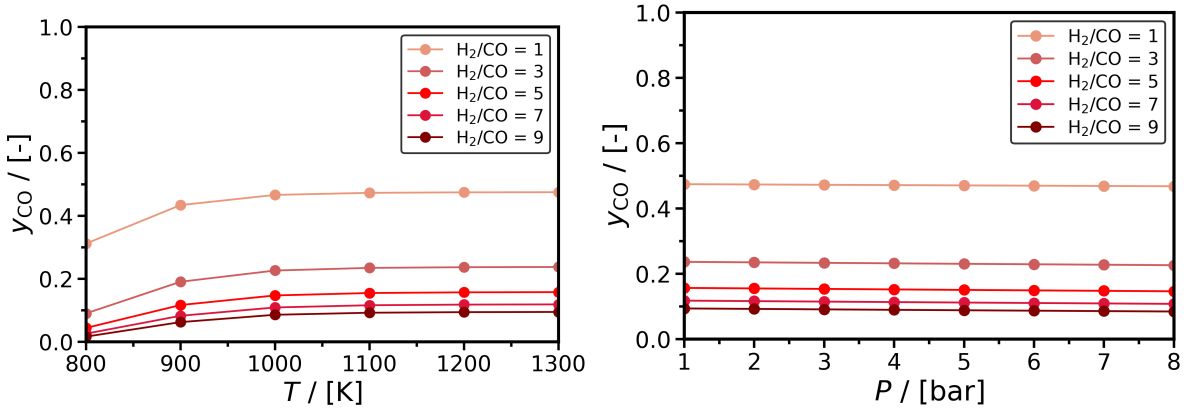


(a) (b)

**Figure 4.5: a)** The chemical equilibrium mole fractions $y_{CO}$ of the gas streams given in Table 4.3 as a function of temperature. P = 1 bar. **b)** The chemical equilibrium mole fractions $y_{CO}$ of the gas streams given in Table 4.3 as a function of pressure. T = 1173 K.

In Figure 4.5a it can be seen that the $y_{CO}$ increases from 800 K to 1000 K, while afterwards $y_{CO}$ is approximately constant. This is the same behaviour in relationship to pressure as observed in Section 4.1.2. Also, the almost non-existent variation of the mole fraction as function of pressure in Figure 4.5b is the same as in Section 4.1.2. It is apparent that an increase or decrease of $H_2$/CO-ratio has no direct influence on the relative chemical equilibrium composition. The absolute numbers do vary, but the ratio stays the same. The same observations hold for Figure 4.6a and Figure 4.6b, but then applied on $y_{H_2}$. The mole fraction $y_{H_2}$ keeps increasing from 800 K to 1000 K, while afterwards it remains as good as constant. The pressure decreases the equilibrium composition slightly, but $y_{H_2}$ almost remains constant in a pressure range of 1 bar to 8 bar. Although the initial $H_2$/CO-ratio ultimately effects the value for $y_{CO}$ and $y_{H_2}$, no effect of the $H_2$/CO-ratio on the equilibrium composition is observed.

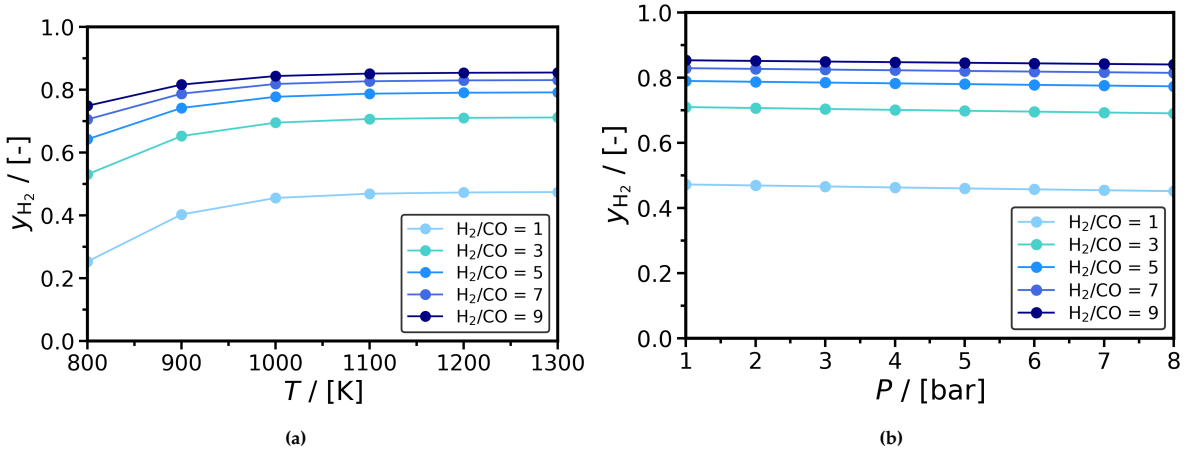


(a) (b)

**Figure 4.6: a)** The chemical equilibrium mole fractions $y_{H_2}$ of the gas streams given in Table 4.3 as a function of temperature. P = 1 bar. **b)** The chemical equilibrium mole fractions $y_{H_2}$ of the gas streams given in Table 4.3 as a function of pressure. T = 1173 K.

Figure 4.7a and Figure 4.7b present the results for the Gibbs minimization on $y_{CO}$ and $y_{H_2}$ versus temperature and pressure for the MLP and EMP reducing gas streams. After T > 1000 K and for the complete pressure range of 1 bar to 8 bar, the mole fractions in the gas phase can be assumed constant. Therefore, with all results considered, it can be concluded that a change in temperature in the 1100 K to 1250 K range has no effect on the chemical equilibrium composition. For a change in pressure from 1 bar to 8 bar, also no change in chemical equilibrium is observed. For the DRI process however, it is known that the condition of chemical equilibrium is not attained since the residence time of the gases is not long enough. Therefore, the chemical reactions must also be studied kinetically, since then it becomes possible to determine their behaviour on a shorter timescale.

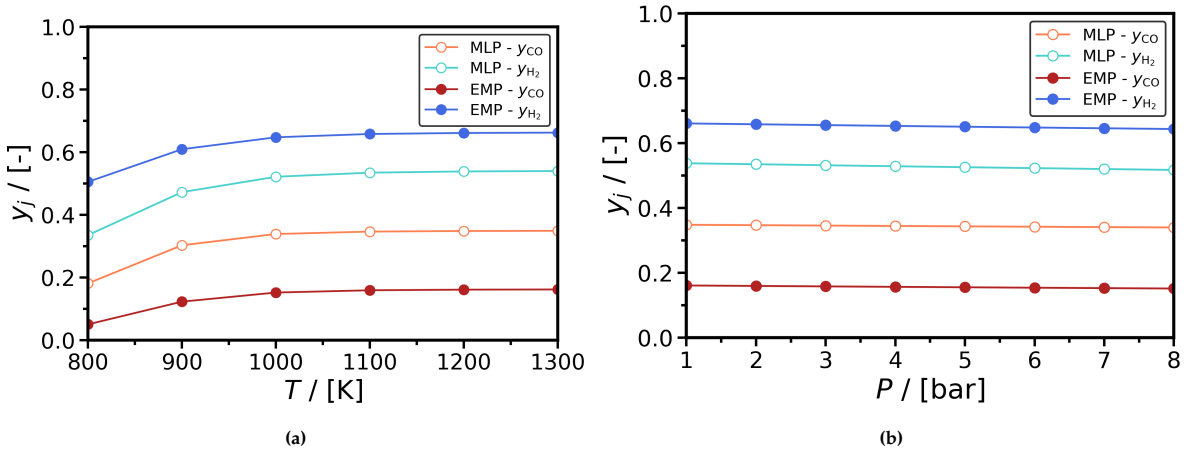


(a) (b)

**Figure 4.7: a)** The chemical equilibrium mole fractions $y_{H_2}$ and $y_{CO}$ of the MLP and EMP processes as a function of temperature. P = 1 bar. **b)** The chemical equilibrium mole fractions $y_{H_2}$ and $y_{CO}$ of the MLP and EMP processes as a function of pressure. T = 1173 K.

## 4.2. Kinetic Reaction Modelling

The kinetic reaction modelling of the DRI process is divided into three parts: the kinetic reactions in the bulk gas phase, the reduction of the iron ore and the carburization reactions. In Section 4.2.1 the results for the bulk gas phase reactions are given, while in Section 4.2.2 the results of the iron ore reduction is shown. Then in Section 4.2.3 the results for the carburization kinetics will be presented. For the reduction and carburization reactions, also the diffusivity of the gases is modelled. At last, the results will be compared with available literature in Section 4.2.4.

### 4.2.1. Bulk Gas Phase Reactions

For the gas phase reaction of the MLP and the EMP processes, the reaction rates for SRM and WGS were calculated as functions of temperature and pressure. It must be noted that for WGS, only the reaction rate with Fe as catalyst gave actual results. The reaction rates for WGS on $Fe_2O_3$, $Fe_3O_4$ and $Fe_{0.95}O$ gave values of practically zero. Therefore, only the WGS on Fe is considered for the results of the bulk gas phase reactions in this chapter. This is valid for both MLP and EMP processes. For the calculations of the partial pressures, the mole fractions of the reducing gas streams given in Table 4.1 were applied. The results for the MLP process are given in Figure 4.8, Figure 4.9a and Figure 4.9b. In Figure 4.8, the reaction rates for SRM and WGS on Fe are depicted over a temperature range of 1000 K to 1300 K. The pressure is assumed to be constant, at 1.8 bar. In Figure 4.9a and Figure 4.9b the temperature is varied to 1123 K, 1173 K and 1223 K. The chemical reaction formulas for both SRM and WGS are given next to the graph, on the right. When $v_i > 0$, the reactions shift towards the top, while the reactions shift towards the bottom if $v_i < 0$.

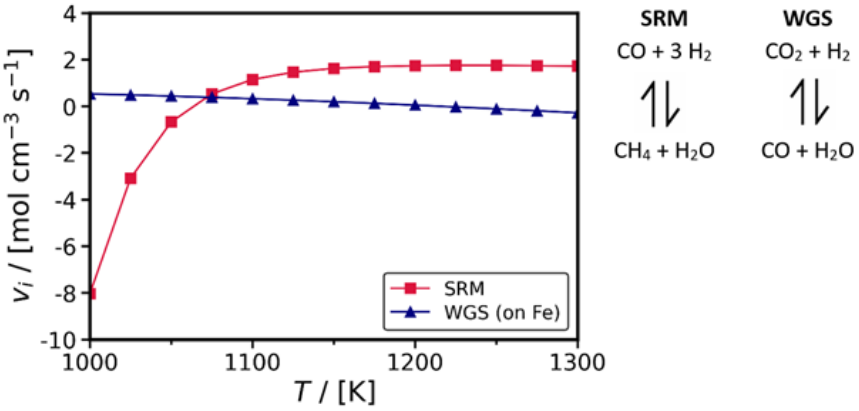


**Figure 4.8:** The reaction rates of SRM versus the WGS on Fe as a function of temperature for the MLP process. P = 1.8 bar. Next to the graph on the right, the chemical reaction formulas for SRM and WGS are shown. When $v_i > 0$, the reactions shift towards the top, while the reactions shift towards the bottom if $v_i < 0$.

Out of Figure 4.8 it is apparent that for temperatures in the range of 1100 K to 1250 K, SRM is the dominant gas phase reaction while WGS on Fe is close to zero. This implies that for this temperature range with P = 1.8 bar, a feed-in of natural gas leads to the production of $H_2$ and CO. Since reforming takes place *in situ*, it can be observed for MLP that no external reformer is required to reform natural gas to a syngas mixture before feeding into the SF. This can prove to be interesting in the early stages of DRI developments, when natural gas-based DRI (NG-DRI) may prove to be economically favourable over a fully $H_2$-based DRI process. The absence of an external reformer in the balance of plant can also lower the LCOP of the MLP process.

In Figure 4.9a, the SRM reaction rate for the MLP reducing gas is shown as a function of pressure. Meanwhile, temperature is also varied by 50 K around the optimal reduction temperature of 1173 K. Therefore, the SRM reaction rate is plotted for 1123 K, 1173 K and 1223 K. It is shown in Figure 4.9a that, for an increase in pressure, a higher temperature is required for the reaction rate of SRM to remain positive. For the MLP process, it is seen that a temperature of 1173 K is not sufficient to have internal reforming inside the SF. A temperature of 1223 K presents a better case for internal reforming, as the reaction rate of SRM keeps increasing for an increase in pressure up to P = 7 bar. In Figure 4.9b it is seen that an increase in pressure at T = 1123 K and T = 1173 K leads to an increase in the reaction rate for WGS. This implicates that CO and $H_2O$ are consumed and $H_2$ and $CO_2$ are produced, which is advantageous for the DRI process. On the other hand, if the temperature for WGS is increased to T = 1223 K, the reaction rate becomes slightly negative for the complete pressure range of 1 bar to 8 bar.

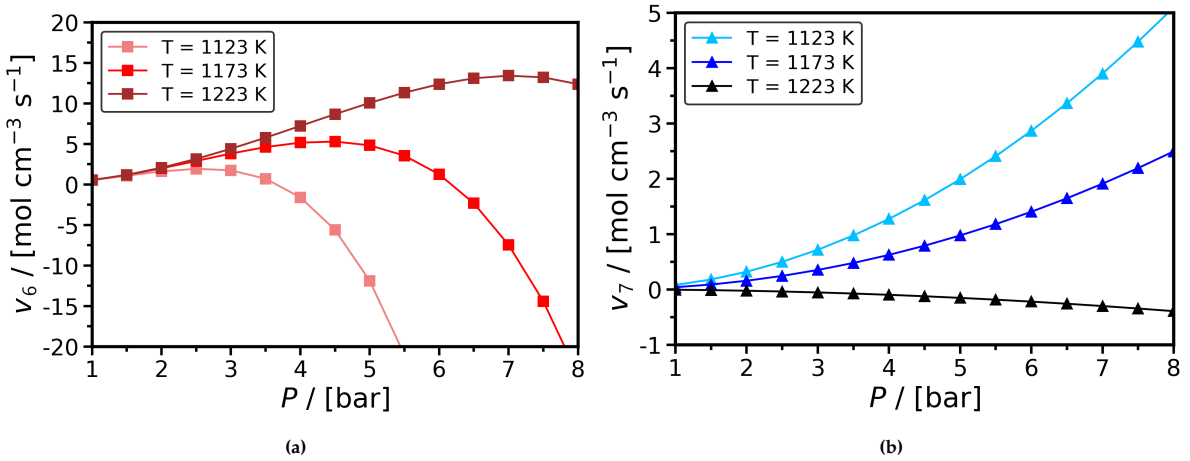


(a) (b)

**Figure 4.9: a)** Reaction rates of SRM as a function of pressure for the MLP process. **b)** Reaction rates of WGS on Fe as a function of pressure for the MLP process.

In conclusion, it can be observed in Figure 4.8 that for the reducing gas composition and pressure for MLP given in Table 4.1, internal reforming of natural gas is possible for T > 1100 K. Hence, the MLP process has the potential to start off with a feed-in of mainly natural gas in the reducing stream. Then, the $H_2$ mole fraction can gradually be increased. This can be an option if at first it is difficult to acquire sufficient green $H_2$ for a complete green DRI process. Subsequently, it can be seen in Figure 4.9a that for the reducing gas stream of MLP in the pressure range of the EMP process (6 bar to 8 bar), internal reforming becomes a possibility for T = 1223 K. For T = 1173 K, the reaction rate of SRM is negative and no reforming of $CH_4$ can occur.

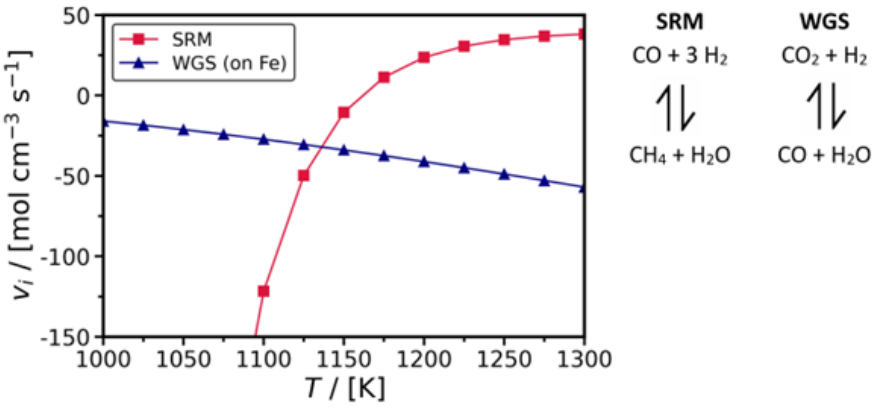


**Figure 4.10:** Reaction rates of SRM versus WGS on Fe as a function of temperature for the EMP process. P = 7.2 bar. Next to the graph on the right, the chemical reaction formulas for SRM and WGS are shown. When $v_i > 0$, the reactions shift towards the top, while the reactions shift towards the bottom if $v_i < 0$.

For the EMP process the results for the reaction rates of SRM and WGS on Fe are shown in Figure 4.10, Figure 4.11a and Figure 4.11b. In Figure 4.10, the chemical reaction formulas for SRM and WGS are shown next to the graph on the right. When $v_i > 0$, the reactions shift towards the top, while the reactions shift towards the bottom if $v_i < 0$. The composition of the reducing gas applied for EMP is given in Table 4.1. The temperature in Figure 4.10 is increased from 1000 K to 1300 K, while the pressure in Figure 4.11a and Figure 4.11b is increased from 1 bar to 8 bar. When comparing Figure 4.8 with Figure 4.10, it is seen that the change in pressure and reducing gas composition leads to higher and lower reaction rates for SRM and WGS on Fe. Whereas for MLP the reaction rate for SRM at T = 1173 K equals 1.7 mol/(cm$^3$·s), for EMP that already amounts to 11 mol/(cm$^3$·s). At T = 1223 K, the SRM reaction rate has even increased to 31 mol/(cm$^3$·s) for EMP, while for MLP it remains at 1.8 mol/(cm$^3$·s). The WGS on Fe eventually reaches values of -57 mol/(cm$^3$·s) for EMP and -0.3 mol/(cm$^3$·s) for MLP.

From Figure 4.10 it becomes evident that for internal reforming of natural gas a temperature of at least T = 1173 K is needed for the reducing gas of EMP. At this temperature however, WGS is highly negative. This leads to a decrease in the overall $H_2$ concentration. Therefore, internal reforming does not look like a viable option for the EMP process and most likely an internal reformer is necessary to operate the process with an in put of natural gas.

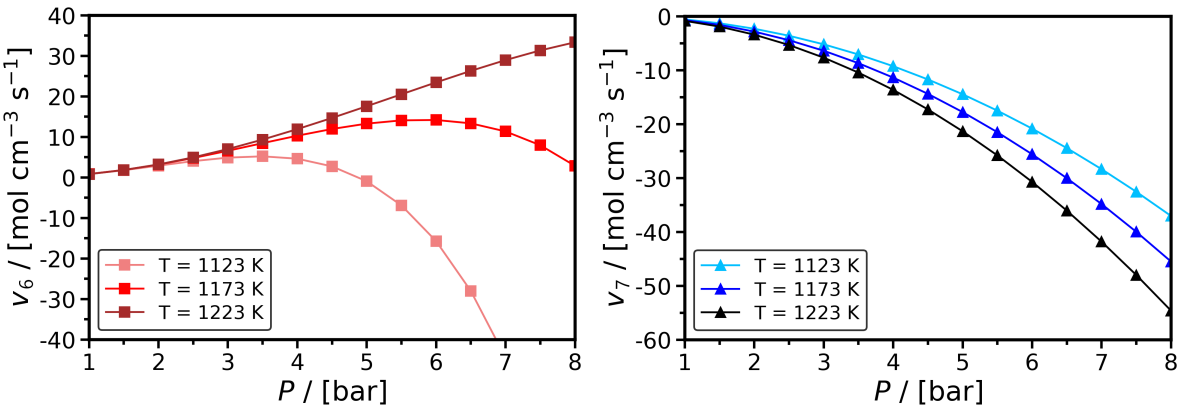


**Figure 4.11: a)** Reaction rates of SRM as a function of pressure for the EMP process. **b)** Reaction rates of WGS on Fe as a function of pressure for the EMP process.

In Figure 4.11a the same SRM behaviour can be observed for EMP as for MLP, but once again with higher positive and negative reaction rates. An increase in pressure only leads to a positive SRM reaction rate when at least T = 1173 K. For T = 1173 K, the SRM reaction rate does approach zero for P = 8 bar. Therefore, a higher T is proposed for internal natural gas reforming.

Figure 4.11b shows that the reaction rates for WGS on Fe remain negative and get increasingly more negative with an increase in temperature. Due to the highly negative values for the reaction rate of the WGS at P = 6 bar and P = 8 bar, it is a possibility that $H_2$ production by SRM is canceled out by the reverse WGS. Therefore, more research on this topic is advised if internal reforming of natural gas is preferred in the early stages of DRI operation.

In conclusion, the reaction rates for EMP are of a higher order than MLP. For the reducing gas compositon of EMP at lower pressures this does not prove to be an issue if internal reforming is desired. At higher pressures however, there is a possibility that SRM and WGS compete with one another which can lead to a decrease in $H_2$ concentration in the SF which has a negative effect on DRI.

### 4.2.2. Iron Ore Reduction

Before the reducing gases reach the iron oxide reaction front, diffusion must take place. The gases diffuse from the bulk gas phase onto the iron ore pellets, after which they diffuse through the solid pores. Every iron oxide intermediate exhibits its own porosity that can be calculated through the densities and pellet radii. The results of the porosity calculations are given in Table 4.4. The results for the diffusivities of the reducing gases for the reduction of the iron oxides are given in Figure 4.12 and Figure 4.13. It is seen in all four graphs that diffusion of $H_2$ has the highest diffusivity and that diffusion of $CO_2$ has the lowest. Furthermore, despite the higher $H_2$ concentration in the reducing gas of EMP compared to MLP, the diffusivity of $H_2$ in both processes appears to be the same. The same holds for the higher CO concentration in the reducing gas stream of the MLP process compared to the EMP process. An increase in pressure leads to a decrease of the diffusivity of all gases. Meanwhile an increase in temperature shows a slow but steady linear increase of effective diffusivities for all gases. At P = 1 bar, the diffusivity of $H_2$ is close to 3.5 times higher than the diffusivity of CO. For P = 8 bar, $H_2$ diffusion is approximately 1.6 times higher than diffusion of CO. From these

diffusivities, it can be deducted that reduction with $H_2$ has a higher reaction rate than reduction with CO.

**Table 4.4:** Iron oxide intermediates and their respective porosities [76]. Porosity is a measure of the void fraction, or empty space, in a solid material. It is the ratio of the volume of the void fraction over the total volume of the solid. A high porosity indicates a high void fraction and vice versa.

| **Iron Oxide Intermediate** | **Chemical Formula** | *Porosity* / [-] |
|---|---|---|
| Hematite | $Fe_2O_3$ | 0.22 |
| Wustite | $Fe_{0.95}O$ | 0.33 |
| Metallic iron | Fe | 0.64 |

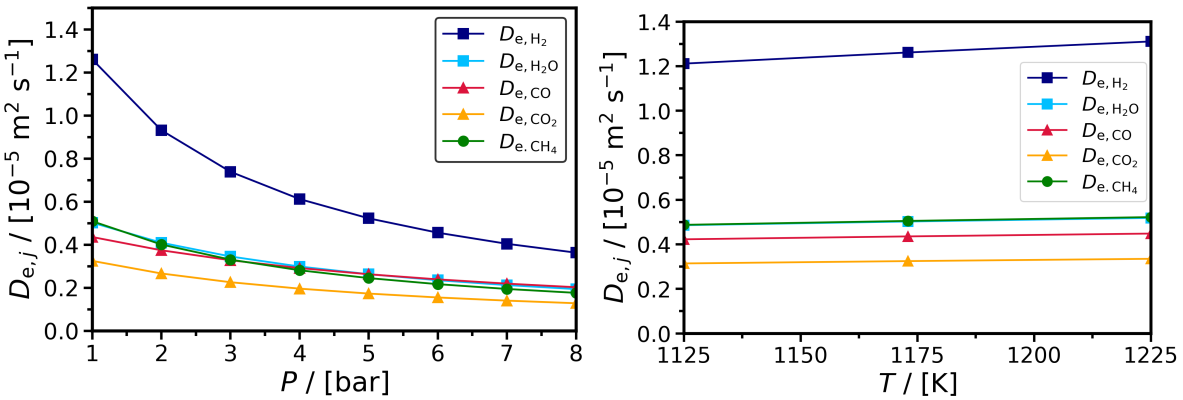


(a) (b)

**Figure 4.12: a)** Effective diffusivities as a function of pressure for the gases in the reducing stream of the MLP process. T = 1173 K. **b)** Effective diffusivities as a function of temperature for the gases in the reducing stream of the MLP process. P = 1.8 bar.

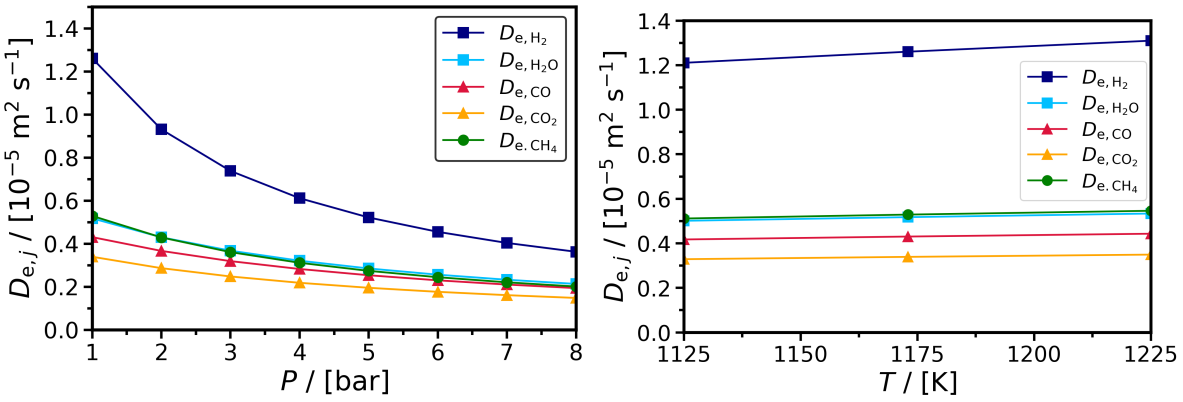


(a) (b)

**Figure 4.13: a)** Effective diffusivities as a function of pressure for the gases in the reducing stream of the EMP process. T = 1173 K. **b)** Effective diffusivities as a function of temperature for the gases in the reducing stream of the EMP process. P = 7.2 bar.

The results for the kinetic modelling of hematite and wustite reduction by $H_2$ and CO for the MLP process are shown in Figure 4.14a and Figure 4.14b, respectively. For both iron oxides, it is evident from Figure 4.14 that reduction with $H_2$ has a higher reduction rate than reduction with CO.

In Figure 4.15a, the ratio of the reaction rates of hematite over wustite reduction for MLP is given. The results are shown for reduction with $H_2$ (blue) and reduction with CO (red). When this ratio is smaller than one, it is implied that reduction of wustite has a higher reaction rate than the reduction of hematite. Hence, hematite reduction is then rate-determining. When this ratio is greater than one, hematite

reduction has the higher reaction rate, which implies that wustite reduction is rate-determining. For reduction with $H_2$, wustite reduction is the rate-determining step for temperatures well up to 1250 K. For reduction with CO, hematite reduction becomes rate-determining at 1100 K.

In Figure 4.15b, the ratio of $H_2$/CO reduction is shown. For both hematite and wustite reduction, reduction with $H_2$ has a higher reduction rate for the complete temperature range of 1000 K to 1300 K. When the temperature increases, the reaction rate of $H_2$ reduction increases quicker than the reaction rate of CO reduction. This results in a higher $H_2$/CO reduction rate ratio for higher temperatures. At T = 1173 K, hematite reduction with $H_2$ is a factor 1.7 higher than reduction with CO. For wustite reduction at T = 1173 K, $H_2$ reduction is 1.5 times faster than CO reduction.

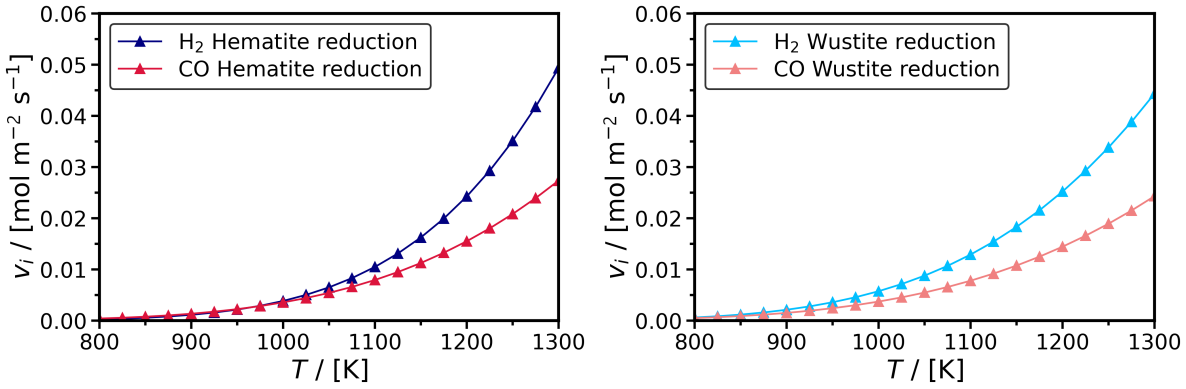


**Figure 4.14: a)** Reaction rates as function of temperature of hematite reduction for the MLP process. Reduction with $H_2$ in blue, reduction with CO in red. **b)** Reaction rates as function of temperature of wustite reduction for the MLP process. Reduction with $H_2$ in light blue, reduction with CO in pink.

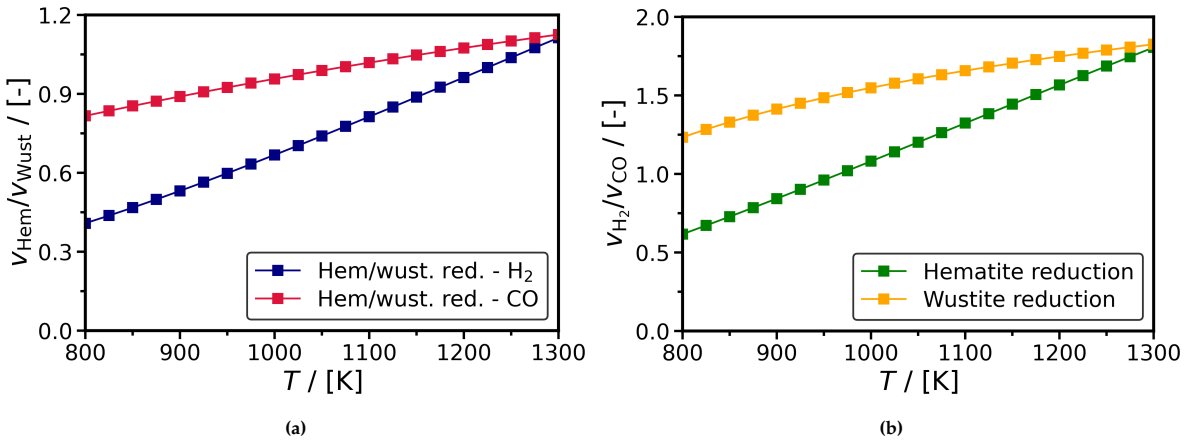


**Figure 4.15: a)** Ratio of reaction rates of hematite reduction over wustite reduction for the MLP process. Reduction with $H_2$ in blue, reduction with CO in red. **b)** Ratio of reaction rates of $H_2$ reduction over CO reduction for the MLP process. Reduction of hematite in green, reduction of wustite in yellow.

For the EMP process, the reaction rates for hematite and wustite reduction by $H_2$ and CO are shown in Figure 4.16a and Figure 4.16b. It is apparent that reduction of both hematite and wustite with $H_2$ has a higher reaction rate than reduction with CO. When Figure 4.16 is compared to Figure 4.14, it can be seen that the $H_2$ reaction rates for EMP are of a higher order than MLP. This can be contributed to the higher pressure of the process and the higher amount of $H_2$ in the gas phase, as given in Table 4.1. The lower $y_{CO}$ of EMP causes the CO reduction rates for hematite and wustite reduction with CO to appear lower than the MLP reduction rates.

In Figure 4.17a the ratio of the reaction rates of hematite over wustite reduction for EMP is given. Reduction with $H_2$ shows a higher reaction rate for wustite reduction for temperatures up to 1250 K. Hence, for $H_2$ reduction it appears that hematite reduction is rate-determining. Reduction with CO exhibits a higher reduction rate for hematite reduction than for wustite reduction. At T = 1173 K, hematite reduction with CO has a two times higher reaction rate than wustite reduction. For CO reduction in the EMP process, wustite reduction is rate-determining.

Figure 4.16b shows that reduction with $H_2$ exhibits higher reaction rates than reduction with CO for EMP. At T = 1173 K, hematite reduction with $H_2$ has a four times higher reduction rate than reduction with CO. For T = 1173 K for wustite reduction, reduction with $H_2$ even has a nine times higher reduction rate than CO reduction.

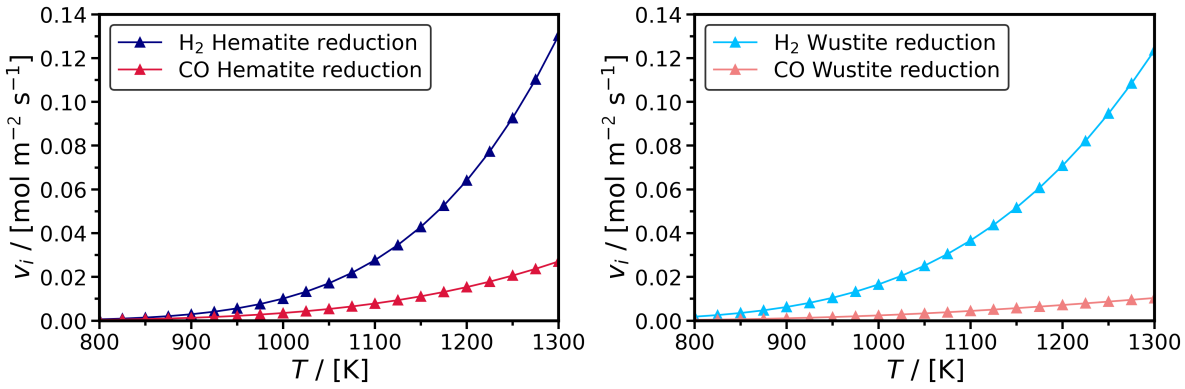


(a) (b)

**Figure 4.16: a)** Reaction rates as function of temperature of hematite reduction for the EMP process. Reduction with $H_2$ in blue, reduction with CO in red. **b)** Reaction rates as function of temperature of wustite reduction for the EMP process. Reduction with $H_2$ in light blue, reduction with CO in pink.

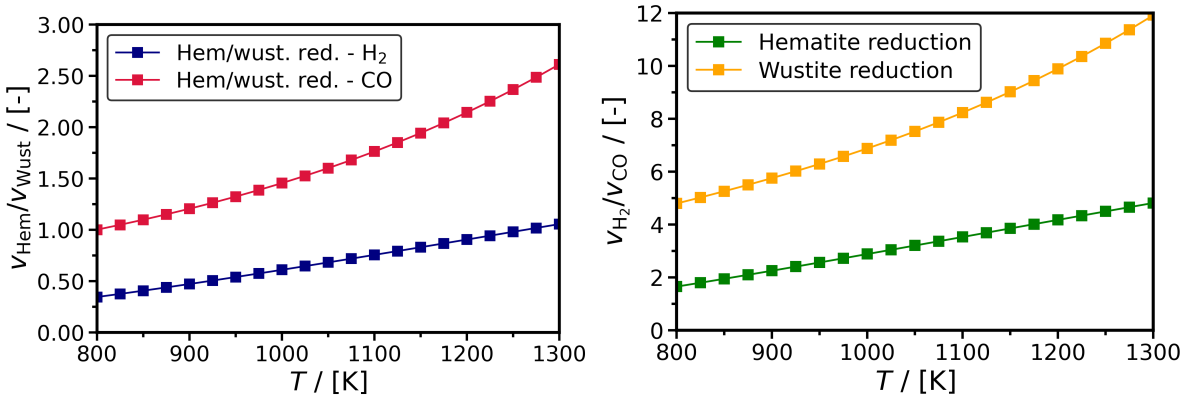


(a) (b)

**Figure 4.17: a)** Ratio of reaction rates of hematite reduction over wustite reduction for the EMP process. Reduction with $H_2$ in blue, reduction with CO in red. **b)** Ratio of reaction rates of $H_2$ reduction over CO reduction for the EMP process. Reduction of hematite in green, reduction of wustite in yellow.

In conclusion, it is apparent that a higher mole fraction of $H_2$ in the reducing gas stream in combination with an increased pressure leads to two to three times higher reaction rates. For the MLP process reduction with CO only has a slightly higher reaction rate compared to EMP, despite having at least a two times higher CO mole fraction. For both MLP and EMP, reduction with $H_2$ is dominant over reduction with CO. When reducing with CO, wustite reduction is rate-determining in the range of 1000 K to 1300 K. Reduction with $H_2$ for both MLP and EMP sees wustite reduction as rate-determining. More details on the validity of the applied model of Rahimi and Niksiar [96] is discussed in Section 4.2.4.

### 4.2.3. Carburization Reactions

For the calculations of the diffusion and the carburization reactions, the cooling gas data of Table 4.5 is used. It is immediately evident from the MLP and EMP stream data that there is more $CH_4$ than CO in both cooling gas streams. For EMP, even no CO is present and only $CH_4$ is used for cooling and carburization. In the MLP cooling gas $y_{H_2}$ is high since it amounts to 0.55. The results for the diffusion of the cooling gas for the MLP process are shown in Figure 4.18. For the cooling gas of EMP no diffusion calculations were performed, since of the carburizing agents only $CH_4$ is present in the gas composition. Therefore, no diffusion comparison is necessary to describe the carburization behaviour. From Figure 4.18 it is apparent that diffusion of $CH_4$ occurs at a higher rate than CO diffusion, for low and medium pressures and temperatures. This indicates that $CH_4$ has a higher carburization potential than CO.

**Table 4.5:** The pressure and molar fractions in the gas phase for the cooling gas streams for the MLP process of Appendix A.1 and the EMP process of Appendix A.4. The reducing gas stream is labeled as *'Stream 8'* in the appendix.

| | $P$/[bar] | $y_{CO}$/[-] | $y_{CO_2}$/[-] | $y_{H_2}$/[-] | $y_{H_2O}$/[-] | $y_{N_2}$/[-] | $y_{CH_4}$/[-] |
|---|---|---|---|---|---|---|---|
| **MLP** [91] | 1.96 | 0.03 | 0.01 | 0.55 | 0.04 | 0.11 | 0.26 |
| **EMP** [130] | 8.89 | 0.00 | 0.00 | 0.00 | 0.00 | 0.07 | 0.93 |

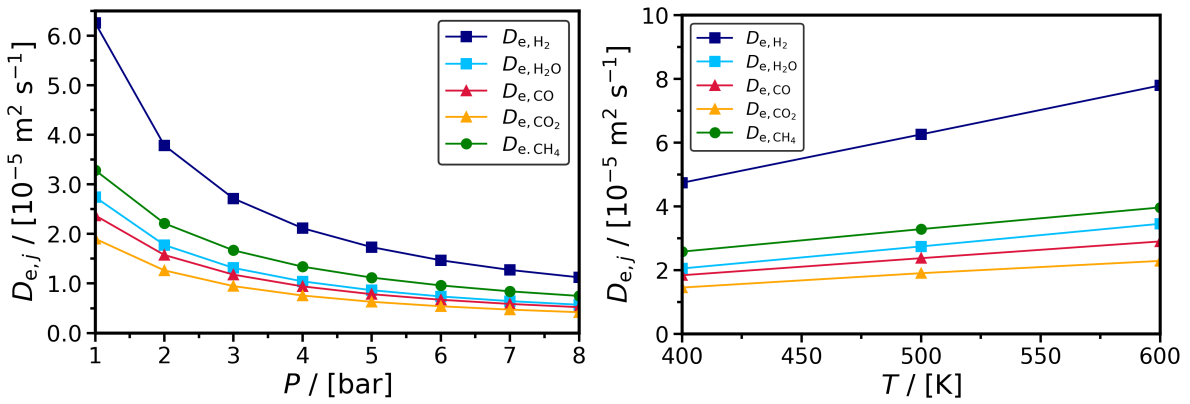


(a) (b)

**Figure 4.18: a)** Effective diffusivities as a function of pressure for the gases in the cooling gas stream of the MLP process. T = 1173 K. **b)** Effective diffusivities as a function of temperature for the gases in the reducing stream of the MLP process. P = 1.8 bar.

For the carburization reactions of the MLP process, the carbon activities for MC and BR are given in Figure 4.19a and Figure 4.19b, respectively. The temperature is increased from 500 K to 900 K. The pressure is also varied, from 2 bar to 8 bar. For MC, it can be observed in Figure 4.19a that an increase in temperature leads to an increase in the carbon activity. When T < 650 K however, the carbon activities become so small that carburization most likely does not occur. Only for a pressure of 2 bar the carbon activity seems adequate at 650 K. For the P = 2 bar case, the carbon activity becomes close to zero for T < 600 K. Thus, an increase in pressure has a negative effect on the carbon activity for MC and the MLP process. For BR in Figure 4.19b, the inverse relationship is observed. For BR, an increase in pressure leads to an increase in carbon activity. An increase in temperature also leads to an increase of the carbon activity, although it must be noted that the carbon activities do not exceed values of 0.45 from 500 K to 900 K. This implies that for a process operating on lower pressures, MC is the dominant carburization reaction. Whenever pressures are increased, the carbon activities of both MC and BR are more similar. Although it must be noted that MC still exhibits a higher carbon activity when T > 800 K for the high pressure case. In Figure 4.20a, for comparison the carbon activities for MC and BR are combined in a single graph for P = 2 bar.

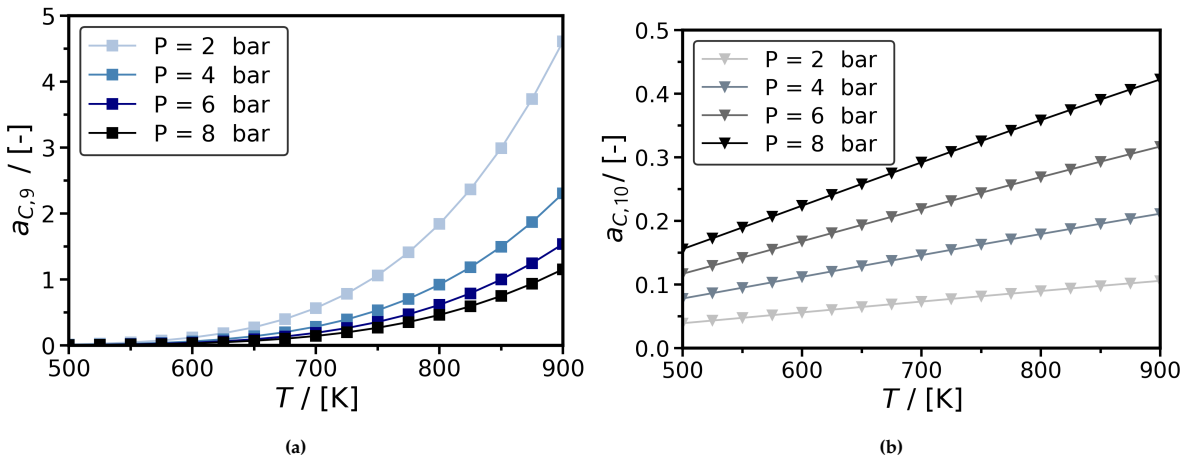


**Figure 4.19: a)** Carbon activities of MC as a function of temperature for the MLP process. **b)** Carbon activities of BR as a function of temperature for the MLP process.

Figure 4.20b gives the reaction rate of BR versus temperature for increasing values for pressure. It is seen that for all four cases, when T > 650 K the reaction rate for BR is as good as zero. When T < 650 K, the reaction rates become increasingly negative the lower the temperature. This implies that solid carbon is consumed by BR in the temperature range 500 K to 650 K. A higher pressure indicates a more negative reaction rate for BR.

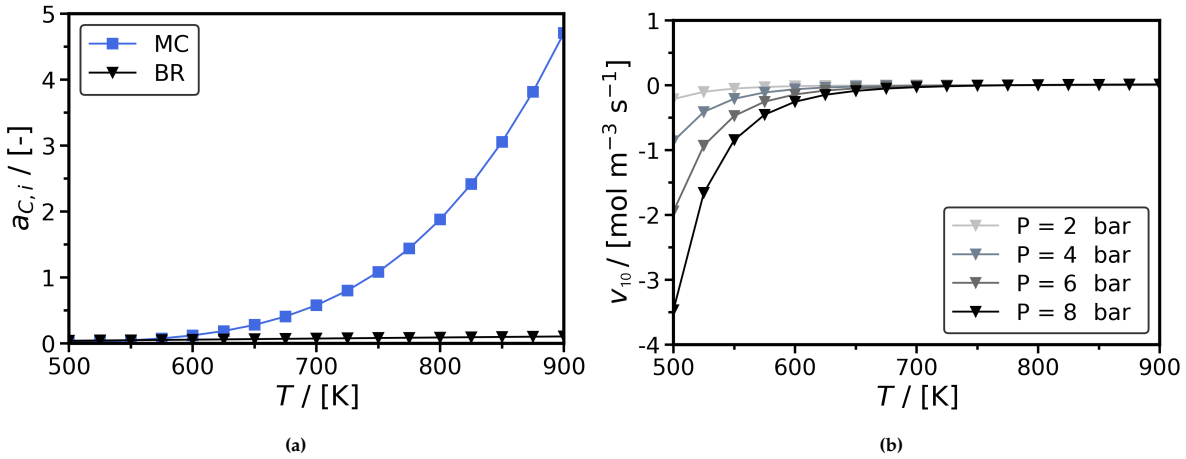


**Figure 4.20: a)** Carbon activities as a function of temperature of MC and BR for the MLP process. P = 1.8 bar. **b)** Reaction rates of BR for the MLP process.

Figure 4.21a presents the reaction rate for MC versus temperature for increasing pressures. It is apparent that for T < 600 K almost no MC occurs for P = 2 to P = 8 bar. When T > 600 K, the reaction rates gradually increase to a maximum rate at T = 825 K. Then, with a further increase in temperature all reaction rates become negative at T = 875 K. The cooling gas exit stream for MLP leaves the reactor at a temperature of approximately 750 K, so the negative reaction rates or the maximum value of MC are never achieved throughout the carburization process. An increase in pressure leads to an increase in reaction rate for MC. Subsequently, in Figure 4.21b the reaction rate of MC is also plotted versus the pellet porosities of Table 4.4. Here it is seen that an increase in pellet porosity leads to a decrease in MC reaction rate. This is probably due to the larger void fraction inside the metal framework, making it harder for the gases to interact with the solid.

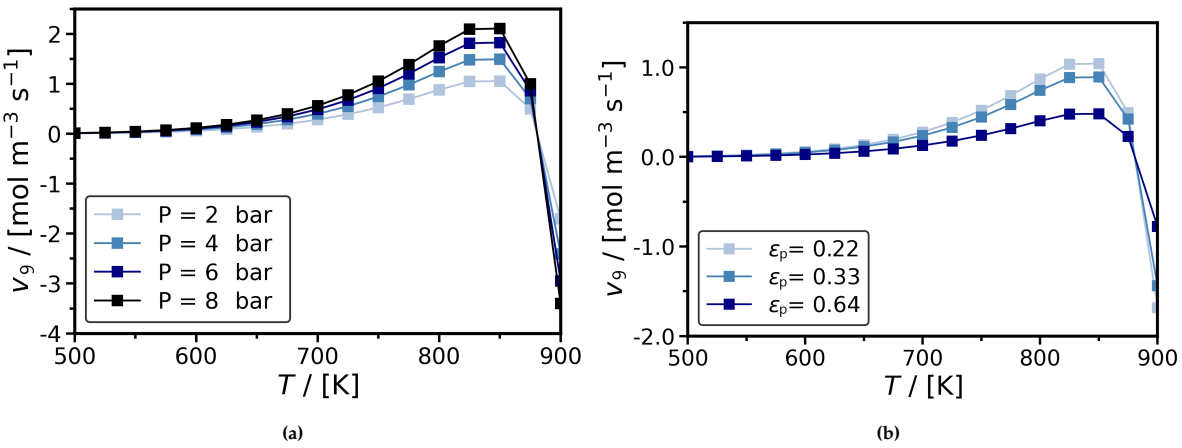


**Figure 4.21: a)** Reaction rates of MC as a function of temperature for the MLP process, with increasing pressure. **b)** Reaction rates of MC as a function of temperature for the MLP process, with increasing pellet porosity.

Finally, in Figure 4.22 the weight percentage of carbon is estimated as a function of temperature through the relationship of Chipman [28]. Here it can be observed that for temperatures up to 900 K the weight percentage attains values of approximately 1.2 wt.% of carbon. As can be seen in in Figure 4.22 however, the weight percentage of carbon increases exponentially even when T > 875 K, when the reaction rate for MC has become negative. Therefore, the application of this method is limited.

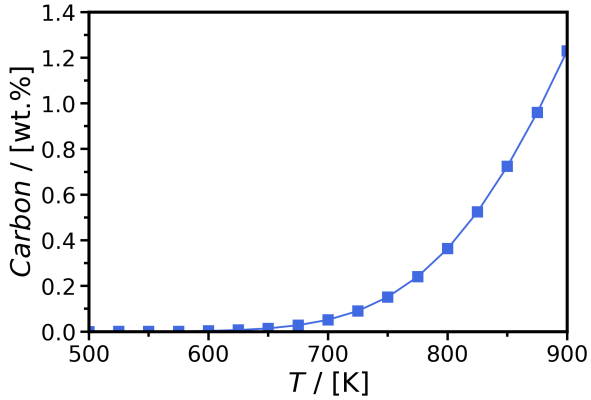


**Figure 4.22:** The weight percentage of carbon in iron, obtained via MC for the MLP process.

For the EMP process, the same kinetic modelling is performed. As can be seen in Table 4.4 however, no CO is present in the cooling gas stream of EMP. Therefore, no BR can take place and the values for the reaction rate become zero. This is shown in Figure 4.23a, where the carbon activities of MC and BR are given as function of temperature. In this graph, BR has a carbon activity of zero and therefore BR was omitted for the kinet reaction modelling of the EMP process. The carbon activity of MC increases with increasing temperature and already becomes greater than one at T = 550 K. Therefore, for the EMP cooling gas a higher carburizing potential through MC is observed than for the cooling gas of MLP shown in Figure 4.20a.

In Figure 4.23b, the carbon activity for MC is given as function of temperature for increasing operating pressures. It can be observed that for EMP, an increase in pressure leads to an increase in carbon activity. This is the opposite relationship as for MC for MLP, as given in Figure 4.19a. The mole fraction of $CH_4$ and the pressure seem to influence the carbon activity. For a large mole fraction of $CH_4$, a higher pressure increases the carbon activity. For a small mole fraction of $CH_4$, an increase in pressure leads to a decrease in carbon activity. This can explain the lower percentage of carbon in the DRI end product for MLP compared to EMP. The higher values of the carbon activ-

ity for MC for EMP also correspond with the higher weight percentage of carbon in the EMP end product.

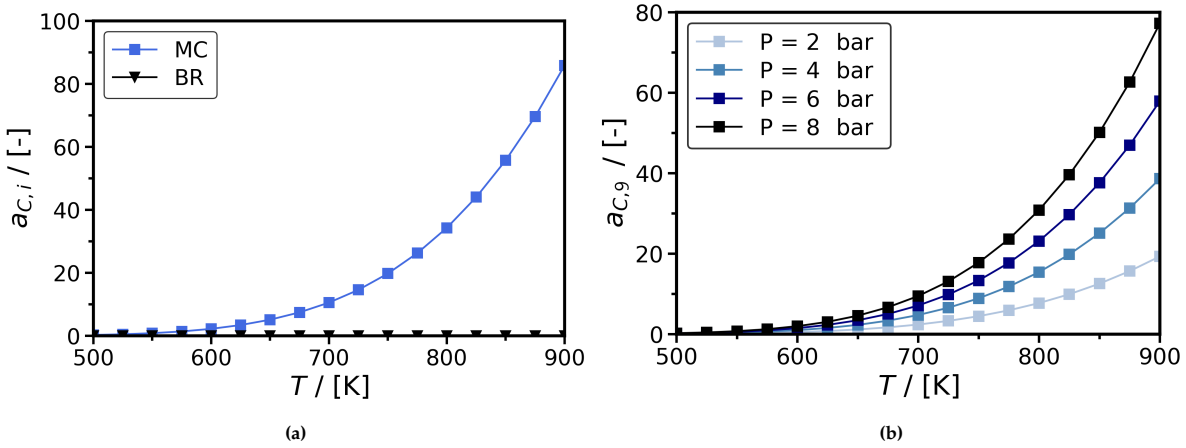


**Figure 4.23: a)** Carbon activities as a function of temperature of MC and BR for the EMP process. P = 7.2 bar. **b)** Carbon activities of MC as a function of temperature for the EMP process, with increasing pressure.

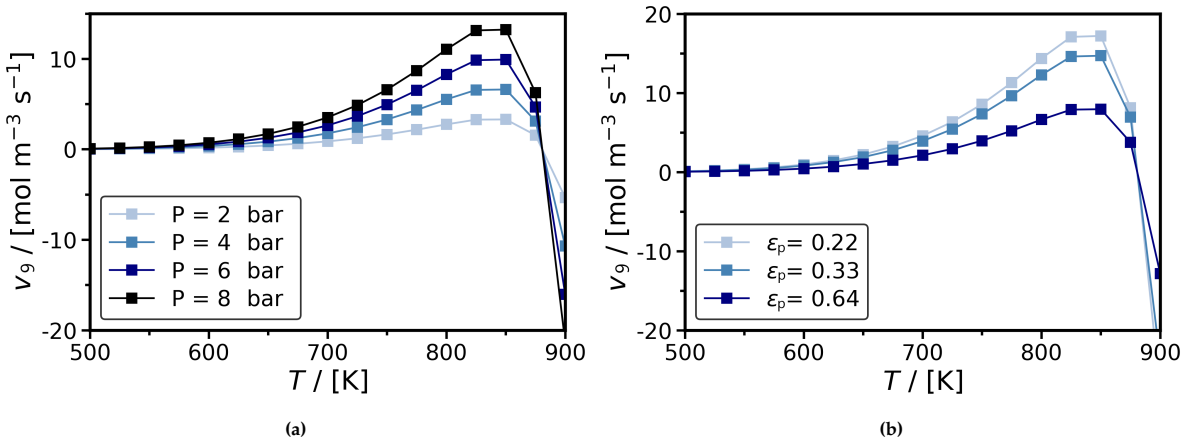


**Figure 4.24: a)** Reaction rates of MC as a function of temperature for the EMP process, with increasing pressure. **b)** Reaction rates of MC as a function of temperature for the EMP process, with increasing pellet porosity.

Figure 4.24a shows the reaction rate for MC as a function of temperature for increasing pressures in the EMP process. The same trend is observed as for the MLP coolin gas, only now higher reaction rates of MC are observed. An increase in pressure also leads to a higher increase in reaction rates for EMP. At T = 875 K, the reaction becomes negative, while a maximum reaction rate is observed for T = 850 K. The DRI end product of the EMP process of Appendix A.4 leaves the SF at T = 907 K. This implies that inside of the SF, the maximum reaction rates for MC could be attained. This is another explanation for the higher carburization rate for the EMP process compared to the MLP process.

In the end, Figure 4.25 shows the weight percentage of carbon versus temperature for EMP. Since temperatures inside of the cooling zone of EMP are still relatively high, a weight percentage of 2% to 3.5% can be justified via this graph. Here it must once again be noted that the model of Chipman [28] on which these results are based do not take into account the reversibility of the MC reaction. Therefore this relationship can not be applied for T > 850 K.

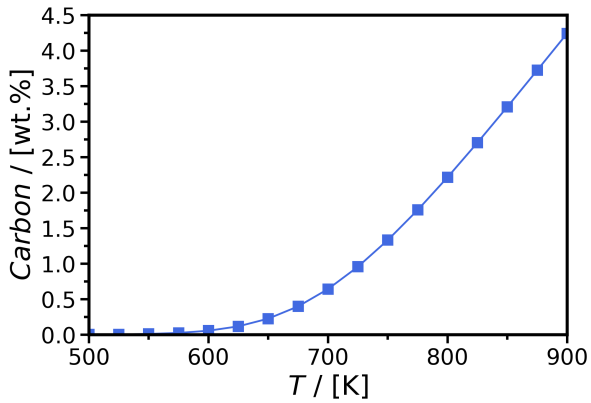


**Figure 4.25:** The weight percentage of carbon in iron, obtained via MC for the EMP process.

### 4.2.4. Comparison with Literature

From literature, it is known that the reduction rates of iron oxides with both $H_2$ and CO actually decrease when temperature is increased [53, 68, 87, 112]. For CO this boundary lays around 1123 K, while for $H_2$ the maximum reaction rate for reduction is usually achieved around 1173 K. After these temperatures, reduction reaction rates should decrease accordingly. As is apparent from Figure 4.14 and Figure 4.16, for reduction with $H_2$ and CO the reaction rates keep increasing well after these temperatures are reached. Therefore, the model of Rahimi and Niksiar [96] is flawed.

In the study of Rahimi and Niksiar [96], the results for the mole fractions of $H_2$ and CO obtained from the model for the simulation of an SF for the DRI process are compared to existing experimental data. For a simulation with a syngas mixture that has a $H_2$/CO-ratio of 1.41, which is just under the MLP $H_2$/CO-ratio of 1.55, an average error of 0.05% was obtained in comparison with the experimental data of Takenaka et al. [114]. When for the same $H_2$/CO-ratio the volumetric flow rate of the reducing gas was reduced, the error of the model increased to 0.7%. Upon a further volumetric flow rate reduction and a decrease of $H_2$/CO-ratio to 1.23, the error increased up to 2.7%. This indicates that for the MLP process, the model of Rahimi and Niksiar [96] can provide an accurate estimation of the reduction reactions of the DRI process. It appears that an increase in $H_2$ concentration and therefore an increase in $H_2$/CO-ratio leads to a decrease of the error of the model, although this has only been estimated for a $H_2$/CO-ratio of up to 1.41. Hence, no estimation can be made on the error of the model of Rahimi and Niksiar [96] for the EMP process, with a $H_2$/CO-ratio of 4.09.

In the kinetic reaction rate modelling of Hamadeh, Mirgaux, and Patisson [50] for MC, it can be observed in Figure 4.21a and Figure 4.24a that reaction rates become negative at T = 875 K. According to Nasiri, Panjepour, and Ahmadian [75] and Ribeiro et al. [99], MC produces solid carbon for carburization of temperatures up to 860 K. For T = 860 K, it is seen that the reaction rate for MC decreases rapidly. This is in accordance with literature Nasiri, Panjepour, and Ahmadian [75] and Ribeiro et al. [99].

The relationship of Chipman [28] seems to predict the weight percentages of carbon in the DRI end product quite accurately. It is reported that the MLP process can reach values of 1 to 2 wt.% of carbon, while EMP can reach percentages of up to 2 to 4 wt.% [50, 56]. These same values can be attained for processes up to 850 K in Figure 4.22 and Figure 4.25. However, as can be observed in Figure 4.21 and Figure 4.24, the reaction rate of MC will get negative for T > 850 K. This indicates that the carbon weight percentage should start to decrease at T = 850 K. This is not in line with the weight percentages of carbon that are observed in Figure 4.22 and Figure 4.25. Therefore, the relationship of Chipman [28] for MC is only valid up to 850 K.

## 4.3. Techno-Economic Scenario Modelling

Three scenarios were developed for the techno-economic assessment of the DRI process, labelled scenario A, B and C. Scenario A presents the situation in which the DRI process is run on 100% imported green $H_2$. This scenario is presented in Section 4.3.1. Scenario B describes the case where an on-site electrolyzer is included in the balance of plant for the DRI process, that is supplied with grey electricity from the Dutch electricity grid. Therefore, this scenario encompasses DRI production with grey $H_2$ and is presented in Section 4.3.2. Furthermore, compressed $H_2$ storage is included in this scenario as well. Scenario C specifies the situation in which the on-site electrolyzer is fed with electricity produced on a wind farm close-by. This scenario therefore is based on green $H_2$ and is shown in Section 4.3.3. Here again, compressed $H_2$ storage is considered. Finally, in Section 4.3.4 the results of the LCOP are compared to literature. It must be stated in advance that the results in this chapter are highly sensitive to the limitations and simplifications of the applied models. The data used for these calculations may vary between different sources and therefore a different outcome may be obtained when other literature is consulted. All data used throughout this chapter is listed in Appendix D.

### 4.3.1. Scenario A - Green $H_2$ Import for 100% $H_2$-based Direct Reduction of Iron Ore

In scenario A, the direct reduction process of iron ore is based on 100% green $H_2$. This green $H_2$ is not locally produced, but imported from countries and regions where large quantities of renewable electricity are harvested and green $H_2$ is produced. Countries or regions that show potential in this field are Canada, Australia and the Middle East [69, 49, 107]. A schematic overview of scenario A is presented in Figure 4.26.

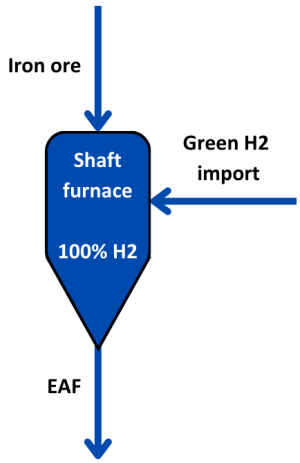


**Figure 4.26:** Techno-economic scenario A for the 100% $H_2$-based direct reduction of iron ore. This scenario assumes 100% green $H_2$ import for the reduction process. Of the direct reduction process, only the parameters for the shaft furnace are taken into account.

Since in this scenario the LCOP is highly sensitive to the price of green $H_2$, a parametric study on the $H_2$-price was conducted. The results are shown in Figure 4.27a. In this graph it can be seen that $H_2$-prices must fall below €2/kg for the $H_2$-DRI process to have a lower LCOP than the BF process. To become cheaper than the NG-DRI process, $H_2$-prices of less than €1/kg are required. At the moment, a 100 MW electrolyzer is being constructed in Europe that will sell its produced green $H_2$ for more than €8/kg [85]. When $H_2$-prices are that high, the $H_2$-DRI route is not feasible compared to the BF and NG-DRI processes.

The $H_2$-DRI scenario may become feasible when the European emission costs increase. When the CMC for the $H_2$-DRI process falls below the emission costs implemented by the EU, it is advantageous to switch to the $H_2$-DRI process. For the CMC a study on the $H_2$-price was conducted, of which the results are given in Figure 4.27b. The CMC is compared to the Carbon Emission Price of the European Union in 2023 and the predicted Emission Prices for 2030 and 2040 [129]. As current emission prices stand

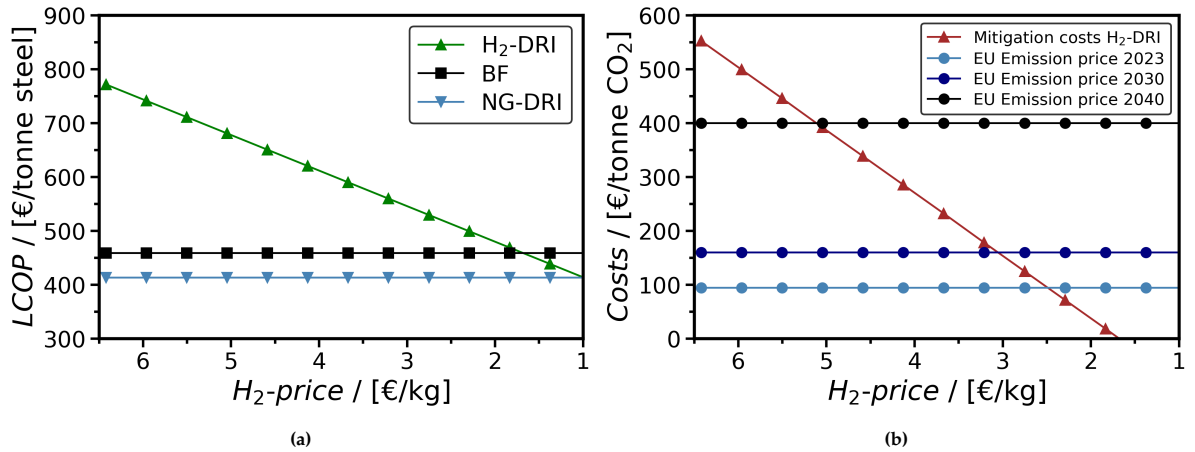


(a) (b)

**Figure 4.27: a)** The levelized cost of steel production (LCOP) of $H_2$ direct reduction of iron ore (DRI) with green $H_2$ import as a function of the $H_2$-price. The LCOP of the newly proposed $H_2$-DRI scenario is compared to the LCOP of the blast furnace (BF) and natural gas-based DRI processes. **b)** The carbon mitigation costs (CMC) of $H_2$-DRI with green $H_2$ import as a function of the $H_2$-price. The $H_2$-DRI process is compared to the BF process to produce the results for CMC. If $H_2$-prices are high and the carbon emission prices are low, the BF process is economically beneficial over $H_2$-DRI. When the line of the $H_2$-DRI CMC falls below the carbon emission price, $H_2$-DRI has become the cheapest option. Current and future emission prices in the European Union are shown in the graph for comparison.

at €94/tonne $CO_2$, the $H_2$-price does only need to fall below €2.50/kg for $H_2$-DRI to be economically favourable [65]. When emission prices increase to €160/tonne $CO_2$ by 2030, a $H_2$-price of €3/kg suffices. For 2040, the estimation of €400/tonne $CO_2$ is highly optimistic and not deemed to be realistic. A price of €400/tonne $CO_2$ is only regarded as a reasonable scenario if 90% of the EU reduction targets are met [129, 65]. If such carbon emission prices are ever to be attained, a $H_2$-price of €5/kg is sufficient for an economical feasible 100% $H_2$-DRI process. Although this looks promising at first sight, the required $H_2$-prices for this highly optimistic scenario are still far below current $H_2$ market prices.

### 4.3.2. Scenario B - Grey $H_2$ Production and Storage for 100% $H_2$-based Direct Reduction of Iron Ore

In scenario B, an on-site electrolyzer (ELY) is included in the balance of plant to produce $H_2$ for a completely $H_2$-based DRI process. Also, compressed $H_2$ storage with enough capacity for 4.5 hours is realized. A schematic overview of the complete scenario is shown in Figure 4.28. The ELY will be supplied with electricity from the Dutch grid, which has a relatively high emission factor. Over 2023, the Dutch grid emission factor (GEF) was 0.421 kg $CO_2$/kWh on average [83]. Therefore, this scenario is based on the production and storage of grey $H_2$. In Figure 4.29a and Figure 4.29b the LCOP as a function of the electricity price is given for different ELY options. The ELY scenarios are given in Table 4.6.

In 2023, electricity prices in the Netherlands were on average around €90 per $MWh_e$. Then it is evident from Figure 4.29a that electricity prices must fall drastically for the $H_2$-DRI process to be economically feasible in this proposed scenario. For ELY 1, the prices and efficiencies from state-of-the-art electrolyzers was taken. For ELY 2 and ELY 3, it is assumed that in the future ELY construction costs will decrease. It is clear though that a decrease of €367/$kW_e$ still requires an electricity price of €23/$MWh_e$ to become economically favourable over the BF process. In Figure 4.29b, more factors for ELY are taken into account. ALthough ELy 1 and ELY 4 are the same scenario, ELY 4 was included for consistency. ELY 5 and ELY 6 stand for an increase in electrical efficiency of the ELY, resulting in a lower electricity need for the production of $H_2$. It is evident that for the most optimistic scenario, an electricity price of €33/$MWh_e$ is the required minimum for an economically feasible case. Since average electricity prices in the Netherlands were up to €90/$MWh_e$ over the year 2023, it will probably take a long time to attain such low prices and for scenario B to become feasible. Furthermore, the question arises whether a scenario with electricity import from the Dutch electricity grid should be considered at all, since the DRI process will then rely on grey and not on green $H_2$. This indicates that the process is not $CO_2$ free.

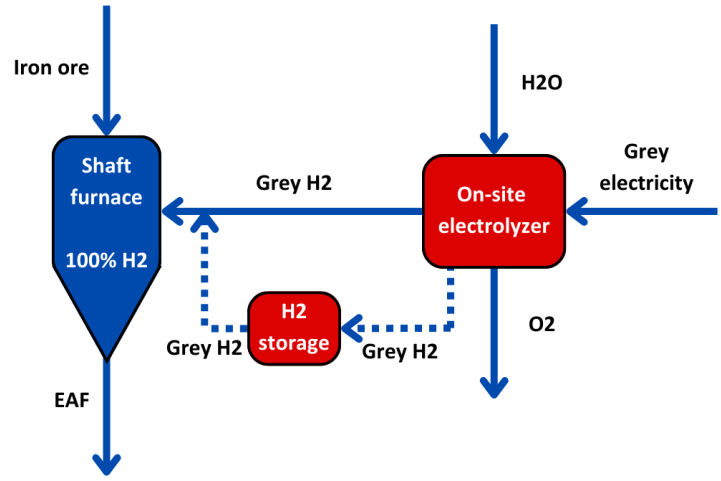


**Figure 4.28:** Techno-economic scenario B for the 100% $H_2$-based direct reduction of iron ore. This scenario assumes 100% grey $H_2$ production at an on-site electrolyzer that is supplied with grey grid electricity. In addition, there is compressed $H_2$ storage with a capacity of 34000 kg. This is sufficient for 4.5 hours of shaft furnace operation with an annual output of 1 Mt of direct reduced iron.

**Table 4.6:** Different electrolyzer (ELY) scenarios for levelized cost of steel production calculations. The parameters given are the construction costs of the installed capacity of the ELY in [€/$kW_e$], the electrical efficiency of $H_2$ production in [$kWh_e$/kg $H_2$] and the indirect emissions of the electrical arc furnace further down in the process in [t $CO_2$/t steel].

| **Scenario** | *Price* / [€/$kW_e$] | *Efficiency* / [$kWh_e$/kg $H_2$] | *Indirect EAF emissions* / [t $CO_2$/t steel] |
|---|---|---|---|
| *ELY 1* | 642 | 53 | 1427 |
| *ELY 2* | 459 | 53 | 1427 |
| *ELY 3* | 275 | 53 | 1427 |
| *ELY 4* | 642 | 53 | 1427 |
| *ELY 5* | 459 | 45 | 1142 |
| *ELY 6* | 275 | 40 | 856 |

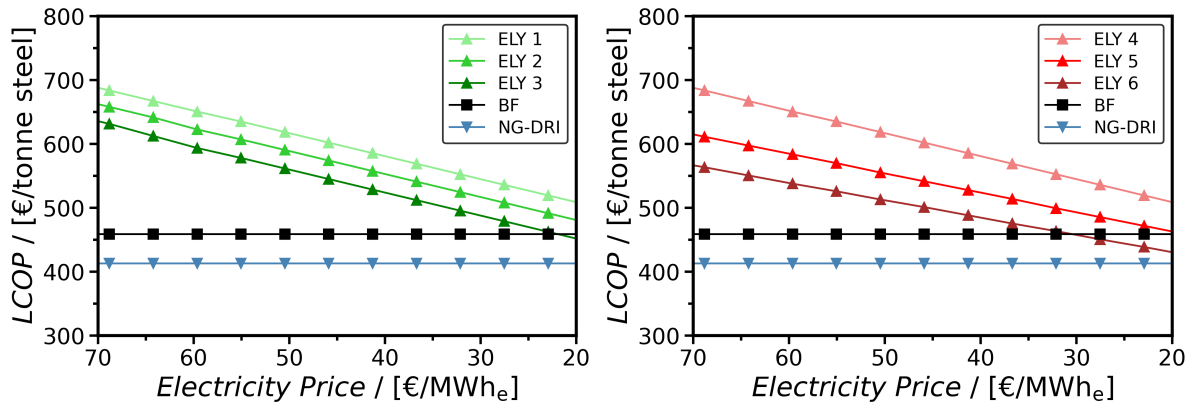


(a) (b)

**Figure 4.29: a)** The levelized cost of steel production (LCOP) of $H_2$ direct reduction of iron ore (DRI) scenario B as a function of the electricity price. The LCOP of the newly proposed $H_2$-DRI scenario B is compared for different electrolyzer (ELY) configurations to the LCOP of the blast furnace (BF) and natural gas-based DRI processes. The ELY becomes cheaper to construct for subsequent scenarios. **b)** The LCOP of $H_2$-DRI scenario B as a function of the electricity price. The LCOP of the newly proposed $H_2$-DRI scenario B is compared for different ELY configurations to the LCOP of the BF and natural gas-based DRI processes. The ELY becomes cheaper to construct and electrically more efficient for subsequent scenarios.

Aside from the electricity price, the GEF also plays an important role in the feasibility of scenario B. At the moment, the Dutch grid is relatively carbon intensive totalling an average of 0.421 kg $CO_2$/kWh in the year 2023. For comparison, the GEFs of other European countries are presented in Table 4.7.

Even in Germany, where a lot of coal is used for electricity generation, the GEF is lower than in the Netherlands. With grid-related carbon emissions it is not possible to produce green $H_2$ with grid electricity. Therefore, scenario B assumes the production and consumption of grey $H_2$. In Figure 4.33, the total emissions of the different processes is plotted as a function of the GEF. It is shown that for a GEF of 0.10 $kgCO_2/kWh$, grey $H_2$-DRI becomes less carbon intensive than BF. Hence, in Sweden and Norway scenario B is a feasible scenario, while Belgium is quite close to the break-even point. In the most optimistic scenario, the GEF does only need to fall under 0.20 $kgCO_2/kWh$ for a less carbon intensive process than BF steel production. In that case, scenario B will be feasible in Denmark as well. Although it will take some time for the Dutch electricity grid to decarbonize sufficiently, there are immediate possibilities for scenario B in countries like Belgium, Denmark, Sweden and Norway.

Another challenge that arises for scenario B is the problem of net congestion in the Netherlands. The feed-in of renewable sources into the net is increasing rapidly, bringing about major challenges for the Dutch electricity grid in the years to come [41]. The waiting list for a grid connection is increasing rapidly as well [14]. Therefore, the concept of a 400 MW ELY that is supplied with grid electricity does not seem to be a realistic scenario in the Netherlands at the moment.

**Table 4.7:** Average grid emission factor in the Netherlands, its bordering countries and some Scandinavian nations over the year 2023 [83].

| **Country** | *Grid Emission Factor* / [$kgCO_2/kWh_e$] |
|---|---|
| *The Netherlands* | 0.421 |
| *Belgium* | 0.107 |
| *Germany* | 0.354 |
| *Denmark* | 0.185 |
| *Sweden* | 0.019 |
| *Norway* | 0.018 |

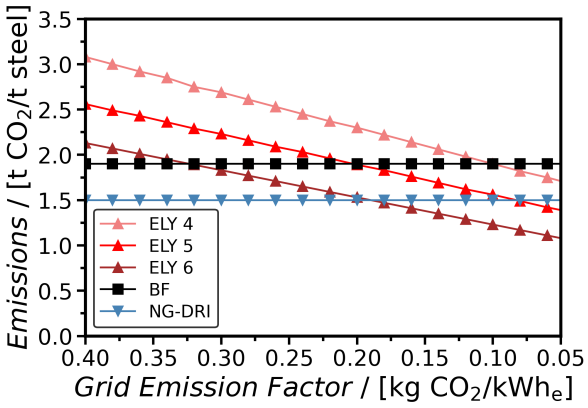


**Figure 4.30:** Total $CO_2$ emissions per tonne steel produced of the newly proposed $H_2$ direct reduction of iron ore scenario B as a function of the grid emission factor. For comparison, the $CO_2$ emissions for the blast furnace (BF) and natural gas-based DRI processes are given as well. For subsequent ELY scenarios, the indirect $CO_2$ emissions of the electric arc furnace further down in the steel production process decrease.

### 4.3.3. Scenario C - Green $H_2$ Production and Storage with Wind Farm for 100% $H_2$-based Direct Reduction of Iron Ore

In this scenario not only an on-site ELY and compressed $H_2$ storage are included in the balance of plant, but a whole wind farm is constructed just off the coast of IJmuiden, where TATA Steel is located. Scenario C is depicted schematically in Figure 4.31. The wind farm site considered for this scenario is called *IJmuiden Ver* and is currently under tender. The site lies 54 km off the coast and has enough area to support a wind farm that can supply an ELY of 400 MW, as required for the production for 1 Mt steel per year. The location of the *IJmuiden Ver* site is presented in Figure 4.32. In addition, more data and information of the wind farm site is presented in Table 4.8.

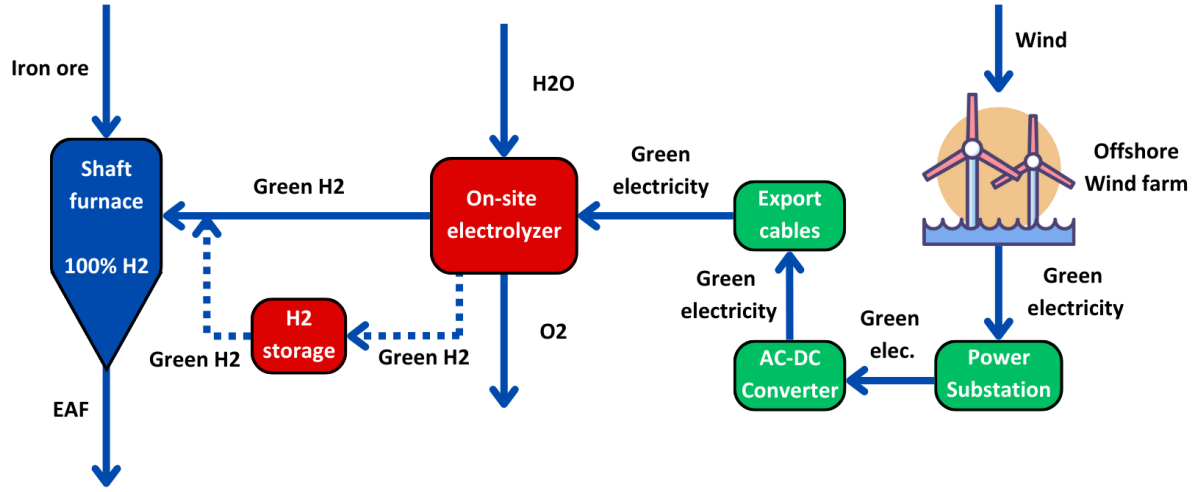


**Figure 4.31:** Techno-economic scenario C for the 100% $H_2$-based direct reduction of iron ore. This scenario assumes 100% green $H_2$ production at an on-site electrolyzer that is supplied with renewable electricity from a wind farm. This wind farm will be constructed in the vicinity of TATA Steel IJmuiden. In addition, there is compressed $H_2$ storage with a capacity of 34000 kg. This is sufficient for 4.5 hours of shaft furnace operation with an annual output of 1 Mt of direct reduced iron.

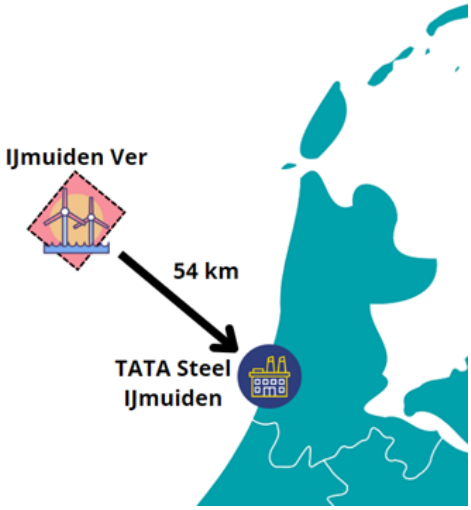


**Figure 4.32:** The location of the wind farm site *IJmuiden Ver* and its distance to the TATA Steel plant in IJmuiden.

**Table 4.8:** Information of the offshore wind farm site *IJmuiden Ver*.

| Parameter | Value | Unit |
|---|---|---|
| *Area* | 650 | [$km^2$] |
| *Distance to shore* | 54 | [km] |
| *Energy density wind farm* | 6 | [$MW_e/km^2$] |

For this scenario, it was estimated that in the least optimistic scenario the eventual costs for electricity of the wind farm amount to €40/MWh. Realistically speaking, values for state-of-the-art wind farms usually get up to €60/MWh [123]. The results for scenario C are depicted in Figure 4.33. In this optimistic scenario, an LCOP of more than €500/tonne steel is still attained considering current wind farm and electrolyzer prices and efficiencies. If the technology becomes less expensive and more efficient, it is predicted that around the year 2030 the $H_2$-DRI scenario becomes economically more attractive than BF. By 2050, through this estimation $H_2$-DRI becomes the most feasible economic option. Since this scenario essentially has no direct $CO_2$ emissions, it may be considered as the most promising option. In scenario C, any $CO_2$ emitted during the construction of the wind farm, the electrolyzer or $H_2$ storage are not taken into account. When comparing the LCOP of scenario C with the LCOP of scenario A and B, scenario C offers the most promising 100% $H_2$-DRI case.

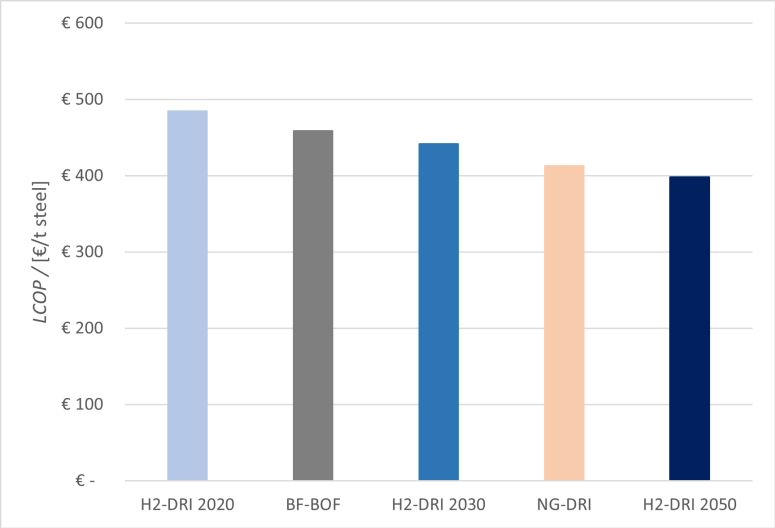


**Figure 4.33:** Levelized cost of steel production (LCOP) for $H_2$-based direct reduction (DRI) scenario C. For the newly proposed scenario C, the LCOP is given for 2020, 2030 and 2050. For comparison, the LCOP of the blast furnace and natural gas-based DRI processes are given as well.

### 4.3.4. Comparison with Literature

Although a techno-economic assessment of the LCOP in the Netherlands is novel, research has been conducted on sustainable steel manufacturing in Norway. As reported by Bhaskar et al. [15], a plant set-up with an on-site electrolyzer supplied with electricity from the Norwegian electricity grid got initial LCOP values varying from €571 to €662/tonne steel produced. In scenario B for TATA Steel IJmuiden, the initial LCOP is much higher, at approximately €690/tonne steel produced. It is to no surprise that the LCOP in Norway lies closer to the BF and NG-DRI processes, since electricity prices in Norway are lower than in the Netherlands. For the LCOP of Bhaskar et al. [15], the most promising scenario assumed a grid electricity price of €37/$MWh_e$. It was also reported that a grid emission factor of 0.18 $kgCO_2/kWh_e$ leads to less carbon pollution than compared to BF steel production [15]. This is in line with the findings of Section 4.3.2. For scenario A no insightful comparison material was found, while for scenario C an electricity price of €60/$MWh_e$ was deemed more realistically for an offshore wind farm [20].

# 5 Conclusions

Based on the results and discussion of Chapter 4, this chapter aims to interpret the results and draw conclusions in the light of the research question and sub-questions proposed in Chapter 1. Section 5.1 discusses the results for the reduction of the iron ore pellets, while Section 5.2 provides the conclusions for the bulk gas phase. Then, Section 5.3 gives the conclusions for the carburization reactions. Finally, the conclusions for the techno-economic analysis are given in Section 5.4.

## 5.1. Iron Ore Reduction

When interpreting the results of Section 4.1.1, the most important conclusion is that reduction of wustite with $H_2$ is endothermic, while reduction of wustite with CO is highly exothermic. Although the reduction of hematite with $H_2$ is exothermic as well, the overall reduction of $Fe_2O_3$ to metallic Fe is endothermic. For reduction with CO, hematite reduction is exothermic. This means that for iron oxide reduction with CO, less energy is required to keep the reactions going while for the $H_2$ process, extra energy is needed for stable operating conditions inside of the shaft furnace.

In Section 4.2.2, the reduction reactions of hematite and wustite with $H_2$ and CO were modelled for the MLP ad EMP processes. When comparing the reaction rates for $H_2$ reduction, it can be noted that both hematite and wustite reduction with $H_2$ increase with an increase in pressure and $H_2$/CO-ratio. Since the driving force of the kinetic modelling of the reduction reaction is a concentration difference, this increase in reaction rate is mostly influenced by the $H_2$/CO-ratio.

For the MLP process, for the total temperature range of 1000 - 1300 K, reduction with $H_2$ remains dominant over reduction with CO. For the optimal reduction temperature of 1173 K, wustite reduction with $H_2$ is slightly faster than hematite reduction. Therefore, hematite reduction is the rate-determining step. For CO, the rates of both reduction reactions are close to equal. With an increase in temperature, it is observed that the reduction rate of hematite becomes larger than that of wustite, which hence is the rate-determining step for iron oxide reduction with temperatures higher than 1200 K.

For the EMP process, a large difference is observed between $H_2$ and CO reduction. When reducing with $H_2$, the reduction of hematite remains the rate-determining step until approximately 1250 K. For reduction with CO however, wustite reduction is rate-determining for the complete temperature range of 1000 K to 1300 K. For an increase in temperature, the reduction rate of hematite increases faster than reduction of wustite, just as in the MLP process. When comparing reduction rates of $H_2$ versus CO, $H_2$ is by far the dominant reducing agent. At 1173 K, reduction of hematite with $H_2$ is 3 times higher than reduction of hematite with CO. Reduction of wustite at the same temperature is at least 9 times faster than reduction with CO.

In conclusion, the results for the reduction of hematite and wustite can be summarised as follows:

- Overall reduction with $H_2$ is endothermic, overall reduction with CO is highly exothermic
- For the low and high $H_2$ processes, reduction with $H_2$ is dominant over reduction with CO since $H_2/CO > 1$
- For the MLP process, hematite reduction is rate-determining at 1173 K
- For the EMP process, wustite reduction is rate-determining at 1173 K

## 5.2. Bulk Gas Flow

In Section 4.1.2, the reducing gas streams for the MLP and EMP processes are compared and minimized. It is seen that in the range of 1 bar to 8 bar, for both processes no significant influence of the pressure on the equilibrium composition is observed. For temperatures, it is evident that an increase in temperature is beneficial for $H_2$ and CO concentrations in the gas phase. At the optimal reduction temperature of 1173 K however, no large differences in the chemical equilibrium composition are seen when increasing or decreasing the temperature. The temperature must be significantly lower for alterations to the chemical equilibrium (T < 900 K). Therefore, it can be concluded that both temperature and pressure have little influence on the chemical equilibrium composition of the reducing gases in the bulk flow.

In Section 4.1.3 the influence of the $H_2/CO$-ratio is modelled. It is seen that for T > 1000 K, no big differences in mole fraction in the gas phase is observed for all given ratios. For the pressure, no difference in equilibrium composition is noted for the complete range of 1 bar to 8 bar. When the $H_2/CO$-ratio increases, $y_{H2}$ increases. After $H_2/CO > 5$ however, the difference between ratios becomes small. This is in line with literature, observing that after a $H_2$ volume fraction > 70%, no higher reduction rates are observed.

For the gas phase reactions, SRM and WGS were modelled of which the results are shown in Section 4.2.1. When looking at the results for the MLP process, at T < 1075 K the WGS is dominant. SRM is then actually negative, meaning that $H_2$ and CO are consumed to produce $CH_4$ and $H_2O$. Although $CH_4$ is known to exhibit some reducing behaviour, this still has a negative effect on the overall reduction process. For MLP at the optimal reduction temperature of 1173 K, SRM is positive and WGS close to zero. For the EMP process at T = 1173 K, WGS is negative while SRM is just above zero. Therefore, the most important reaction in the gas phase for both the MLP and EMP process is SRM. When varying the temperatures from 1123 K to 1173 K and 1223 K, it can be seen that both SRM and WGS are strongly effected by pressure. Nevertheless, in this temperature range SRM remains dominant and WGS almost negligible. This complies with the results of the Gibbs minimization in Section 4.1.1, where it can be seen that at temperatures between 1123 K and 1223 K the equilibrium gas phase composition mainly consists of $H_2$ and CO and almost no $CH_4$ and $H_2O$. This is true for both the low $H_2$ and high $H_2$ process.

In Section 4.2.1, it is seen that both SRM and WGS are highly influenced by the initial gas phase composition. For the MLP process, for T = 1173 K SRM is positive for an increasing pressure up to 6 bar, after which the reaction rate becomes negative. A decrease in temperature to 1123 K has a large influence on the reaction rate of SRM, which becomes increasingly more negative after P > 4 bar. Increasing the temperature to T = 1223 K has a positive effect on SRM, which remains positive in the whole pressure range of 1 bar to 8 bar. For the WGS, an increase in temperature shows the opposite effect. At T = 1223 K, the WGS on Fe becomes slightly negative for the whole pressure range of 1 bar to 8 bar. At T = 1173 K and T = 1123 K, WGS on Fe becomes exponentially more positive. It is seen that temperature only has a small effect on the WGS, whereas the pressure has a large influence on the reaction rate. For SRM, it is necessary to have T > 1050 K for the reaction rate to be positive, while a pressure in the region of 3 bar to 5 bar gives the highest reaction rate for T = 1173 K. In the end, it can be concluded that MLP is well suited for internal reforming of natural gas.

For EMP, it can be seen in Figure 4.10 that the reaction rates of SRM and WGS are indeed influenced by a higher $H_2$ volume percentage. It can be noted that SRM shifts to the right compared to the MLP process, while WGS shifts downwards. Hence, the equilibrium of WGS has shifted to the left, while a higher

temperature is required to have $H_2$ and CO formation from the available $CH_4$. It is seen that T > 1150 K is necessary for a positive reaction rate for SRM. Lower temperatures are quickly becoming unfavorable due to $CH_4$ formation out of $H_2$ and CO, which slows down the direct reduction process. In the high $H_2$ process, it is seen that WGS actually is negative for all temperatures and the whole 1 bar to 8 bar pressure range. SRM becomes more positive and hence SRM happens faster, but this mainly applies to the T = 1173 K and T = 1223 K cases. It follows that for the MLP process, internal reforming of $CH_4$ can be a viable option for DRI production, especially in the early stages of the operation when green $H_2$ prices are still high. For EMP, a higher temperature is needed for successful internal reforming, which can have a negative impact on reduction rates. Therefore, it can be concluded that EMP is not suited for internal reforming of natural gas.

In conclusion, the results for the reactions in the bulk gas flow are:

- The influence of temperature and pressure on the chemical equilibrium composition is negligible
- If the ratio of $H_2$/CO in the reducing gas becomes larger than 7, no remarkable changes to the equilibrium composition are observed
- The dominant reaction for the bulk gas flow for T = 1173 K is SRM, for both the MLP and EMP $H_2$ process
- When high amounts of $H_2$ are present in the reducing gas, both pressure and temperature are influential on the reaction rate for SRM
- Internal reforming of $CH_4$ shows the most potential for the MLP process

## 5.3. Carburization Reactions

For MLP, it is evident that an increase in temperature has a positive effect on the carbon activity for both MC and BR. For MC the increase is exponential, while for BR the increase is more or less linear. An increase in pressure lowers the carbon activity for MC. For BR, an increase in pressure increases the carbon activity. In the case for P = 8 bar and T = 900 K, $a_{C,8}$ is still lower than 0.45. In Figure 4.20a the carbon activities of MC and BR are combined and it is seen that when T > 600 K, the carbon activity for MC increases rapidly, while BR remains low. Therefore, the main carburizing mechanism in this temperature and pressure range is MC.

In Figure 4.20b and Figure 4.21a the reaction rates for MC and BR are presented versus temperature for different pressures for the MLP process. BR is negative for T < 700 K, and close to zero for T > 700 K. This is in line with the carbon activity given in Figure 4.20a. MC on the other hand increases rapidly in reaction rate in between 600 K to 875 K. When T > 875 K, the reaction rate gets negative, so carbon gets consumed instead of produced. When the pressure is increased, the reaction rate increases. Figure 4.20b show the reaction rate for MC for different porosities of the solid. An increase in porosity exhibits a decrease in reaction rate. Probably due to the larger void fraction in the solid, the reactive area for the carburization reactions decreases. Finally, Figure 4.22 presents the weight percentage of carbon as a function of temperature. This value increases exponentially with temperature. It is evident that this model does not take into account the reversibility of the carburization reactions, since the weight percentage of carbon keeps on increasing well after T > 875 K.

For the EMP process, the carbon activities for MC and BR are given in Figure 4.23a. It is seen that, due to the larger amount of $CH_4$ in the cooling gas of the high $H_2$ process, it follows that MC is the dominant carburization reaction. The same trend is observed in Figure 4.23b and Figure 4.24a. The carbon activity and reaction rate for MC are a factor 5 to 6 times higher than for the MLP case. Due to the absence of CO in the cooling gas, BR was assumed to be zero and MC is the main carburizing reaction. For an increase in porosity, the same trend of a decreasing reaction rate for MC is observed. The weight percentage of carbon in between two and four percent is more easily reached as in Figure 4.25 compared to Figure 4.22. This is in line with literature [56].

In conclusion, the results for the carburization reactions are:

- For both the MLP and EMP process, Methane Cracking is the dominant carburization reaction
- An increase in pressure is beneficial to carbon deposition on Fe
- When the pressure is increased, a higher temperature is needed for the same carburization levels
- An increase in porosity leads to a decrease in carburization potential
- $CH_4$ has a higher carburizing potential than CO

## 5.4. Techno-Economic Scenarios

For each of the proposed techno-economic scenarios, different conclusions may be drawn. For scenario A, in which green $H_2$ is imported, the $H_2$ price needs to fall below €1.80/kg $H_2$ before the scenario becomes economically more attractive than the BF process. Before a better case than NG-DRI is obtained, the $H_2$-price even needs to fall as low as €1.10/kg$H_2$. It must be noted that a $H_2$ price of €3.60/kg$H_2$ is required to reach break-even for the carbon mitigation costs. These $H_2$-prices are extremely low compared to current $H_2$-market prices. Therefore, scenario A is not deemed realistic, for now and in the near future.

For scenario B, the electricity price needs to fall below €20/MWh$_e$ to be economically feasible. For the most optimistic electrolyzer scenario, prices of €30/MWh$_e$ are sufficient. Even if EU carbon emission prices increase up to €160/tonne $CO_2$, scenario B will only become attractive if $H_2$-price fall to €3/kg. This will not happen in the next five years. Furthermore, scenario B only becomes less carbon intensive than BF and NG-DRI if the GEF falls below 0.20 to 0.10 kg$CO_2$/kWh. Therefore, scenario B may prove to be feasible in countries with a lower GEF than the Netherlands. Countries where scenario B may prove to be feasible are Belgium, Sweden and Norway.

Of all proposed scenarios, scenario C provides the most promising $H_2$-DRI case. Although the initial LCOP is still higher than the LCOP of BF and NG-DRI, the process emits no direct $CO_2$ and has initially the lowest LCOP of all three proposed techno-economic scenarios. The electricity price of €40/MWh for the constructed wind farm is still on the optimistic side though. The following conclusions can be drawn form the techno-economic assessment:

- At the moment, the import of green $H_2$ for 100% $H_2$-DRI is not regarded as a feasible option
- EU emission prices must increase up to €160/tonne $CO_2$ and a $H_2$-price must decrease to €3/kg before an on-site electrolyzer supplied with grid electricity will become feasible
- In the most optimistic electrolyzer scenario, electricity prices need to fall below €30/MWh for a competitive LCOP for the grid-supplied electrolyzer scenario
- GEF should fall below 0.20 to 0.10 kg$CO_2$/kWh$_e$ for a decrease in carbon emissions for $H_2$-DRI with an on-site grid-supplied electrolyzer compared to NG-DRI
- In Belgium, Sweden and Norway, a grid-supplied on-site electrolyzer may already be less carbon intensive than NG-DRI
- If a wind farm is constructed that produces renewable electricity for €40/MWh, an economically feasible $H_2$-based DRI process could be realized

# 6

# Recommendations

In addition to the conclusions of Chapter 5, it is possible to make recommendations on the DRI process and on future research into the topic. Where the focus of $H_2$-based steelmaking mainly lies on reducing the direct $CO_2$ emissions of the DRI process, the recommendations presented in this chapter lay the emphasis on bringing down the indirect emissions of steel manufacturing as well. Whereas the direct emissions of the natural gas-based DRI process amount to 0.45 tonne $CO_2$/tonne DRI produced, the indirect emissions amount to 1.1 tonne $CO_2$/tonne DRI produced [98]. Therefore, bringing down indirect emissions is a must if carbon neutrality is ever to be achieved for DRI steel manufacturing. In Section 6.1 the recommendations on the DRI process are given, while in Section 6.2 the recommendations for the carburization process are explicated. At last, in Section 6.3 suggestions are made for future studies on the DRI topic.

## 6.1. Direct Reduction Optimization

In this section recommendations will be made that aim to bring down the indirect emissions for the DRI process in the Netherlands. These recommendations regard increasing the efficiency of the DRI process and decreasing the carbon emissions of upstream and downstream processing steps.

- **Dual-row Exit Gas Recycling**

The gaseous waste stream at the top of the SF (*stream 7*) and the waste cooling gas stream (*stream 9*) still contain relatively high amounts of $H_2$, CO, $H_2O$ and $CH_4$. A recycle of the $H_2$ and CO from *stream 9* back to the reducing gas stream would increase the process efficiency and would reduce the amount of resources needed. Furthermore, the $CH_4$ in *stream 9* can be reutilized for the cooling gas stream, while the $H_2O$ in *stream 7* could be used for the production of $H_2$. Top gas or cooling gas recycling is not a novel concept and it is already applied to the state-of-the-art MIDREX and Energiron processes [56, 66]. Most applied top gas recycling systems are single-row however. It is reported in literature that a dual-row gas injection of a recycle stream yields a higher gas utilization and lowers the total energy consumption of the process [106].

- **Pressurized Chemical Looping**

A novel idea on decarbonizing natural gas-based DRI, is that of pressurized chemical looping (PCL) [19, 52]. In this concept, the reformer and the gas heaters in the SF are replaced by PCL combustion units. PCL is a manner of heat production through the use of fossil fuels that includes a $CO_2$ capture and utilization unit. Furthermore, due to the high pressures of PCL, equipment size and costs are reduced and reaction rates for SRM increase. Waste heat from PCL can be harvested via process water and can be utilized elsewhere in the production process. It must be noted that PCL is in principle not a carbon neutral process and that it is mainly an improvement on the natural gas based DRI process.

- **Reutilization of Process Waste Heat**

The gases that exit the SF for natural gas and $H_2$-based DRI production have temperatures of around 600 K to 700 K. This heat is initially lost as the gases are cooled again for seperation and reusage. It is however a feasible scenario to reutilize the waste heat from these gaseous exit streams via process water for example, that can be redirected for the pre-treatment of gases in a reformer. This will reduce the pre-heating requirements of the process, leading to a less carbon intensive process.

- **Control of Pollution**

Indirect $CO_2$ emissions comprise roughly 70% of the total for natural gas-based steel production [98]. In these indirect emissions, the harvesting and pelletizing process of the iron ore burden is considered. Multiple suggestions were made in literature to decrease the environmental impact of iron ore production. Recommendations are for example the implementation of a 30 meter high wind screen around the bulk resource and a dust-collector where pellet transportation takes place [30]. For the harvesting of the iron ore the electrification of the process is suggested, although it must be noted that the electricity must be 100% green before it can have a serious impact on carbon emissions. To gain a better insight in the decarbonization opportunities of the iron ore pellet production, it is advised to conduct a life cycle assessment.

## 6.2. Renewable Carburization Sources

The challenge of reducing emissions in the carburization process lies in finding a sustainable carbon source that brings the total carburization process to net zero. The term 'sustainable carbon source' implies an organic source for carbon, that is easily replenished by nature. The idea is that the source can be considered as carbon neutral when the emissions of the use of the carbon source cancel out against the $CO_2$ uptake over the lifetime of the organic material. It must be noted that is not facile to exactly determine all $CO_2$ emissions and $CO_2$ uptake of the organic material and that different sources in literature present different outcomes for these kind of estimations. In this section two types of sustainable, organic carbon sources for the carburization process are proposed and discussed briefly. The two types of organic carbon sources that were selected required the lowest carburizing temperatures according to Adedipe et al. [2]. This temperature lies close to 800°C.

- **Cassava leaves**

As reported by Arthur and Azeko [7], the wastes that cassave produce like leaves and peels are usually rich in cyanide. Usually, these residual products are used for the production of starch and ethanol, while there is also an opportunity to use these wastes as a bio-cyaniding processing source. It has been reported in literature that *in situ* heating of these cassave waste products leads to diffusion of both carbon and nitrogen into iron and steel products [4, 8]. Temperatures of 1073 K were reported to be sufficient for carburization to take place, which is significantly higher than cooling gas data in Appendix A.

- **Date seeds & Snail shells**

From Adedipe et al. [2], the proposed organic carburizing material by Kolawole, Awoyemi, and Abiona [58] consists of a mixture of date seeds and snail shells. Dates are being grown in Asia and northern Nigeria. Its seeds are regarded as a waste product and are usually discarded [58]. When combined with snail shells in a 60% date seed / 40% snail shell ratio, it has been observed that mild steel products could be carburized successfully. Since dates are a popular fruit, its initially worthless seeds could provide an interesting organic carbon source for DRI production. Until now however, only small experiments have been carried out on the matter and therefore research with this organic carbon source on a larger scale is suggested.

## 6.3. Further Research

Although this thesis research presents some valuable insights on the important chemical reactions for the DRI process, as explained in Chapter 3 these conclusions are based on only a handful of the kinetic models that were developed. By applying a different model from a different source, results that are obtained will differ with the results attained by the models of Hamadeh, Mirgaux, and Patisson [50] and Rahimi and Niksiar [96]. To make sure that the results hold for the other types of kinetic DRI modelling, therefore the following steps for future research are recommended.

- **Kinetic Model Comparison Study**

To determine which of the kinetic reduction models that are reported in literature most accurately represents the real DRI process, a thorough comparison study is recommended. By comparing the different kinetic models from literature, also a better understanding into the shortcomings and limitations of currently applied models is obtained.

- **Dynamic Mass and Energy Balance Study**

Although the models applied in this thesis do have a time dependency, no further research was conducted in the dynamic behaviour of the chemical reactions inside a SF. For a follow-up study in this topic, it is suggested that a dynamic model is applied instead of the steady-state models that were used throughout this thesis. It is recommended to work with dynamic mass and energy balances, so that the temperature change of the chemical constituents throughout the SF can be determined.

- **Study on the minimal $CH_4$ requirements for carburization**

Now that the dominance of MC over BR in the carburization process has been established, it would be interesting to study the minimum requirements of $CH_4$ for sufficient carburization of the DRI end product. This can be done experimentally or through a fluid dynamic model, for example. Research into the minimum $CH_4$ requirements also provides new insights in the economics of the natural gas-based DRI process. It can then be determined what the costs are of gradually increasing $H_2$ concentrations with gradually decreasing $CH_4$ concentrations for the DRI process.

- **Experimental Validation**

Although many a study has already been conducted on the $H_2$ and syngas-based DRI process, it is not possible to immediately validate the results obtained in this thesis with experimental data. It is therefore interesting to see if the conclusions and findings of this study can be proven experimentally. This can prove to be worthwhile for all parts of the DRI process: for the gas phase reactions, direct reduction and carburization processes.

- **Laboratory Study on Sustainable Carburization Sources**

Despite the presence of experimental data on the sustainable carburization sources provided by Adedipe et al. [2], the available data is limited and only for small-scale operations. It would be interesting to see if these processes are easily scalable and to which extent carburization of the DRI product occurs for the different sustainable carbon sources. Furthermore, it is possible to experiment with organic carbon sources closer to home, like agricultural waste in the province of North-Holland.

# References


[1] S. Abdenour et al. "Influence of the carburization time on the structural and mechanical properties of XC20 steel". In: *Materials Research Express* 8 (8 Aug. 2021).

[2] O. Adedipe et al. "Sustainable carburization of low carbon steel using organic additives: A review". In: *Sustainable Materials and Technologies* 38 (Dec. 2023).

[3] K. Alhumaizi, A. Ajbar, and M. Soliman. "Modelling the complex interactions between reformer and reduction furnace in a midrex-based iron plant". In: *Canadian Journal of Chemical Engineering* 90 (5 Oct. 2012), pp. 1120–1141.

[4] E.K. Ampaw et al. "Carbonitriding "Pack Cyaniding" of Ductile Irons". In: *Advanced Materials Research* 1132 (Dec. 2015), pp. 330–348.

[5] R. Amundson. "Solid-fluid interactions in fixed and moving beds". In: *Industrial Engineering Chemistry* 1 (48 1956), pp. 26–35.

[6] M. Arandas, V. Chevrier, and C. Ravenscroft. "New technologies for maximizing operational flexibility of MIDREX® DRI plants: adjusting product carbon in MIDREX® DRI products." In: *AISTECH* (2017), pp. 979–984.

[7] E.K. Arthur and S.T. Azeko. "Surface hardening of ferrous materials with cassava (Manihot spp.) waste: A review". In: *Scientific African* 9 (Sept. 2020).

[8] E.K. Arthur et al. "Nano- and Macro-wear of Bio-carbo-nitrided AISI 8620 Steel Surfaces". In: *Metallurgical and Materials Transactions A: Physical Metallurgy and Materials Science* 46 (12 Oct. 2015), pp. 5810–5829.

[9] M. Atsushi, H. Uemura, and T. Sakaguchi. "MIDREX processes". In: *Kobelco Technology Review* (29 Dec. 2010), pp. 50–57.

[10] K. Soares Augusto and S. Paciornik. "Porosity characterization of iron ore pellets by x-ray microtomography". In: *Materials Research* 21 (2 2018).

[11] T. Battle et al. *The Direct Reduction of Iron*. Vol. 3. Elsevier Ltd., 2014, pp. 89–176. ISBN: 9780080969886.

[12] R. Béchara et al. "Carbon impact mitigation of the iron ore direct reduction process through computer-aided optimization and design changes". In: *Metals* 10 (3 2020).

[13] R. Béchara et al. "Optimization of the iron ore direct reduction process through multiscale process modeling". In: *Materials* 11 (7 June 2018).

[14] J. Van den Berg. *Wachtlijst stroomnet explodeert door energietransitie, jaren wachten op stroom geen uitzondering*. Ed. by De Volkskrant. 21-02-2024.

[15] A. Bhaskar et al. "Decarbonizing primary steel production: Techno-economic assessment of a hydrogen based green steel production plant in Norway". In: *Journal of Cleaner Production* 350 (May 2022).

[16] Bloomberg. *EUR to USD Exchange Rate*. URL: `https://www.bloomberg.com/quote/EURUSD:CUR` (visited on 02/26/2024).

[17] M. Van Bokkum. *Tata hakt knoop door en gaat tóch staal maken met waterstof*. Ed. by NRC. 27-07-2023.

[18] A. Bonalde, A. Henriquez, and M. Manrique. "Kinetic Analysis of the Iron Oxide Reduction Using Hydrogen-Carbon Monoxide Mixtures as Reducing Agent". In: *ISIJ International* 45 (9 2005), pp. 1255–1260.

[19] N. Bond, R. Symonds, and R. Hughes. "Pressurized Chemical Looping for Direct Reduced Iron Production: Carbon Neutral Process Configuration and Performance". In: *Energies* 15 (14 July 2022).

[20] J. Bosch, I. Staffell, and A.D. Hawkes. "Global levelised cost of electricity from offshore wind". In: *Energy* 189 (Dec. 2019).

[21] W.F. Breunis. “Hydrogen gas production from offshore wind energy”. In: (2021).

[22] J. Burgess. *Inflation pushes Europe green hydrogen costs up by Eur2/kg*. Ed. by A. Critchlow. 27-09-2023.

[23] P. Canu et al. “Multiphysics simulation of a DRP shaft furnace”. In: (2013).

[24] P. Cavaliere. “Direct Reduced Iron: Most Efficient Technologies for Greenhouse Emissions Abatement”. In: Springer International Publishing, 2019, pp. 419–484.

[25] P. Cavaliere, A. Perrone, and D. Marsano. “Effect of reducing atmosphere on the direct reduction of iron oxides pellets”. In: *Powder Technology* 426 (Aug. 2023).

[26] Z. Chen et al. “Reduction kinetics of hematite powder in hydrogen atmosphere at moderate temperatures”. In: *Metals* 8 (10 Oct. 2018).

[27] V.F. Chevrier. “Ultra-Low CO2 Ironmaking: Transitioning to the Hydrogen Economy”. In: (Mar. 2020). Ed. by MIDREX.

[28] J. Chipman. “Thermodynamics and Phase Diagram of the Fe-C System”. In: *Metallurgical Transactions* 3 (January 1972), pp. 55–64.

[29] A. Christensen. “Assessment of Hydrogen Production Costs from Electrolysis: United States and Europe”. In: (2020).

[30] C.F. Coelho and G. Morales. “Sustainability in pelletizing iron ore through the Industrial Ecology and Cleaner Production Program”. In: *Independent Journal of Management  Production* 4 (1 June 2013).

[31] L. Collins. *European-made green hydrogen would be cheaper in EU than any imports by 2050, says European Commission report*. 9-08-2023.

[32] A. Ranzani Da Costa, D. Wagner, and F. Patisson. “Modelling a new, low CO2 emissions, hydrogen steelmaking process”. In: *Journal of Cleaner Production* 46 (2013), pp. 27–35.

[33] M. David, C. Ocampo-Martinez, and R. Sanchez-Peña. “Advances in Alkaline water electrolyzers: A review”. In: (2019).

[34] P. Duarte and D. Pauluzzi. “Premium Quality DRI Products from ENERGIRON”. In: (July 2019). Ed. by Danieli, pp. 1–19.

[35] B. Dussoubs et al. “Modelling of a moving bed furnace for the production of uranium tetrafluoride Part 1: Formulation of the model”. In: *Chemical Engineering Science* 58 (12 2003), pp. 2617–2627.

[36] Duurzaam-ondernemen.nl. *Locatie Tata Steel in IJmuiden erkend als een van de meest CO2-efficiënte staalfabrieken in de wereld*. 24-10-2022.

[37] Duurzaam-ondernemen.nl. *Tata Steel Nederland levert Groen Staal-plan in met nadruk op vermindering uitstoot*. 4-11-2023.

[38] V. Eckert. *Imported hydrogen can beat EU production costs by 2030 - study*. Ed. by E. Osmond. 24-01-2023.

[39] B. Van Eeckhout et al. “Economic comparison of VSC HVDC and HVAC as transmission system for a 300MW offshore wind farm”. In: *European Transactions on Electrical Power* 20 (5 July 2010), pp. 661–671.

[40] S. Eggelston et al. *2006 IPCC Guidelines for National Greenhouse Gas Inventories*. Ed. by International Panel for Climate Change. 2006.

[41] Energy Storage NL. *Netcongestie zet door: bijna heel Nederland op rood*. 18-10-2023.

[42] Energy Transitions Commission. *Making Net-Zero Steel Possible*. Sept. 2022.

[43] Entsoe Transparancy Platform. *Day-ahead prices*. URL: `https://www.entsoe.eu` (visited on 12/01/2023).

[44] A.A. El-Geassy, K.A. Shehata, and S.Y. Ezz. “Mechanism of Iron Oxide Reduction with Hydrogen/Carbon Monoxide Mixtures·”. In: *Transaction ISIJ* 17 (1977), pp. 629–635.

[45] M. Geerdes et al. *Modern Blast Furnace Ironmaking*. 3rd ed. Amsterdam, The Netherlands: Delft University Press, 2015. ISBN: 978-1-61499-498-5.

[46] A. Zare Ghadi, M. Sadegh Valipour, and M. Biglari. “Mathematical modelling of wustite pellet reduction: grain model in comparison with USCM”. In: *Ironmaking and Steelmaking* 43 (6 July 2016), pp. 418–425.

[47] A. Zare Ghadi et al. “A Review on the Modeling of Direct Reduction of Iron Oxides in Gas-Based Shaft Furnaces”. In: *steel research international* 94 (6 June 2023), p. 2200742.

[48] A. Zare Ghadi et al. “A Review on the Modeling of Gaseous Reduction of Iron Oxide Pellets”. In: *Steel Research International* 91 (1 Jan. 2020).

[49] D. Godkin and D.K. Rubin. *Deals Reached for Two Canada Green Hydrogen Megaprojects*. Ed. by Engineering News-Record. 16-11-2023.

[50] H. Hamadeh, O. Mirgaux, and F. Patisson. “Detailed modeling of the direct reduction of iron ore in a shaft furnace”. In: *Materials* 11 (10 Oct. 2018).

[51] J. Hampp, M. Düren, and T. Brown. “Import options for chemical energy carriers from renewable sources to Germany”. In: *PLoS ONE* 18 (Feb. 2023).

[52] J. He et al. “Improving the carbon resistance of iron-based oxygen carrier for hydrogen production via chemical looping steam methane reforming: A review”. In: *Fuel* 351 (Nov. 2023).

[53] A. Heidari et al. “A review on the kinetics of iron ore reduction by hydrogen”. In: *Materials* 14 (24 Dec. 2021).

[54] IEA, IRENA UN Climate Change High-Level Champions. *Breakthrough Agenda Report 2023*. Sept. 2023.

[55] International Energy Agency. *Iron and Steel Technology Roadmap*. Oct. 2020.

[56] X. Jiang, L. Wang, and F. Man Shen. “Shaft furnace direct reduction technology — Midrex and Energiron”. In: *Advanced Materials Research* 805-806 (2013), pp. 654–659.

[57] Joint Research Centre. *EU climate targets: how to decarbonise the steel industry*. Ed. by European Commission EU Science Hub. June 2022.

[58] M.Y. Kolawole, E.A. Awoyemi, and O.M. Abiona. “Potential of Date-Seed/Snail Shells as a Carburizer for Enhanced Mechanical Properties of Mild-Steel”. In: *Journal of Engineering Sciences* 8 (2 2021).

[59] V. Kolisnichenko. *The Netherlands reduced steel production by 25% y/y in 2023*. Ed. by GMK Centre. 8-02-2024.

[60] P. Koukkari, R. Pajarre, and P. Blomberg. “Reaction rates as virtual constraints in Gibbs energy minimization”. In: *Pure and Applied Chemistry* 83 (5 2011), pp. 1063–1074.

[61] A. Krüger et al. “Integration of water electrolysis for fossil-free steel production”. In: *International Journal of Hydrogen Energy* 45 (55 Nov. 2020), pp. 29966–29977.

[62] S. Kuang, Z. Li, and A. Yu. “Review on Modeling and Simulation of Blast Furnace”. In: *Steel Research International* 89 (1 Jan. 2018).

[63] T.K. Sandeep Kumar et al. “Carburization Behavior of Hydrogen-Reduced DRI Using Synthetic Bio-syngas Mixtures as Fossil-Free Carbon Sources”. In: *Journal of Sustainable Metallurgy* 8 (4 Dec. 2022), pp. 1546–1560.

[64] T.K. Sandeep Kumar et al. “Effect of Temperature and Gas Mixtures on Cementite Formation During the Carburization of Hydrogen-Reduced DRI”. In: *Journal of Sustainable Metallurgy* 8 (4 Dec. 2022), pp. 1450–1464.

[65] A. Lea. *Green steel needs hydrogen price below* $2/kg$. Ed. by Argus. 11-06-2022.

[66] W. Liu et al. “The production and application of hydrogen in steel industry”. In: *International Journal of Hydrogen Energy* 46 (17 Mar. 2021), pp. 10548–10569.

[67] Z. Liu et al. “Study on optimization of reduction temperature of hydrogen-based Shaft Furnace—Numerical simulation and multi-criteria evaluation”. In: *International Journal of Hydrogen Energy* (May 2023).

[68] Q. Lyu et al. “Effect of hydrogen addition on reduction behavior of iron oxides in gas-injection blast furnace”. In: *Thermochimica Acta* 648 (Feb. 2017), pp. 79–90.

[69] P. Martin. *Australian territory puts oil giant's green hydrogen project on fast track for regulatory approvals*. Ed. by Hydrogen Insight. 8-01-2024.

[70] S. Martynov, S. Brown, and H. Mahgerefteh. "An extended Peng-Robinson equation of state for carbon dioxide solid-vapor equilibrium". In: *Greenhouse Gases: Science and Technology* 3 (2 2013), pp. 136–147.

[71] D.A. McQuarrie and J.D. Simon. *Physical Chemistry: A Molecular Approach*. 1st ed. Sausulito, California, USA: University Science Books, Sausalito, California, 1997. ISBN: 978-0-470-03037-0.

[72] A. Meshram et al. "Modeling Isothermal Reduction of Iron Ore Pellet Using Finite Element Analysis Method: Experiments  Validation". In: *Metals* 12 (12 Dec. 2022).

[73] P. Metolina et al. "Hydrogen direct reduction ironmaking process for zero CO2 emission: A study on the effect of particle properties changes during the multiple non-catalytic gas-solid reactions". In: *Minerals Engineering* 201 (Oct. 2023), p. 108188.

[74] M.J. Moran and H.N. Shapiro. *Fundamentals of Engineering Thermodynamics*. 5th ed. West Sussex, England: John Wiley  Sons, Inc., 2006. ISBN: 978-0-470-03037-0.

[75] Y. Nasiri, M. Panjepour, and M. Ahmadian. "The kinetics of hematite reduction and cementite formation with CH4-H2-Ar gas mixture". In: *International Journal of Mineral Processing* 153 (Aug. 2016), pp. 17–28.

[76] A.A. Abo El-Nasr, A. Saleh, and A.A. Alshennawy. "Porosity measurement of iron oxide by using computer vision system". In: *International Journal of Engineering Research and Technology* 13 (4 2020), pp. 653–659.

[77] Nederlandse Emissieautoriteit. *Historische daling CO2-uitstoot grote industrie, vooral Chemische bedrijven stoten veel minder uit*. Ed. by NEa. 14-04-2023.

[78] E.D. Negri, M.D. Alfano, and M.G. Chiovetta. "Direct reduction of hematite in a moving bed. Comparison between one- and three-interface pellet models". In: *Chemical Engineering Science* 42 (10 Mar. 1987), pp. 2472–2475.

[79] E.D. Negri, O.M. Alfano, and M.G. Chiovetta. "Moving-Bed Reactor Model for the Direct Reduction of Hematite. Parametric Study". In: *Ind. Eng. Chem. Res* 34 (1995), pp. 4266–4276.

[80] A. Niksiar and A. Rahimi. "A study on deviation of noncatalytic gas-solid reaction models due to heat effects and changing of solid structure". In: *Powder Technology* 193 (1 July 2009), pp. 101–109.

[81] NOS Nieuws. *Van auto's tot wasmachines: dit gebeurt er met Tata's staal uit IJmuiden*. 23-07-2023.

[82] S.M.M. Nouri, H. Ale Ebrahim, and E. Jamshidi. "Simulation of direct reduction reactor by the grain model". In: *Chemical Engineering Journal* 166 (2 Jan. 2011), pp. 704–709.

[83] Nowtricity. *Real time elecricity production emissions by country*. URL: https://www.nowtricity.com/ (visited on 02/26/2024).

[84] M. Pahle et al. "The EU-ETS price through 2030 and beyond: A closer look at drivers, models and assumptions". In: (2022).

[85] C. Palladino. *Lex in depth: the staggering cost of a green hydrogen economy*. Ed. by The Financial Times. 28-05-2023.

[86] D. R. Parisi and M. A. Laborde. "Modeling of counter current moving bed gas-solid reactor used in direct reduction of iron ore". In: *Chemical Engineering Journal* 104 (1-3 Nov. 2004), pp. 35–43.

[87] F. Patisson and O. Mirgaux. "Hydrogen ironmaking: How it works". In: *Metals* 10 (7 July 2020), pp. 1–15.

[88] D. Pauluzzi et al. "CFD Study of an Energiron Reactor Fed With Different Concentrations of Hydrogen". In: (2021).

[89] J. Perpiñán et al. "Integration of carbon capture technologies in blast furnace based steel making: A comprehensive and systematic review". In: *Fuel* 336 (Mar. 2023).

[90] A.J. Pimm, T.T. Cockerill, and W.F. Gale. "Energy system requirements of fossil-free steelmaking using hydrogen direct reduction". In: *Journal of Cleaner Production* 312 (Aug. 2021).

[91] British Steel plc. *Refsource 139531 - Midrex Alabama*. 1997.

[92] H.M. Polat et al. “Solving Chemical Absorption Equilibria using Free Energy and Quantum Chemistry Calculations: Methodology, Limitations, and New Open-Source Software”. In: *Journal of Chemical Theory and Computation* 19 (9 May 2023), pp. 2616–2629.

[93] R. Privat et al. “Teaching the Concept of Gibbs Energy Minimization through Its Application to Phase-Equilibrium Calculation”. In: *Journal of Chemical Education* 93 (9 Sept. 2016), pp. 1569–1577.

[94] A. Rahbari et al. “Combined Steam Reforming of Methane and Formic Acid to Produce Syngas with an Adjustable H2:CO Ratio”. In: *Industrial and Engineering Chemistry Research* 57 (31 Aug. 2018), pp. 10663–10674.

[95] R. Rahbari. “Thermodynamics of Industrially Relevant Systems: Method Development and Applications”. In: (2020).

[96] A. Rahimi and A. Niksiar. “A general model for moving-bed reactors with multiple chemical reactions part I: Model formulation”. In: *International Journal of Mineral Processing* 124 (2013), pp. 58–66.

[97] A. Rahimi and A. Niksiar. “A general model for moving-bed reactors with multiple chemical reactions, Part II: Effect of kinetic model”. In: *International Journal of Mineral Processing* 124 (2013), pp. 67–74.

[98] K. Rechberger et al. “Green Hydrogen-Based Direct Reduction for Low-Carbon Steelmaking”. In: *Steel Research International* 91 (11 Nov. 2020).

[99] T. Ramos Ribeiro et al. “C–O–H2 ternary diagram for evaluation of carbon activity in CH4-containing gas mixtures”. In: *Journal of Materials Research and Technology* 13 (July 2021), pp. 1576–1585.

[100] J. Ripke and J. Kopfle. “MIDREX H2: Ultimate Low CO2 Ironmaking and its place in the new Hydrogen Economy”. In: *ESTAD Conference* (June 2017).

[101] A. Rogeau et al. “Techno-economic evaluation and resource assessment of hydrogen production through offshore wind farms: a European perspective”. In: (2023).

[102] E. Salucci et al. “Modelling of iron oxide reduction with hydrogen”. In: *Computer Aided Chemical Engineering* 52 (Jan. 2023), pp. 715–720.

[103] S. Sarkar et al. “Modeling MIDREX Based Process Configurations for Energy and Emission Analysis”. In: *Steel Research International* 89 (2 Feb. 2018).

[104] M. Shahabuddin, G. Brooks, and M. Akbar Rhamdhani. “Decarbonisation and hydrogen integration of steel industries: Recent development, challenges and technoeconomic analysis”. In: *Journal of Cleaner Production* 395 (Apr. 2023).

[105] A. Shams and F. Moazeni. “Modeling and Simulation of the MIDREX Shaft Furnace: Reduction, Transition and Cooling Zones”. In: *JOM* 67 (11 Aug. 2015), pp. 2681–2689.

[106] L. Shao et al. “Computational analysis of hydrogen reduction of iron oxide pellets in a shaft furnace process”. In: *Renewable Energy* 179 (Dec. 2021), pp. 1537–1547.

[107] R. Singh. *Middle East’s clean hydrogen capacity plans double year on year*. Ed. by H. Edwardes-Evans. 25-09-2023.

[108] A. Singlitico, J. Østergaard, and S. Chatzivasileiadis. “Onshore, offshore or in-turbine electrolysis? Techno-economic overview of alternative integration designs for green hydrogen production into Offshore Wind Power Hubs”. In: *Renewable and Sustainable Energy Transition* 1 (Aug. 2021).

[109] D. Spreitzer and J. Schenk. “Reduction of Iron Oxides with Hydrogen—A Review”. In: *Steel Research International* 90 (10 Oct. 2019).

[110] Supriyono and Jamasri. “Holding time effect of pack carburizing on fatigue characteristic of v-notch shaft steel specimens”. In: vol. 1855. American Institute of Physics Inc., June 2017.

[111] J. Szekely and J.W. Evans. “A structural model for gas-solid reactions with a moving boundary”. In: *Chemical Engineering Science* 25 (1970), pp. 1091–107.

[112] K.H. Tacke and R. Steffen. “Hydrogen for the reduction of iron ores—State of the art and future aspects”. In: *Stahl und Eisen* 124 (4 2004), pp. 45–52.

[113] Takahashi, Yagi, and Omori. "Reduction of Iron Oxide Pellets with Hydrogen". In: *Science reports of the Research Institutes* 23 (July 1971), pp. 9–30.

[114] Y. Takenaka et al. "Mathematical model of direct reduction shaft furnace and its application to actual operations of a model plant". In: *Computers and Chemical Engineering* IO (1 1986), pp. 61–74.

[115] TATA Steel. *Duurzaamheidsverslag 2022-2023*. 2023. URL: `https://www.tatasteelnederland.com/groen-staal-en-duurzaamheid` (visited on 11/13/2023).

[116] Trading Economics. *Iron Ore Price*. URL: `https://tradingeconomics.com/commodity/iron-ore` (visited on 10/10/2023).

[117] R.E. Treybal. *Mass-Transfer Operations*. 3rd ed. Singapore: McGraw-Hill Book Company, Singapore, 1981.

[118] M.S. Valipour, M.Y. Motamed Hashemi, and Y. Saboohi. "Mathematical modeling of the reaction in an iron ore pellet using a mixture of hydrogen, water vapor, carbon monoxide and carbon dioxide: an isothermal study". In: *Advanced Powder Technology* 17 (3 Jan. 2006), pp. 277–295.

[119] M.S. Valipour and Y. Saboohi. "Numerical investigation of nonisothermal reduction of hematite using Syngas: The shaft scale study". In: *Modelling and Simulation in Materials Science and Engineering* 15 (5 Sept. 2007), pp. 487–507.

[120] E. Vartiainen et al. "True Cost of Solar Hydrogen". In: *Solar RRL* 6 (5 May 2022).

[121] V. Vogl, M. Åhman, and L.J. Nilsson. "Assessment of hydrogen direct reduction for fossil-free steelmaking". In: *Journal of Cleaner Production* 203 (Dec. 2018), pp. 736–745.

[122] D.R. Wicakso et al. "Integration of pyrolysis - Tar decomposition over porous low grade iron ore". In: vol. 722. Institute of Physics Publishing, Jan. 2020.

[123] Wind Europe. *Wind energy is the cheapest source of electricity generation*. 29-03-2019.

[124] E. Wołowiec-Korecka et al. "Calculation of the mixture flow in a low-pressure carburizing process". In: *Metals* 9 (4 Apr. 2019).

[125] World Steel Association. *December 2023 crude steel production and 2023 global crude steel production totals*. Jan. 2024.

[126] World Steel Association. *Hydrogen (H2)-based ironmaking*. June 2022.

[127] World Steel Association. *worldsteel Short Range Outlook October 2023*. Oct. 2023.

[128] W. Xu et al. "Material Flow Analysis of CO2 Emissions from Blast Furnace and Basic Oxygen Furnace Steelmaking Systems in China". In: *Steel Research International* 86 (9 Sept. 2015), pp. 1063–1072.

[129] H. Yermolenko. *The price of carbon emissions in the EU may reach €400/t by 2040 – forecast*. Ed. by GMK Centre. 6-10-2023.

[130] A. Zugliano et al. "Online modelling of ENERGIRON direct reduction shaft furnaces". In: *IFAC Proceedings Volumes (IFAC-PapersOnline)* 15 (2013), pp. 346–351.

[131] H. B. Zuo et al. "Reduction kinetics of iron oxide pellets with H2 and CO mixtures". In: *International Journal of Minerals, Metallurgy and Materials* 22 (7 July 2015), pp. 688–696.

# A

# MIDREX & Energiron Plant Data

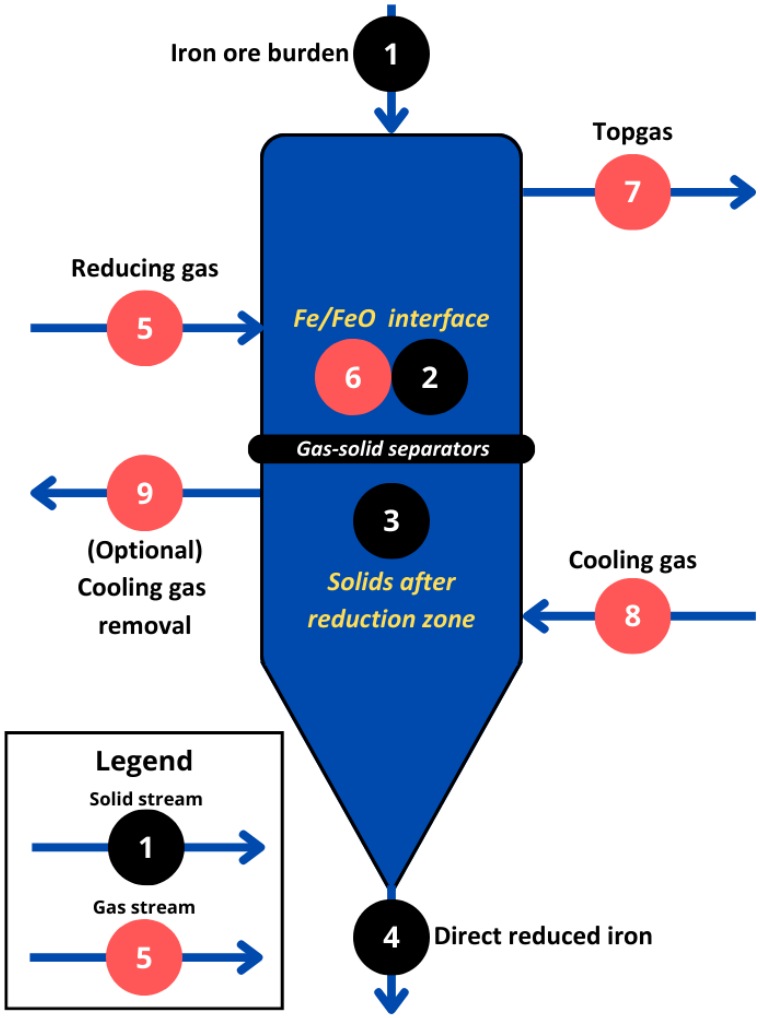


**Figure A.1:** A schematic overview of a shaft furnace in both the MIDREX and Energiron processes with numbered streams and furnace positions. Black indicates a solid flow, while red marks a gas flow.

In this appendix, data from existing MIDREX and Energiron plants is summarised and tabulated. All relevant streams and positions are labeled with a number, as seen in Figure A.1. These numbers will be used as a reference throughout the rest of this appendix.

# A.1. MIDREX Plant in Mobile, Alabama, USA

**Table A.1:** Solid flows of the MIDREX plant in Mobile, Alabama, USA.

| **Operating Conditions** | **Stream 1** | **Stream 2** | **Stream 3** | **Stream 4** |
|---|---|---|---|---|
| *DRI Production Rate* [t/h] | 68 | 68 | 68 | 68 |
| *Flowrate* [kg/h] | 97900 | 85606 | 69400 | 68000 |
| *Pressure* [bar] | N/A | N/A | N/A | N/A |
| *Temperature* [K] | 298 | 1120 | 1113 | 323 |
| *Metallization* | 0.00% | 0.00% | 91.91% | 91.97% |
| **Chemical Species** [wt.%] | | | | |
| $Fe_2O_3$ | 95.22% | 0.00% | 0.00% | 0.00% |
| $FeO$ | 0.29% | 96.84% | 9.68% | 9.63% |
| $Fe$ | 0.00% | 0.00% | 85.47% | 85.00% |
| $C(s)$ | 0.00% | 0.00% | 0.96% | 1.50% |
| *Gangue* | 2.80% | 3.16% | 3.89% | 3.87% |
| *Loss On Ignition (e.g.* $H_2O$*)* | 1.69% | 0.00% | 0.00% | 0.00% |
| **Total** | 100.00% | 100.00% | 100.00% | 100.00% |

**Table A.2:** Gas flows of the MIDREX plant in Mobile, Alabama, USA.

| **Operating Conditions** | **Stream 5** | **Stream 6** | **Stream 7** | **Stream 8** | **Stream 9** |
|---|---|---|---|---|---|
| *DRI Production Rate* [t/h] | 68 | 68 | 68 | 68 | 68 |
| *Flowrate* [$Nm^3$/h] | 114226 | 119197 | 119197 | 49475 | 49232 |
| *Pressure* [bar] | 1.838 | 1.5 | 1.272 | 1.958 | 1.838 |
| *Temperature* [K] | 1113 | 1173 | 653 | 313 | 757 |
| **Chemical Species** [vol.%] | | | | | |
| $CO$ | 34.76% | 24.14% | 20.36% | 2.60% | 2.65% |
| $CO_2$ | 2.36% | 11.41% | 15.19% | 0.93% | 0.93% |
| $H_2$ | 53.89% | 43.85% | 36.82% | 54.58% | 55.61% |
| $H_2O$ | 5.21% | 17.52% | 24.55% | 3.71% | 3.53% |
| $N_2$ | 0.60% | 0.82% | 0.82% | 11.76% | 11.98% |
| $CH_4$ | 3.09% | 2.26% | 2.26% | 26.30% | 25.30% |
| $C_xH_y$ | 0.09% | 0.00% | 0.00% | 0.10% | 0.00% |
| **Total** | 100.00% | 100.00% | 100.00% | 99.98% | 100.00% |
| **Chemical Species** [kg mol/h] | | | | | |
| $CO$ | 1771.44 | 1283.99 | 1082.74 | 57.39 | 58.21 |
| $CO_2$ | 120.27 | 606.55 | 807.80 | 20.53 | 20.43 |
| $H_2$ | 2746.34 | 2331.83 | 1958.08 | 1204.76 | 1221.46 |
| $H_2O$ | 265.51 | 931.81 | 1305.56 | 81.89 | 77.54 |
| $N_2$ | 30.58 | 43.61 | 43.61 | 259.58 | 263.14 |
| $CH_4$ | 157.47 | 120.19 | 120.19 | 580.53 | 555.71 |
| $C_xH_y$ | 4.59 | 0.00 | 0.00 | 2.21 | 0.00 |
| **Total** | 5096.19 | 5317.97 | 5317.97 | 2206.88 | 2196.48 |

## A.2. MIDREX Plant in Contrecoeur, Québec, Canada

**Table A.3:** Solid flows of the MIDREX plant in Contrecoeur, Québec, Canada [13, 50].

| **Operating Conditions** | **Stream 1** | **Stream 4** |
|---|---|---|
| *DRI Production Rate* [t/h] | 119.2 | 119.2 |
| *Flowrate* [kg/h] | 163944 | 119200 |
| *Pressure* [bar] | N/A | N/A |
| *Temperature* [K] | 263 | - |
| *Metallization* | 0.00% | 93.80% |
| **Chemical Species** [wt.%] | | |
| $Fe_2O_3$ | 96.65% | 0.00% |
| $FeO$ | 0.00% | 7.47% |
| $Fe$ | 0.00% | 85.72% |
| $C(s)$ | 0.00% | 2.00% |
| *Gangue* | 3.35% | 4.71% |
| *Loss On Ignition (e.g.* $H_2O$*)* | 0.00% | 0.00% |
| **Total** | 100.00% | 100.00% |

**Table A.4:** Gas flows of the MIDREX plant in Contrecoeur, Québec, Canada [13, 50].

| **Operating Conditions** | **Stream 5** | **Stream 7** | **Stream 8** |
|---|---|---|---|
| *DRI Production Rate* [t/h] | 119.2 | 119.2 | 119.2 |
| *Flowrate* | 7841 [kmol/h] | 193000 [$Nm^3$/h] | 1804 [kmol/h] |
| *Pressure* [bar] | 1.78 | 1.42 | - |
| *Temperature* [K] | 1230 | 558 | 314 |
| **Chemical Species** [vol.%] | | | |
| $CO$ | 32.71% | 19.58% | 4.30% |
| $CO_2$ | 2.40% | 17.09% | 2.40% |
| $H_2$ | 49.66% | 40.28% | 13.42% |
| $H_2O$ | 4.28% | 19.03% | 3.20% |
| $N_2$ | 1.76% | 1.02% | 0.78% |
| $CH_4$ | 9.08% | 2.95% | 75.90% |
| $C_xH_y$ | 0.11% | 0.05% | 0.00% |
| **Total** | 100.00% | 100.00% | 100.00% |

## A.3. MIDREX Plant from Gilmore near Portland, Oregon, USA

**Table A.5:** Solid flows from Gilmore near Portland, Oregon, USA [13, 50, 105].

| **Operating Conditions** | **Stream 1** | **Stream 4** |
|---|---|---|
| *DRI Production Rate* [t/h] | 26.4 | 26.4 |
| *Flowrate* [kg/h] | 37440 | 119200 |
| *Pressure* [bar] | N/A | N/A |
| *Temperature* [K] | 303 | 316 |
| *Metallization* | 0.00% | 92.90% |
| **Chemical Species** [wt.%] | | |
| $Fe_2O_3$ | 95.00% | 0.00% |
| $FeO$ | 0.00% | 8.87% |
| $Fe$ | 0.00% | 83.56% |
| $C(s)$ | 0.00% | 1.42% |
| *Gangue* | 5.00% | 6.15% |
| *Loss On Ignition (e.g.* $H_2O$*)* | 0.00% | 0.00% |
| **Total** | 100.00% | 100.00% |

**Table A.6:** Gas flows of the MIDREX plant from Gilmore near Portland, Oregon, USA [13, 50, 105].

| **Operating Conditions** | **Stream 5** | **Stream 7** | **Stream 8** | **Stream 9** |
|---|---|---|---|---|
| *DRI Production Rate* [t/h] | 26.4 | 26.4 | 26.4 | 26.4 |
| *Flowrate* [$Nm^3/h$] | 53863 | - | 11800 | 10607 |
| *Pressure* [bar] | 1.4 | 1.31 | - | - |
| *Temperature* [K] | 1203 | 285 | 316 | 733 |
| **Chemical Species** [vol.%] | | | | |
| $CO$ | 29.97% | 18.90% | 3.10% | 2.10% |
| $CO_2$ | 4.80% | 14.30% | 3.40% | 4.39% |
| $H_2$ | 52.58% | 37.00% | 21.36% | 24.26% |
| $H_2O$ | 4.65% | 21.20% | 1.96% | 1.96% |
| $N_2$ | 6.30% | 7.67% | 2.38% | 1.85% |
| $CH_4$ | 1.80% | 0.93% | 67.80% | 65.66% |
| $C_xH_y$ | 0.00% | 0.00% | 0.00% | 0.00% |
| **Total** | 100.10% | 100.00% | 100.00% | 100.22% |

## A.4. Energiron Plant from Zugliano, 2013

**Table A.7:** Solid flows of the Energiron plant as mentioned by Zugliano, 2013 [130].

| **Operating Conditions** | **Stream 1** | **Stream 4** |
|---|---|---|
| *DRI Production Rate* [t/h] | 206.41 | 206.41 |
| *Flowrate* [kg/h] | 290284 | 206410 |
| *Pressure* [bar] | N/A | N/A |
| *Temperature* [K] | 340 | 907 |
| *Metallization* | 0.00% | 94.57% |
| **Chemical Species** [wt.%] | | |
| $Fe_2O_3$ | 96.18% | 0.00% |
| $FeO$ | 0.14% | 0.00% |
| $Fe$ | 0.00% | 94.57% |
| $C(s)$ | 0.00% | 2.28% |
| *Gangue* | 2.29% | 3.17% |
| *Loss On Ignition (e.g.* $H_2O$*)* | 1.39% | 0.00 |
| **Total** | 100.00% | 100.02% |

**Table A.8:** Gas flows of the Energiron plant as mentioned by Zugliano, 2013 [130].

| **Operating Conditions** | **Stream 5** | **Stream 7** | **Stream 8** |
|---|---|---|---|
| *DRI Production Rate* [t/h] | 206.41 | 206.41 | 206.41 |
| *Flowrate* [$Nm^3/h$] | 345813 | 390915 | 10590 |
| *Pressure* [bar] | 7.24 | 6.60 | 8.89 |
| *Temperature* [K] | 1235 | 685.28 | 298 |
| **Chemical Species** [vol.%] | | | |
| $CO$ | 16.20% | 13.60% | 0.00% |
| $CO_2$ | 4.98% | 7.28% | 0.00% |
| $H_2$ | 66.29% | 43.32% | 0.00% |
| $H_2O$ | 2.96% | 28.81% | 0.00% |
| $N_2$ | 1.27% | 1.13% | 7.50% |
| $CH_4$ | 8.30% | 5.86% | 92.50% |
| $C_xH_y$ | 0.00% | 0.00% | 0.00% |
| **Total** | 100.00% | 100.00% | 100.00% |

# B

# Thermodynamic Equilibrium Modelling

## B.1. Gibbs Minimization

To calculate the Gibbs free energy of a homogeneous gas phase reaction of $n$ different gases, Equation (B.1) applies [95].

$$\Delta {G_R}^0 = \sum_{j=n} \left(\gamma_j \ \mu_j\right) \tag{B.1}$$

In Equation (B.1), $\gamma_j$ is the stoichiometric coefficient for gaseous component $j$ and $\mu_j$ the chemical potential of component $j$ in [kJ/mol]. The chemical potential of component $j$ can be calculated via Equation (B.2).

$$\mu_j = {\mu_j}^{\mathrm{G}} + RT \ ln\left(\frac{y_j \ \phi_j \ P_{\mathrm{Total}}}{P^\circ}\right) \tag{B.2}$$

All parameters of Equation (B.2) are explicated in Section 3.1. The input for Equation (B.2) is the gas stream data that can be found in Appendix A. Parameter ${\mu_j}^{\mathrm{G}}$ is the ideal gas chemical potential of component $j$ in [kJ/mol], which can be calculated through Equation (B.3).

$${\mu_j}^{\mathrm{G}} = \left[{G_j}^0(T) - {H_j}^0(T_{\mathrm{r}})\right] - \left[{H_j}^0(0K) - {H_j}^0(T_{\mathrm{r}})\right] - D_{0,j} \tag{B.3}$$

In Equation (B.3), ${G_j}^0$ is the standard ideal Gibbs free energy of component $j$ in [kJ/mol], ${H_j}^0$ the standard enthalpy of component $j$ in [kJ/mol], $T$ the absolute temperature in [K], $T_{\mathrm{r}}$ the reference temperature of 298.15 [K] and $D_{0,j}$ the atomization energy in [kJ/mol]. The first two terms between brackets in Equation (B.3) can be directly obtained through the NIST-JANAF tables, whilst $D_{0,j}$ can be calculated via Equation (B.4).

$$D_{0,j} = \sum_{a=m} \left(\beta_a \ \Delta {H_{\mathrm{f},a}}^0(0K)\right) - \Delta {H_{\mathrm{f},j}}^0(0K) \tag{B.4}$$

In Equation (B.4) $\beta_a$ is the stoichiometric coefficient of atom $a$ in molecule $j$, $\Delta {H_{\mathrm{f},a}}^0$ the standard enthalpy of formation of atom $a$ in [kJ/mol] and $\Delta {H_{\mathrm{f},j}}^0$ the standard enthalpy of formation of molecule $j$ in [kJ/mol].

The principle of the Gibbs minimization method is to minimize Equation (B.2) to obtain the equilibrium composition of the gas phase. When Equation (B.2) is minimized, this automatically implies that Equation (B.1) is minimized as well. The MATLAB code used to minimize the Gibbs free energies of the gaseous components in this thesis research is given in Appendix E. For all parameters that are a function of temperature or pressure, the data for the Gibbs minimization was extracted from the NIST-JANAF tables.

## B.2. Peng-Robinson Equation of State

The Peng-Robinson Equation of State (PR-EoS) is given in Equation (3.2), where $v_{\mathrm{m}}$ is the molar volume of the gaseous mixture per mole of mixture, while $a_{\mathrm{m}}$ and $b_{\mathrm{m}}$ are specific pure component parameters. These specific component parameters can be calculated via Equation (B.5) and Equation (B.6) [95].

$$a_{\mathrm{m}} = \sum_{j=1}^{n} \sum_{k=1}^{n} \left( x_j \; x_k \; a_{jk} \right) \tag{B.5}$$

$$b_{\mathrm{m}} = \sum_{k=1}^{n} \left( x_j \; b_j \right) \tag{B.6}$$

$$a_{jk} = (1 - k_{jk}) \; (a_j \; a_k)^{1/2} \tag{B.7}$$

In Equation (B.5) and Equation (B.6), for a total of $n$ components $a_{\mathrm{m}}$ and $b_{\mathrm{m}}$ can be calculated for molecules $j$ and $k$ through the mole fraction of $j$ as $x_j$, the mole fraction of $k$ as $x_k$, parameter $a_{jk}$ which is a function of the binary interaction parameter $k_{jk}$ and the pure component parameters $a_j$ and $b_j$. For $H_2, H_2O, CO, CO_2, CH_4$ and $N_2$ the binary interaction parameters were extracted from Aspen and tabulated in Table B.1. When a molecule pair is not represented in Table B.1, the value given by Aspen equals zero.

**Table B.1:** The binary interaction parameters (BIP) for $H_2, H_2O, CO, CO_2, CH_4$ and $N_2$ as extracted from Aspen. The BIP values not presented in this graph, were extracted from Aspen as zero.

| **Component *j*** | **Component *k*** | $k_{jk}$ / [-] |
|---|---|---|
| $H_2$ | CO | 0.0919 |
| $H_2$ | $CO_2$ | -0.1622 |
| $H_2$ | $N_2$ | 0.103 |
| $H_2$ | $CH_4$ | 0.0156 |
| $CH_4$ | CO | 0.03 |
| $CH_4$ | $CO_2$ | 0.0919 |
| $CH_4$ | $N_2$ | 0.0311 |
| $CO_2$ | CO | -0.017 |
| $CO_2$ | $H_2O$ | 0.12 |
| CO | $N_2$ | 0.0307 |

$$a_j = 0.45724 \cdot \frac{R^2 \; {T_{\mathrm{c},j}}^2}{P_{\mathrm{c},j}} \; \left[ 1 + \left( 0.37464 + 1.54226 \; \omega_j - 0.2699 \; {\omega_j}^2 \right) \; \left( 1 - {T_{\mathrm{r},j}}^{1/2} \right) \right]^2 \tag{B.8}$$

$$b_j = \frac{0.0778 \; R \; T_{\mathrm{c},j}}{P_{\mathrm{c},j}} \tag{B.9}$$

$$T_{\mathrm{r},j} = \frac{T}{T_{\mathrm{c},j}} \tag{B.10}$$

The pure component parameters can be calculated via Equation (B.8) and Equation (B.9). In these formulas, $T_{\mathrm{c},j}$ is the critical temperature of component $j$ in [K], $P_{\mathrm{c},j}$ the critical pressure in [Pa], $\omega_{\mathrm{j}}$ the dimensionless acentric factor and $T_{\mathrm{r},j}$ the dimensionless reduced temperature that can be calculated via Equation (B.10). For $H_2, H_2O, CO, CO_2, CH_4$ and $N_2$, the necessary parameters are tabulated in Table B.2.

**Table B.2:** The parameters necessary for Equation (B.8), Equation (B.9) and Equation (B.10). These are the critical temperature, critical pressure and the acentric factor.

| **Component *j*** | $T_{c,j}$ / [K] | $P_{c,j}$ / [Pa] | $\omega_j$ / [-] |
|---|---|---|---|
| $H_2$ | 33.14 | 1296400 | -0.219 |
| $H_2O$ | 647.1 | 22064000 | 0.3443 |
| CO | 132 | 3400000 | 0.066 |
| $CO_2$ | 304 | 7300000 | 0.228 |
| $CH_4$ | 190 | 4500000 | 0.012 |
| $N_2$ | 126.19 | 3395800 | 0.0372 |

Subsequently, it is possible to derive the fugacity coefficient of a certain gas in the mixture. The formula for the fugacity coefficient is given by Equation (B.11).

$$ln\left(\phi_j\right) = \frac{b_j}{b_m\,(Z_m - 1)} - ln\left(Z_m - B_m\right) - \frac{A_m}{2\sqrt{2}\,B_m}\left[\frac{2\sum_{k=1}^{n}(y_k\,a_{jk})}{a_m} - \frac{b_j}{b_m}\right] ln\left(\frac{Z_m + 2.414\,B_m}{Z_m - 0.414\,B_m}\right) \tag{B.11}$$

In Equation (B.11), the new parameters for a gaseous mixture of $n$ components are the compressibility factor $Z_m$ represented by Equation (B.12) and parameters $A_m$ and $B_m$ given in Equation (B.13) and Equation (B.14), respectively.

$$A_m = \frac{a_m(T)\,P}{R^2\,T^2} \tag{B.12}$$

$$B_m = \frac{b_m\,P}{R\,T} \tag{B.13}$$

$$Z_m = \frac{P\,V}{R\,T} \tag{B.14}$$

For the calculations of the fugacity coefficient of the reducing gas streams and the cooling gas streams of Appendix A.1 and Appendix A.4, the results are shown in Table B.3 and Table B.4 respectively.

**Table B.3:** Fugacity coefficients for all gas streams of MLP as given in Appendix A.1.

| **Stream 5** | **$H_2$** | **$H_2O$** | **CO** | **$CO_2$** | **$CH_4$** | **$N_2$** |
|---|---|---|---|---|---|---|
| $y_j$ / [-] | 0.54 | 0.05 | 0.35 | 0.02 | 0.03 | 0.01 |
| $\phi_j$ / [-] | 1.00 | 1.00 | 1.00 | 1.00 | 1.00 | 1.00 |
| **Stream 6** | | | | | | |
| $y_j$ / [-] | 0.44 | 0.18 | 0.24 | 0.02 | 0.02 | 0.01 |
| $\phi_j$ / [-] | 1.00 | 1.00 | 1.00 | 1.00 | 1.00 | 1.00 |
| **Stream 7** | | | | | | |
| $y_j$ / [-] | 0.37 | 0.25 | 0.20 | 0.15 | 0.02 | 0.01 |
| $\phi_j$ / [-] | 1.00 | 1.00 | 1.00 | 1.00 | 1.00 | 1.00 |
| **Stream 8** | | | | | | |
| $y_j$ / [-] | 0.55 | 0.04 | 0.03 | 0.01 | 0.26 | 0.12 |
| $\phi_j$ / [-] | 1.00 | 0.99 | 1.00 | 0.99 | 1.00 | 1.00 |
| **Stream 9** | | | | | | |
| $y_j$ / [-] | 0.56 | 0.04 | 0.03 | 0.01 | 0.25 | 0.12 |
| $\phi_j$ / [-] | 1.00 | 1.00 | 1.00 | 1.00 | 1.00 | 1.00 |

**Table B.4:** Fugacity coefficients for all gas streams of EMP as given in Appendix A.4.

| **Stream 5** | **$H_2$** | **$H_2O$** | **CO** | **$CO_2$** | **$CH_4$** | **$N_2$** |
|---|---|---|---|---|---|---|
| $y_j$ / [-] | 0.66 | 0.03 | 0.16 | 0.05 | 0.08 | 0.01 |
| $\phi_j$ / [-] | 1.00 | 1.00 | 1.00 | 1.00 | 1.00 | 1.00 |
| **Stream 7** | | | | | | |
| $y_j$ / [-] | 0.43 | 0.29 | 0.14 | 0.07 | 0.06 | 0.01 |
| $\phi_j$ / [-] | 1.00 | 1.00 | 1.00 | 1.00 | 1.00 | 1.00 |
| **Stream 8** | | | | | | |
| $y_j$ / [-] | 0.00 | 0.00 | 0.00 | 0.00 | 0.93 | 0.07 |
| $\phi_j$ / [-] | *N/A* | *N/A* | *N/A* | *N/A* | 1.01 | 0.99 |

.

# C

# Kinetic Reaction Modelling

For the kinetic modelling, the models developed by Rahimi and Niksiar [96] and Hamadeh, Mirgaux, and Patisson [50] were supported by parameters extracted from literature. Parameters like these are kinetic rate constants and equilibrium constants, among others. In this appendix, all necessary relationships to calculate the kinetic reaction rates for all reactions researched throughout this thesis are given. This is split into the gas phase reactions in Appendix C.1, reduction reactions in Appendix C.2 and the carburization reactions in Appendix C.3. Finally, in Appendix C.4, the diffusivities of the gases are further explicated.

## C.1. Gas Phase Reactions

The gas phase reactions that were researched in this thesis study are SRM (*R6*) and WGS (*R7*). For these two reactions, kinetic reaction rate constants were determined experimentally. For WGS, for every different type of iron oxide a different kinetic reaction rate constant applies. The rate constants for SRM and WGS are given in Equation (C.1) up to and including Equation (C.5).

$$k_6 = 392\ exp\left(\frac{6770}{RT}\right) \tag{C.1}$$

$$k_{7,\mathrm{Fe}} = 93.3\ exp\left(\frac{-7320}{RT}\right) \tag{C.2}$$

$$k_{7,\mathrm{Fe_{0.95}O}} = 1.83 \cdot 10^{-5}\ exp\left(\frac{7.84}{RT}\right) \tag{C.3}$$

$$k'_{7,\mathrm{Fe_3O_4}} = 2.683372 \cdot 10^{-5}\ exp\left(\frac{-112000}{RT}\right) \tag{C.4}$$

$$k'_{7,\mathrm{Fe_2O_3}} = 4.56 \cdot 10^{-3}\ exp\left(\frac{-88000}{RT}\right) \tag{C.5}$$

Here, $k_6$ and $k_7$ are given in [mol/(cm$^3$s)], while $k'_7$ has units of [mol/(kg$_{\mathrm{cat}}$s)]. For $k'_7$, the kg$_{\mathrm{cat}}$ refers to the mass of iron oxide available for WGS. Values for the Gibbs free energy were obtained via NIST-JANAF and equilibrium constants were calculated via Equation (C.6).

$$K_{\mathrm{eq},i} = exp\left(\frac{-\Delta {G_{\mathrm{R}.i}}^0}{RT}\right) \tag{C.6}$$

## C.2. Reduction Reactions

The reaction rates for the reduction of the iron oxide pellets are a function of an experimentally determined mass transfer coefficient as well. For hematite reduction with $H_2$ and CO, the governing mass transfer coefficient equations are given in Equation (C.7) and Equation (C.8) respectively. For wustite reduction with $H_2$ the mass transfer coefficient is given in Equation (C.9), while the mass transfer coefficient of wustite reduction with CO is shown in Equation (C.10).

$$k_1 = 160\ exp\left(\frac{-92092}{RT}\right) \tag{C.7}$$

$$k_2 = 23\ exp\left(\frac{-71162}{RT}\right) \tag{C.8}$$

$$k_3 = 25\ exp\left(\frac{-73674}{RT}\right) \tag{C.9}$$

$$k_4 = 17\ exp\left(\frac{-69488}{RT}\right) \tag{C.10}$$

The mass transfer coefficients for the reduction reaction rates are all given in [m/s]. This eventually leads to a two dimensional reaction rate for both hematite and wustite reduction. The equilibrium constant $K_{\mathrm{eq},i}$ was derived similar as in Appendix C.1, through Equation (C.6).

## C.3. Carburization Reactions

The carburization reactions of MC (*R9*) and BR (*R10*) are dominant and their respective mass transfer coefficients are presented in Equation (C.11) and Equation (C.12), respectively.

$$k_9 = 16250\ exp\left(\frac{-55000}{RT}\right) \tag{C.11}$$

$$k_{10} = 1.8\ exp\left(\frac{-27200}{RT}\right) \tag{C.12}$$

$$k'_{10} = 2.2\ exp\left(\frac{-8800}{RT}\right) \tag{C.13}$$

All mass transfer coefficients for the carburization reactions are given in [mol/(m$^3$s)]. BR is a function of two mass transfer coefficients, $k_{10}$ and $k'_{10}$. Both are incorporated in the BR reaction rate equation of Equation (3.19).

## C.4. Diffusivity of Gases

The governing equations for the total pore diffusion are presented in Section 3.2.2. To calculate the molecular diffusion of arbitrary gas $A$ through a mixture of $n$ other gases, the binary diffusion coefficients of gas $A$ through ($j = n$) gases are required. The binary diffusion coefficient $D_{\mathrm{A}j}$ in [m$^2$/s] can be calculated according to the method of Treybal [117], via Equation (C.14). This method applies to mixtures of nonpolar gases or when a polar and a nonpolar gas are present.

$$D_{\mathrm{A}j} = \frac{10^{-4}\ \left(1.084 - 0.249\sqrt{1/M_{\mathrm{A}} + 1/M_j}\right) T^{3/2}\sqrt{1/M_{\mathrm{A}} + 1/M_j}}{P_{\mathrm{a}}\ (r_{\mathrm{A}j})^2\ f(k_{\mathrm{B}}T/\epsilon_{\mathrm{A}j})} \tag{C.14}$$

In Equation (C.14), the binary diffusion coefficient $D_{\mathrm{A}j}$ in [m$^2$/s] is given via absolute temperature T in [K], the molecular weights of gas A $M_{\mathrm{A}}$ and $j$ $M_j$ in [kg/mol], absolute pressure $P_{\mathrm{a}}$ in [N/m$^2$],

the molecular separation at collision $r_{Aj}$ (= $(r_A + r_j)/2$) in [nm], the energy of molecular attraction $\epsilon_{Aj}$ (= $\sqrt{\epsilon_A \epsilon_j}$) in [$(m^2\ kg)/s^2$], Boltzmann constant $k_B$ in [J/K] and the dimensionless collision function $f(kT/\epsilon_{Aj})$. When $\epsilon_A$ is known, the collision function can be extracted from the book of Treybal [117]. The parameters required to solve Equation (C.14) are listed in Table C.1.

**Table C.1:** Gases and their respective values for the different parameters of Equation (C.14) [117].

| **Component *A*** | $\epsilon_A/k_B$ / [K] | $r_A$ / [nm] | $\epsilon_A$ / [$(m^2 \cdot kg)/s^2$] |
|---|---|---|---|
| $H_2$ | 59.7 | 0.2827 | $8.24 \cdot 10^{-22}$ |
| $H_2O$ | 809.1 | 0.2641 | $1.12 \cdot 10^{-20}$ |
| CO | 91.7 | 0.3690 | $1.27 \cdot 10^{-21}$ |
| $CO_2$ | 195.2 | 0.3941 | $2.70 \cdot 10^{-21}$ |
| $CH_4$ | 148.6 | 0.3758 | $2.05 \cdot 10^{-21}$ |
| $N_2$ | 71.4 | 0.3798 | $9.86 \cdot 10^{-22}$ |

Knudsen diffusion is applicable if the mean free path length of a molecule is smaller than the pore diameter. The maximum pore diameter of a porous iron oxide pellet in this thesis is 10 µm (= $10^{-6}$ m). The higher the pressure, the lower the mean free path length. The mean free path length of a molecule can be calculated through the following relationship:

$$\textit{Mean free path length} = \frac{RT}{\sqrt{2}\ \pi\ d_A{}^2\ N_A\ P} \tag{C.15}$$

In Equation (C.15), $R$ is the universal gas constant in [(N·m)/(mol·K)], $T$ the temperature in [K], P the pressure in [$N/m^2$], $N_A$ the Avogadro constant in [1/mol] and $d_A$ the molecular diameter of gas $j$ in [m]. Values for $d_A$ were obtained through Treybal [117] and are listed in Table C.2. In the same table, the mean free path lengths for all gaseous components of this thesis are given for P = 1 bar, the minimum amount of pressure applied in this study. If the mean free path length of the molecule is smaller than 10 µm for the lowest pressure researched, Knudsen diffusion is valid for higher pressures as well. In Table C.2 it shown that the mean free path lengths of all molecules are indeed smaller than 10 µm and that therefore Knudsen diffusion applies for the direct reduction of iron ore for all reactive gases in this thesis.

**Table C.2:** Molecular diameter and mean free path lengths at P = 8 bar for all reactive gaseous components considered throughout this thesis [117]. For all gaseous components, the mean free path length is smaller than the pore diameter (= $10^{-6}$ m) and hence Knudsen diffusion is valid.

| **Component *A*** | $d_A$ / [m] | *Mean free path length* / [m] |
|---|---|---|
| $H_2$ | $2.89 \cdot 10^{-10}$ | $4.36 \cdot 10^{-7}$ |
| $H_2O$ | $2.65 \cdot 10^{-10}$ | $5.19 \cdot 10^{-7}$ |
| CO | $3.76 \cdot 10^{-10}$ | $2.58 \cdot 10^{-7}$ |
| $CO_2$ | $3.30 \cdot 10^{-10}$ | $3.35 \cdot 10^{-7}$ |
| $CH_4$ | $3.80 \cdot 10^{-10}$ | $2.52 \cdot 10^{-7}$ |

To calculate the Knudsen diffusivity, the Knudsen diffusion constant $K_{0,A}$ for gaseous component $A$ is required. The Knudsen diffusion constant can be calculated via Equation (C.16) [111].

$$K_{0,A} = \frac{3\pi\ R_g}{32\ (1 - \epsilon_p)\ (1 + \pi/8)} \tag{C.16}$$

In Equation (C.16), the Knudsen diffusion constant $K_{0,A}$ in [m] is a function of grain radius $R_g$ in [m] and dimensionless pellet porosity $\epsilon_p$.

# D

# Techno-Economic Scenario Modelling

For every economical scenario that was researched in this thesis study, assumptions had to be made regarding the costs for all different aspects of the LCOP and CMC equations. In Appendix D.1, the general techno-economic aspects that were applied for all scenarios are explicated. In Appendix D.2 the costs for the DRI shaft furnace are discussed, while in Appendix D.3 the electrolyzer costs for scenario B and C are given. Finally, in Appendix D.4 the parameters for the construction and maintenance of the wind farm proposed in scenario C are given.

## D.1. General Techno-Economical Aspects

To calculate the LCOP of steel for a proposed techno-economical scenario as given in Equation (3.20), an estimation must be made of the $C_{\text{capex}}$, $C_{\text{opex}}$, $C_{\text{maint}}$, $C_{\text{labour}}$ and $C_{\text{emission}}$. Also, the annuity factor or $AF$ with which the $C_{\text{capex}}$ will be multiplied has to be determined through Equation (D.1).

$$AF = \frac{r\,(1+r)^{\text{n}}}{(1+r)^{\text{n}} - 1} \tag{D.1}$$

In Equation (D.1), $AF$ can be found via the dimensionless discount rate $r$ and the lifetime of the plant $n$ in [years]. For the general calculations of $C_{\text{capex}}$ and the $AF$, the parameters listed in Table D.1 were used.

**Table D.1:** Fixed costs parameters.

| Parameter | Value | Unit | Source |
|---|---|---|---|
| $r$ | 0.1 | [-] | [90] |
| $n$ | 20 | [years] | [90] |
| *Lang factor* | 2 | [-] | [15] |
| *€/$-exchange rate* | 1.09 | [-] | [16] |
| *Annual steel production* | 1 | [Mt] | *N/A* |

The Lang factor mentioned in Table D.1 is a multiplier of $C_{\text{capex}}$ used to estimate all costs extra costs for things like smaller equipment, piping, electrical wiring etc. that need to be considered when building an industrial plant. The €/$-exchange rate given in Table D.1 was taken at 26-02-2024, while the annual steel production for all scenarios was set to 1 Mt. The $C_{\text{maint}}$ can be estimated as 1.5% of $C_{\text{capex}}$ as described by Bhaskar et al. [15] and given in Equation (D.2). For simplicity, the $C_{\text{maint}}$ is assumed to be the same for all three scenarios.

$$C_{\text{maint}} = 0.015\ C_{\text{capex}} \tag{D.2}$$

Furthermore, for all three scenarios for $C_{\text{labour}}$ an approximate cost of €18.35 per tonne steel produced is assumed. For an annual production of 1 Mt of steel, this amounts to €18.35M in total. The calculations

for the $C_{capex}$, $C_{opex}$ and $C_{emission}$ for the DRI SF, the electrolyzer and the wind farm are different for all scenarios and hence their respective parameters are discussed in Appendix D.2, Appendix D.3 and Appendix D.4.

## D.2. Shaft Furnace

The $C_{emission}$ depends on the costs of $CO_2$ and the total $CO_2$ emitted into the atmosphere by a certain plant configuration. Since the DRI production process operates on 100% $H_2$, only reported $CO_2$ emissions of the EAF process were regarded. These values and parameters are presented in Table D.2, including the current and future estimated emission prices. When electricity is used for the production of gray or green $H_2$, the GEF as mentioned in Section 4.3.2 must also be taken into account for the total indirect $CO_2$ emissions.

**Table D.2:** DRI $CO_2$ emission estimations for the Netherlands. Since the process operates on 100% $H_2$, only the emissions coming forth of the EAF are considered.

| Parameter | Value | Unit | Source |
|---|---|---|---|
| *Direct EAF Emissions* | 73 | [kg $CO_2$/t steel produced] | [15] |
| *Indirect EAF Emissions* | 1427 | [kg $CO_2$/t steel produced] | [15] |
| *EU emission price - 2023* | 94 | [€/t $CO_2$] | [84] |
| *EU emission price - 2030* | 160 | [€/t $CO_2$] | [84] |
| *EU emission price - 2040* | 400 | [€/t $CO_2$] | [84] |

Subsequently, the total amount of raw materials required on a yearly and hourly basis for 100% $H_2$-based reduction was determined. The oversight of feedstock requirements and their predicted prices is presented in Table D.3.

**Table D.3:** Raw materials necessary for DRI steel production based on 100% $H_2$.

| Parameter | Value | Unit | Source |
|---|---|---|---|
| *Metallization* | 0.94 | [-] | [50] |
| *$Fe_2O_3$ input* | 1600 | [kg $Fe_2O_3$/t steel produced] | *N/A* |
| *$Fe_2O_3$ price* | 110 | [€/tonne] | [116] |
| *$H_2$ input for reduction* | 60 | [kg $H_2$/t steel produced] | [98] |
| *$H_2$ input for heating* | 6 | [kg $H_2$/t steel produced] | [98] |
| *Hourly $H_2$ demand* | 7.55 | [t $H_2$/h] | *N/A* |
| *EU $H_2$-price - 2023* | 8 | [€/kg $H_2$] | [22] |
| *EU $H_2$-price - 2030* | 5 | [€/kg $H_2$] | [38] |
| *EU $H_2$-price - 2040* | 2 | [€/kg $H_2$] | [31] |

For a DRI SF, the costs for $C_{capex}$ and $C_{opex}$ given in Table D.4 were considered.

**Table D.4:** The CAPEX and OPEX of a DRI SF, including the EAF unit.

| Parameter | Value | Unit | Source |
|---|---|---|---|
| *DRI Shaft Furnace - CAPEX* | 230 | [€/t steel per year] | [61] |
| *DRI Shaft Furnace - OPEX* | 11 | [€/t steel produced] | [24] |
| *DRI Shaft Furnace - Electricity* | 80 | [$kWh_e$/t steel produced] | [24] |
| *Electric Arc Furnace - CAPEX* | 147 | [€/t steel per year] | [121] |
| *Electric Arc Furnace - OPEX* | 30 | [€/t steel produced] | [24] |
| *Electricity Price NL (2024)* | 70 | [€/$MWh_e$] | [43] |

## D.3. Electrolyzer

Many types of electrolyzers exist that differ in efficiencies, capacities and scale-up potential. Out of the different types of electrolyzers, the Poly Exchange Membrane (PEM) shows to best scale-up potential and the highest efficiencies. Therefore, for the construction of an on-site electrolyzer in scenario B and C a PEM is installed. The necessary capacity, CAPEX and OPEX data for PEM electrolyzers used throughout this thesis is given in Table D.5 alongside information on $H_2$ storage [120]. In accordance with literature, this storage is initially assumed to be sufficient for 4.5 hours.

**Table D.5:** The CAPEX and OPEX for a PEM electrolyzer and $H_2$ storage.

| Parameter | Value | Unit | Source |
|---|---|---|---|
| *Electrolyzer - CAPEX (2020)* | 400 | [€/$kW_e$] | [120] |
| *Electrolyzer - CAPEX (2030)* | 240 | [€/$kW_e$] | [120] |
| *Electrolyzer - CAPEX (2050)* | 80 | [€/$kW_e$] | [120] |
| *Electrolyzer - Efficiency (2020)* | 53 | [$kWh_e$/kg $H_2$] | [33] |
| *Electrolyzer - Efficiency (2030)* | 45 | [$kWh_e$/kg $H_2$] | [33] |
| *Electrolyzer - Efficiency (2050)* | 40 | [$kWh_e$/kg $H_2$] | [33] |
| *Electrolyzer - Capacity (2020)* | 400 | [$MW_e$] | *N/A* |
| *Electrolyzer - Capacity (2030)* | 340 | [$MW_e$] | *N/A* |
| *Electrolyzer - Capacity (2050)* | 300 | [$MW_e$] | *N/A* |
| *$H_2$ Storage Tank - CAPEX* | 459 | [€/kg $H_2$] | [51] |
| *$H_2$ Storage Tank - Capacity* | 34000 | [kg $H_2$] | *N/A* |
| *$H_2$ Compressor - CAPEX* | 2335 | [€/kg $H_2$] | [29] |

When an hourly demand of 7.55 tonnes of $H_2$ is considered for the DRI process, an electrolyzer with a capacity of 400 MW is required for the 2020 scenario. For the electrolyzer, it is assumed that a total replacement of the stacks is necessary for every 90.000 hours of operation and that the total costs for stack replacement are approximately 0.22 times the electrolyzer costs [120]. The electrolyzer, $H_2$ storage tanks and compressors are assumed to have an average lifetime of 20 years. The emissions produced by the construction of the electrolyzer were not taken into account in this techno-economic analysis.

## D.4. Wind Farm

The location of the wind farm considered for this thesis is the IJmuiden Ver site, that is located approximately 54 km from the TATA Steel site in IJmuiden. The CAPEX and OPEX of all the wind farm requirements are given in Table D.6.

**Table D.6:** The CAPEX and OPEX for the wind turbines.

| Parameter | Value | Unit | |
|---|---|---|---|
| *Turbine Foundation - CAPEX (2020)* | 941000 | [€/$kW_e$] | [20] |
| *Turbine Foundation - CAPEX (2030)* | 486000 | [€/$kW_e$] | [101] |
| *Turbine Foundation - CAPEX (2050)* | 280000 | [€/$kW_e$] | [101] |
| *Turbine Equipment - CAPEX (2020)* | 1500 | [€/$kW_e$] | [20] |
| *Turbine Equipment - CAPEX (2030)* | 1200 | [€/$kW_e$] | [101] |
| *Turbine Equipment - CAPEX (2050)* | 1000 | [€/$kW_e$] | [101] |
| *Rated Power Turbine (2020)* | 8 | [$MW_e$] | [20] |
| *Rated Power Turbine (2030)* | 15 | [$MW_e$] | [101] |
| *Rated Power Turbine (2050)* | 20 | [$MW_e$] | [101] |
| *Wind Farm Capacity (2020)* | 440 | [$MW_e$] | *N/A* |
| *Wind Farm Capacity (2030)* | 370 | [$MW_e$] | *N/A* |
| *Wind Farm Capacity (2050)* | 330 | [$MW_e$] | *N/A* |

To transport the electricity produced by the wind farm to the site of TATA Steel in IJmuiden, a power substation, an AC/DC converter and export cables are required. Since the *IJmuiden Ver* wind farm lies more than 50 km from the coast, High-Voltage Direct Current (HVDC) is more efficient than Low-Voltage Alternating Current (LVAC) and hence a converter is necessary [101]. The estimated parameters for OPEX and CAPEX calculations on the other components of the balance of plant of the wind farm are presented in Table D.7. For the total length of the export cables, the distance to the coast times 1.2 was considered.

**Table D.7:** The CAPEX and OPEX for the power substation, AC/DC-converter and export cables.

| Parameter | Value | Unit | Source |
|---|---|---|---|
| *Power Converter - CAPEX* | 104 | [€/$kW_e$] | [21] |
| *Power Converter - Efficiency* | 0.995 | [-] | [21] |
| *Power Substation - Rated CAPEX* | 103 | [€/$kW_e$] | [39, 108] |
| *Power Substation - Unitary CAPEX* | 31.75 | [M€/unit] | [39, 108] |
| *Power Substation - Efficieny* | 0.99 | [-] | [39, 108] |
| *Export Cables - CAPEX* | 1.35 | [€/$kW_e$/km] | [101] |
| *Export Cables - Efficiency* | 0.97 | [/1000 km] | [101] |

# E

# Numerical Minimization Modelling

To perform a minimization on the Gibbs free energy of reaction for all components in the gaseous bulk flow, the following code was set-up and used in Python. Values for temperature and chemical potentials are altered in every modelling step.

```
clc;
clear;

% Reaction 1: Steam Reforming of Methane    CH4 + H2O  <->  CO + 3 H2
% Reaction 2: Water-Gas Shift               CO + H2O   <->  CO2 + H2
% Reaction 3: Dry reforming                 CH4 + CO2  <->  2 H2 + 2 CO

% x(1) = CH4, x(2) = H2O, x(3) = CO, x(4) = H2, x(5) = CO2

% Gibbs minimization formula

A = [];
b = [];
x0 = [1,1,0,0,0];
lb = zeros(1,5);
ub = [];

Aeq = [4 2 0 2 0    % H-balance
       1 0 1 0 1    % C-balance
       0 1 1 0 2];  % O-balance

beq = [6
       1
       1];

[x, fval] = fmincon(@G_min,x0,A,b,Aeq,beq,lb,ub);

Z = ['n_CH4=' , num2str(x(1)) , 'n_H2O=' , num2str(x(2)) , 'n_CO', num2str(x(3)) , 'n_H2=' ,
    num2str(x(4)) , 'n_CO2=' , num2str(x(5))]
disp(Z)

y_1 = x(1) / (x(1) + x(2) + x(3) + x(4) + x(5));
y_2 = x(2) / (x(1) + x(2) + x(3) + x(4) + x(5));
y_3 = x(3) / (x(1) + x(2) + x(3) + x(4) + x(5));
y_4 = x(4) / (x(1) + x(2) + x(3) + x(4) + x(5));
y_5 = x(5) / (x(1) + x(2) + x(3) + x(4) + x(5));

Y = ['y_CH4=' , num2str(y_1) , 'y_H2O=' , num2str(y_2) , 'y_CO=', num2str(y_3) , 'y_H2=' ,
    num2str(y_4) , ';y_CO2=' , num2str(y_5)];
disp(Y)

function G = G_min(x)
    R = 8.314;         % [J/(mol*K)]
    T = 1500;          % [K]
    P = 1;             % [bar]
    P0 = 1;            % [bar]
```

```
    phi_i = 1;        % [-]
    mu_1 = -1973700 ; % [kJ/mol]
    mu_2 = -1235700 ; % [kJ/mol]
    mu_3 = -1396900 ; % [kJ/mol]
    mu_4 = -655600  ; % [kJ/mol]
    mu_5 = -1965100 ; % [kJ/mol]
    y_1 = x(1) / (x(1) + x(2) + x(3) + x(4) + x(5));
    y_2 = x(2) / (x(1) + x(2) + x(3) + x(4) + x(5));
    y_3 = x(3) / (x(1) + x(2) + x(3) + x(4) + x(5));
    y_4 = x(4) / (x(1) + x(2) + x(3) + x(4) + x(5));
    y_5 = x(5) / (x(1) + x(2) + x(3) + x(4) + x(5));
    G = (x(1)*mu_1 + x(2)*mu_2 + x(3)*mu_3 + x(4)*mu_4 + x(5)*mu_5 + x(6)*mu_6) + R*T* (x(1)*
        log((y_1*phi_i*P)/P0) + x(2)*log((y_2*phi_i*P)/P0) + x(3)*log((y_3*phi_i*P)/P0) + x
        (4)*log((y_4*phi_i*P)/P0) + x(5)*log((y_5*phi_i*P)/P0));
end
```